An Assessment of Delayed Hydride Cracking in Zirconium Alloy Cladding Tubes Under Stress Transients[+]

Kwai S. Chan
Southwest Research Institute®
San Antonio, Texas 78238

Abstract

Zirconium alloy cladding tubes used in nuclear fuel rods are susceptible to delayed hydride cracking, which is a time-dependent crack growth process resulting from the stress-assisted diffusion of hydrogen to the crack tip, followed by the formation of radial hydrides and the subsequent fracture of the hydrides in the crack-tip region. Delayed hydride cracking in zirconium alloys could be a potential issue for disposal or reactor operation of high burnup fuel rods because transient stresses associated with pellet-cladding mechanical interaction during in-reactor power ramps may be sufficiently high to cause substantial hydride reorientation, formation of hydride rims and blisters, as well as radial hydrides that can make the cladding tubes susceptible to hydride fractures followed by radial-hydride-assisted delayed hydride cracking.

This article reviews the current understanding of the delayed hydride cracking behavior of zirconium alloy cladding tubes for fuel rods, focusing on the degradation mechanisms in high burnup fuel rods and loading scenarios, which could potentially lead to substantial changes in the hydride microstructure and cladding failure by delayed hydride cracking during the disposal of spent nuclear fuel rods in a waste repository. A brief summary of the general characteristics of delayed hydride cracking in zirconium

[+] Work supported by the U.S. Nuclear Regulatory Commission (Contract No. NRC–02–07–006) and Southwest Research Institute® (Focused Internal Research and Development Program).

alloy cladding is presented first. Relevant information on the cladding stresses under various usage conditions are then compiled and categorized into several characteristic stress transients that can be anticipated during reactor operation. Delayed hydride cracking in cladding tubes under stress transients is then examined under various temperatures, cooling rates, burnup levels, and loading conditions.

1. Introduction

Zirconium alloys are used extensively in nuclear reactor applications. Most of the nuclear fuel cladding for power-generating boiling water reactors (BWR) and pressurized water reactors (PWR) is made of two zirconium alloys [Zircaloy-2 (Zr-1.5Sn-0.12Fe-0.1Cr-0.05Ni in wt%) and Zircaloy-4 (Zr-1.5Sn-0.2Fe-0.1Cr-0.007Ni in wt%)] because of their low neutron cross section and good corrosion and fracture resistance in various environmental conditions. The Zircaloy cladding tubes are periodically removed, and their expected service life in a reactor may be a few years [1]. Another zirconium alloy, Zr-2.5% Nb (in wt%), is used extensively in pressure tubes in Canada Deuterium Uranium (CANDU) nuclear reactors. These tubes are structural components of the CANDU reactors, and the service life is expected to be on the order of 30 years [2]. Recently developed zirconium alloys for cladding, such as ZIRLO (Zr-1.1Sn-0.11Fe-1.2Nb in wt%) and M5 (Zr-0.04Fe-1.0Nb) are more resistant to corrosion and hydrogen pickup compared to Zircaloy-2 and Zircaloy-4.

Zirconium alloy cladding tubes used for nuclear fuel rods are susceptible to hydride embrittlement, which is caused by the fracture of hydride platelets aligned in the radial direction [3,4]. One particular form of hydride embrittlement in zirconium cladding is called delayed hydride cracking (DHC), which is a time-dependent crack growth process resulting from the stress-assisted diffusion of hydrogen to the crack tip, followed by the formation of radial hydrides and the subsequent fracture of the hydrides in the crack-tip region [4,5,6,7]. Depending on specific alloys, heat treatment, and burnup, zirconium cladding contains hydrides that are mostly aligned in the

circumferential direction with few or small amounts of randomized radial hydrides in some cases. Under a crack-tip stress field or a stress gradient, some of the circumferential hydrides may dissolve at temperatures above the solvus temperature and go back into solid solution; the hydrogen atoms in solid solution can diffuse to the highly stressed crack-tip region and precipitate as radial hydrides upon cooling, resulting in crack extension and DHC if the hydrides fracture. Failure of Zr-2.5% Nb pressure tubes in CANDU reactors has been reported and attributed to DHC [2,5,8,9,10,11]. Many studies [7–10, 12–14] of DHC kinetics in Zr-2.5% Nb have been conducted, including a multinational round-robin study [15] to produce a consistent set of DHC rates for Zr-2.5% Nb performed under the auspices of the International Atomic Energy Agency (IAEA).

According to the published literature [16–18], cladding tube failure of low burnup (<45 GWd/MTU) fuel rods is rare (< 10 ppm), usually involving residual or transient local tensile stresses [10]. Possible fuel failure that results in cladding perforation includes manufacturing defects, debris fretting, pellet-cladding interaction (PCI), pellet-cladding mechanical interaction (PCMI), corrosion, and DHC [16–18]. Some failures of Zircaloy-2 cladding tubes with and without a Zr-lined barrier were reported during service in BWRs [16, 19–24]. From 1989 to 1993 [16, 19–21], almost 30% of the failed Zr-lined rods exhibited long axial cracks that exceeded 15 cm in length. Some of these cracks were secondary defects, while a few were primary defects. Some of these cracks initiated from large hydride blisters at the outer wall of the Zircaloy-2 cladding tube and propagated inward to failure. Other cracks initiated at the inner wall and propagated

outward to the outer wall. In all cases, the failure mechanism was considered to be DHC or corrosion hydrogen cracking (CHC).

Cheng, et al. [21] performed in-reactor simulation tests to evaluate the root cause of secondary degradation of defective BWR fuel rods. Their results showed the unlined Zircaloy-2 cladding is susceptible to the formation of hydride blister and the associated hydride cracking during a power ramp. In contrast, Zr-lined Zircaloy-2 cladding is susceptible to the formation of a thick hydride rim or radial hydrides at the outer surface. Cheng, et al. [21] identified a hydride-rim-induced DHC or CHC mechanism for axial fracture of Zircaloy-2 cladding where the source of hydrogen to precipitate at the crack tip is the hydride rims rather than the circumferential hydrides in the cladding matrix. DHC has also been suspected as the possible cause of in-reactor fuel failure in reactivity-initiated accident-like (RIA-like) testing in the French CABRI test reactor, REP-Na1 [25,26]. In this case, a crack initiated at the inside wall and propagated to the outside wall of a PWR Zircaloy-4 cladding tube, as summarized by Chung [25]. CRWMS M&O [27] have reviewed the potential hydride-related degradation mechanisms of spent nuclear fuel cladding under long-term repository conditions. Oxide cracking and fracture of hydride blisters were both considered. They cited extensive evidence of hydride blisters that formed beneath a spalled oxide layer [28–32] as well as evidence of the presence of concentrated hydrides or hydride blisters [29, 33–34] near the pellet-pellet boundaries and gaps in Zircaloy-4 cladding in fuel rods operated to burnups higher than ≈ 55 GWd/MTU [27]. While acknowledging the potential for DHC in the outer wall of Zircaloy-4 cladding tubes due to the nucleation, growth, and cracking of hydride blisters, CRWMS M&O [27] considered this failure mechanism did not affect repository

performance significantly for the majority of commercial spent nuclear fuels. They concluded that the formation of locally concentrated hydrides was limited to a small fraction of PWR cladding fabricated from standard Zircaloy-4 operated to burnups higher than 55 GWd/MTU.

For high burnup fuel rods, Pierron, et al. [35] recently showed evidence of oxide cracking on the outer surface of an irradiated Zircaloy-4 tube operated to a fuel burnup of 67 GWd/MTU and with fast neutron fluence of 1.3×10^{22} n/cm^2. A solid hydride rim was also observed to lie beneath the oxide layer. The observation of a solid hydride rim [35] suggested that hydride-related fracture in cladding tubes may increase as the population of high burnup fuel rods increases. For high burnup fuel rods, a potential failure mechanism in irradiated Zircaloy-4 cladding is fracture of the oxide layer on the outer surface, followed by crack penetration into a hydride layer or rim formed beneath the oxide layer and subsequent DHC causing failure of the cladding tube.

The operative failure mechanisms in Zircaloy-2 cladding tubes appear to depend on the level of burnup. After examining 22 nonbarrier BWR failed rods that exhibited axial splits in service, Lin, et al. [20] concluded split fractures observed in these rods were developed from the primary defect. In addition, the axial cracks were likely caused by DHC in the Zircaloy-2 cladding. The burnup level of the split rods ranged from 27 to 28 GWd/MTU. More recently, Hayashi, et al. [36] studied the failure mechanisms in BWR segment rods with Zircaloy-2 cladding during power ramp tests. The segment rods were irradiated for 3 cycles (43 GWd/MTU), 4 cycles (53 GWd/MTU), or 5 cycles (61 GWd/MTU), followed by power ramp testing. At low burnups (< 43 GWd/MTU), Zircaloy-2 cladding failed by pinhole perforation due to PCI and stress corrosion

cracking (SCC). At higher burnups (53 and 61 GWd/MTU), Zircaloy-2 cladding tubes failed by fracture of radial hydrides formed at the outer rim under the PCMI stresses. Cracking initiated from the outer surface of the cladding tube and propagated to inside and axial directions. The experimental observations indicate that the operative failure mechanism in cladding tubes varies with burnup levels and hydrogen contents. In addition, the PCMI stresses were sufficiently high to cause the formation of radial hydrides and their fractures at the outer rim, leading to cladding failure by radial-hydride-assisted DHC (RHA-DHC). According to an IAEA conference report [18], the RHA-DHC process may potentially limit high burnup operations in BWRs because hydriding and hydride-initiated fracture is more pronounced at higher burnups due to increasing hydrogen contents and PCMI stresses. Thus, there is a need to examine the role of DHC in the cladding performance of high burnup fuels.

The onset of DHC in zirconium alloys is controlled by the growth threshold, K_{IH}, which is the stress intensity factor that a crack must exceed for DHC growth to proceed [9,12–14]. As a result, the cladding stress and the size of cracks or defects in the cladding tubes, if present, are important contributing factors, among other factors such as temperature [12,37,38], texture [39,40], hydrogen content [12,38,41,42], neutron irradiation fluence [38,43–45], and cooling rate that affect the DHC growth kinetics in zirconium alloy cladding. Alloy composition [46], microstructure [44], and heat treatment can also affect the susceptibility of an alloy toward delayed hydrides cracking because they influence the oxidation of zirconium to form zirconium oxide, hydrogen, and the absorption of hydrogen into zirconium [47]. Under normal conditions, the stresses in cladding arise from the internal gas pressure in the fuel rods. As part of the

cladding evaluation for the potential repository at Yucca Mountain [48], the U.S. Department of Energy (DOE) has calculated the fission gas pressure in fuel rods and the corresponding stresses as a function of burnup. In this report, DOE estimated an internal pressure of 4.8 MPa [0.7 ksi] as a mean value for a 44.1 GWd/MTU burnup, and 5 percent of the cladding tubes exceeded an internal pressure of 7.3 MPa [1.06 ksi] for a burnup of 63.6 GWd/MTU. These gas pressure values correspond to hoop stresses at 27 °C [81 °F] for 38.4 MPa [5.6 ksi] and 61.8 MPa [9.0 ksi] for the Westinghouse 17 × 17 Lopar (W1717WL) fuel assembly. Using a crack-size distribution based on the manufacturing defect-size distribution, Siegmann, et al. [48–50] and CRWMS M&O [27] computed the stress intensity factors acting on cracks in cladding tubes in the range of 0.5–2 MPa$(m)^{1/2}$ [0.46–1.82 ksi$(in)^{1/2}$] [27,48–50], which is less than the crack-growth threshold, K_{IH}, for DHC. Thus, DHC in cladding tubes in the potential repository was considered unlikely by DOE [27, 48-50], which is consistent with assessments made by Cunningham, et al. [51]. Cunningham, et al. [51] concluded that DHC would not be expected to occur, because the operating stress intensity factors on cracks in cladding tubes are expected to be lower than the crack-growth threshold for DHC. The previous studies, however, did not consider the possibility that the hydride microstructure of cladding tubes could be altered by creep [52] or degraded due to the formation of hydride blisters, hydride rims, and radically oriented hydrides as the result of high PCMI stresses during power ramps [36]. Recent work by Kim [52] suggested that prior creep deformation promotes hydride reorientation to form radial hydrides in spent fuel rods on cooling. The potential effect of PCMI stresses during power ramps on DHC is assessed further.

Recent advances in the development of three-dimensional (3D) finite-element codes and elastic–viscoplastic constitutive models for cladding and fuel pellets have resulted in more precise descriptions of the PCMI and more accurate computation of cladding stresses during power ramps in reactor operations [53–60]. These finite-element method (FEM) results [53–59] indicate that the time-dependent transient stresses associated with PCMI can be relatively high and can last long enough for (i) the formation of a variety of hydride morphologies including hydride blister, hydride rim, and a large field of radially oriented hydrides; and (ii) DHC to occur at least in limited amounts during reactor operations. Because the number of power ramps increases with increasing burnup, the repeated occurrence of transient stresses may affect in-reactor cladding tube integrity should DHC become activated in response to PCMI transient stresses. Although the PCMI transient stresses are present only during power ramps, some of the PCMI stresses may be retained as residual stresses due to swelling and bonding [36, 61] between the fuel pellets and cladding that prevents interface separation during cooling. In the DHC assessment, these residual stresses should be considered because they may affect hydride reorientation. The various hydride microstructures produced by the high PCMI stresses would also remain in the cladding after the fuel assemblies are removed from the reactors. Such residual stresses lower the amount of additional stress required to cause DHC growth in cladding. Thus, the potential of DHC in cladding tubes can be re-evaluated in light of insights provided by the new 3D FEM analysis of cladding stresses and PCMI.

This article reviews the current understanding of the DHC behavior of zirconium alloy cladding tubes, focusing on the degradation mechanisms and loading scenarios that

could potentially lead to cladding failure by DHC during the in-reactor power ramp and the disposal of spent nuclear fuel rods in a waste repository. The article first summarizes the general characteristics of DHC in zirconium alloy cladding. Relevant information on the cladding stresses under various usage conditions are then compiled and categorized into several characteristic stress transients that might occur during reactor operation and disposal in a waste repository. DHC potential in cladding tubes under stress transients is then examined under various temperatures, cooling rates, burnup levels, and loading conditions.

2. General characteristics of DHC in zirconium-based alloys

The integrity of zirconium alloy cladding in nuclear fuel rods during service can be degraded by DHC, a time-dependent crack growth process [2,5,8–11]. Although it has been observed in Zircaloy-2 [37,38,44–46], Zircaloy-4 [42,46], and Zr-2.5% Nb [2,5,8–15,44], most of the work on DHC has been conducted on Zr-2.5% Nb. The physical processes involved in the DHC failure mechanism are fairly well understood. In DHC, hydrogen in the cladding diffuses to a region of high tensile stress, such as that ahead of a crack-tip or notch-tip region, where it precipitates as zirconium hydrides in a direction normal to the tensile stresses [4,5,13]. Under suitable conditions, the hydrides may fracture and result in an incremental extension of the crack tip [13,14]. After crack extension, the extended crack tip becomes dormant for a period of time until sufficient amounts of hydrogen have diffused to the crack-tip region and precipitated as hydrides. Then the

cracking process repeats itself and results in the intermittent crack growth phenomenon known as DHC [8].

The crack growth kinetics of DHC is generally represented in terms of a plot of crack velocity versus stress intensity factor or V-K curve [13] as shown schematically in Figure 1, where V is crack growth velocity and K is the stress intensity factor that characterizes the near-tip stress field of a sharp crack in an elastic material subjected to an applied load, σ. For a mode I crack, the stress intensity factor is given by [62]

$$K = F \sigma \sqrt{\pi a} \tag{1}$$

where a is crack length or depth, and F is an appropriate boundary correction factor for the particular crack geometry. The V-K curve for DHC in zirconium or its alloys typically exhibits three characteristic stages or regions. Stage I is the near-threshold region where DHC growth does not occur at K levels below a threshold, K_{IH}, but increases rapidly with increasing stress intensity factors when the threshold is exceeded [12,13]. At Stage II, the DHC propagates at an essentially constant rate that is relatively independent of the stress intensity factor but is sensitive to the temperature [12]. Stage III is the unstable crack growth region where the applied stress intensity factor approaches the fracture toughness, K_{IC}, of the alloy, which is a material property that can be determined using standardized tests. Unstable fracture of the cladding tube occurs when the stress intensity factor, which represents the crack driving force, exceeds the fracture toughness ($K \geq K_{IC}$) of the alloy.

The shape of the V-K curve reflects the underlying physical mechanisms associated with the DHC in zirconium alloy cladding. Current understandings of the physical mechanisms that are responsible for the various stages of DHC growth in

zirconium alloys are reviewed to identify the role, if any, of DHC in the integrity of zirconium alloy cladding. In particular, assessing the current understandings on the origin of K_{IH} and the factors affecting the DHC threshold, the crack growth kinetics, and the onset of unstable fractures will be emphasized.

2.1. Threshold stress intensity factor, K_{IH}

DHC requires the diffusion of hydrogen to a highly stressed region, the precipitation of hydrides, and then the fracture of hydrides within the fracture process zone [5,13]. The fracture toughness of zirconium hydrides (K^h_{IC}) with the face-centered cubic (fcc) structure ranges from 1–3 MPa$(m)^{1/2}$ [0.91–2.73 ksi$(in)^{1/2}$] from 25–300 °C [77–572 ºF] [63], as shown in Figure 2. In comparison, Figure 2 also shows that the K_{IH} value for Zr-2.5% Nb ranges from 4.3–10 MPa$(m)^{1/2}$ [3.91–9.12 ksi$(in)^{1/2}$] with a 95% confidence limit for a single observation and a mean of 8.2 MPa$(m)^{1/2}$ [7.46 ksi$(in)^{1/2}$] for all tests in the database compiled by Shi and Puls [13]. The K_{IH} value for Zircaloy-2 tubes [38,40,44] ranges from 5.2–14.2 MPA$(m)^{1/2}$ [4.73–8.29 ksi$(in)^{1/2}$]. Recently, Huang and Ho [42] reported that the K_{IH} values for the Zircaloy-4 plates with 100–168 wppm. hydrogen are about 20–21 MPa$(m)^{1/2}$ at 200 ºC [392 ºF] and 300 ºC [572 ºF]. These K_{IH} values are considerably higher than the K_{IH} value of 5 MPa$(m)^{1/2}$ reported by Grigoriev and Jakobsson [46] for Zircaloy-4 tubes. The reasons for the high K_{IH} values observed in the Zircaloy-4 studies by Huang and Ho [42] are not known; possible reasons include low hydrogen contents, texture effect, and incomplete hydride coverage and ligament toughening by Zr-grain ligaments at the crack wake. All the K_{IH} measurements

for Zr-2.5% [9,12], Zircaloy-2 [37,38,40,44–46]], and Zircaloy-4 [42,46] have been obtained using fracture mechanics specimens with a large crack. For large crack fracture mechanics specimens, the K_{IH} for zirconium alloys is always larger than the fracture toughness of the hydrides, indicating that the limiting process associated with the DHC threshold is more involved than just the fracture of hydrides near the crack-tip or notch-tip region. To the knowledge of the author, K_{IH} threshold values have not been reported for small cracks in zirconium alloys.

Shi and Puls [13] elucidated the theoretical value of K_{IH} for zirconium alloys by considering fracture initiation of hydrides formed ahead of a sharp crack tip and a shallow notch tip [14] based on a local critical stress for hydride fracture. The local stress at the crack or notch tip was modeled by summing the contributions from the elastic stress field of a sharp crack or a notch and the compressive stress field induced by the volume change incurred during the precipitation of hydrides in a zirconium matrix with hydrogen in solid solution. The volume increases associated with the formation of the metastable face-centered tetragonal (fct) hydride and the stable fcc hydride are 12% and 17%, respectively [4]. Figure 3(a) illustrates the effects of hydride formation on the near-tip stress field of a sharp crack after hydride formation in the crack-tip process zone. The von Mises effective stress, σ_{eff}, computed from the crack-tip elastic stress field, increases with decreasing distance from the crack tip, reaching a value equal to the yield stress, σ_y, of the matrix in the crack-tip plastic zone. Within the crack-tip plastic zone, the compressive hydride transformation stress, $\sigma_{hydride}$, is superimposed and summed with σ_{eff} to give the local stress, σ_{local}, normal to the crack-tip hydride. The calculated local stress distributions for a crack tip with a hydride are shown for various K levels in

Figure 3(b). The calculation by Shi and Puls [13] showed that the local stress near the crack tip was compressive at low K levels {K <2 MPa(m)$^{1/2}$ [1.82 ksi(in)$^{1/2}$]}, but became tensile when K >4 MPa(m)$^{1/2}$ [3.64 ksi(in)$^{1/2}$]. Shi and Puls [13] postulated that hydride fracture occurs only when the local stress in the hydride exceeds a critical value. The critical stress criterion for hydride fracture led to an expression for K_{IH}, which is given by Shi and Puls [13]

$$K_{IH} = \left(\frac{E^2 \varepsilon_\perp t}{8\pi (1-\nu^2)^2 \lambda} \right)^{1/2} \tag{2}$$

with

$$\lambda = \frac{1}{1-2\nu} - \frac{\sigma_f^h}{\sigma_y} \tag{3}$$

where E is the elastic modulus, ν is Poisson's ratio, σ_y is the yield stress of the Zr alloy, t is hydride thickness, σ_f^h is the fracture strength of the hydride, and $\varepsilon_\perp$ is the transformation strain component normal to the crack in a Mode I crack configuration. Using Eq. (2) and the pertinent material properties for Zr-2.5% Nb and the hydrides, Shi and Puls [13] computed the K_{IH} values for Zr-2.5% Nb as a function of temperature. Their predictions of the K_{IH} values for both irradiated and unirradiated Zr-2.5% Nb are compared against experimental data in Figure 4. The predicted K_{IH} values are lower than those observed experimentally. Shi and Puls [13] attributed the discrepancies between model prediction and experimental data partly to uncertainties of the values of material parameters used in the computation and partly to less than 100% coverage of hydrides in the near-tip process zone so that the fracture toughness of the zirconium matrix also contributed to the observed K_{IH} value. In particular, the hydride fracture strength was not

available and was taken to be 7.357×10^{-3}E, which corresponds to fracture strengths of 694 MPa [100.7 ksi] at 25 °C [77 °F] and 579 MPa [84.0 ksi] at 300 °C [572 °F]. Subsequent work by Shi and Puls [64] determined that the fracture strength of hydrides in Zr-2.5% Nb was about 648 MPa [94.0 ksi] at 25 °C [77 °F] and 623 MPa [90.4 ksi] at 300 °C [572 °F]. Thus, the author concludes that part of the discrepancies could have arisen from uncertainties in the material properties used (fracture strength), as indicated by Shi and Puls [13]. However, the fracture toughness of the zirconium matrix is considerably higher than that of the hydrides. In the author's opinion, incomplete hydride coverage, which results in toughening by matrix ligaments and is discussed later (Section 2.1.2.), is the more important explanation for the discrepancy between theory and experiment.

The effects of a compressive transformation stress field on the K_{IH} threshold can be modeled based on transformation toughening developed to explain the toughening resulting from the transformation of zirconia (ZrO_2) from the tetragonal structure to the monoclinic structure near the crack-tip region [65]. In both zirconia and zirconium hydrides, the stress-induced phase transformation results in a volume increase and a compressive stress field in the matrix that shields the crack tip from the applied tensile stress. This is illustrated in Figure 5, which shows a Mode I crack subjected to a remotely applied stress (resulting in K) and a hydride formed at the crack tip. The local stress intensity at the crack tip, K_{tip}, is given by [65]

$$K_{tip} = K - K_S \tag{4}$$

where K_s is the reduction in the stress intensity factor of the main crack resulting from shielding induced by phase transformation near the crack tip. According to the analysis by [65],

$$K_S = \frac{0.22}{(1-\nu)} \varepsilon^T E V_f \sqrt{w} \tag{5}$$

where ε^T is the transformation strain, E is the elastic modulus, ν is the Poisson's ratio, V_f is the volume fraction of the transformed phase (e.g., hydrides), and w is the width of the transformation zone. At the onset of hydride fracture, K_{tip} equals the fracture toughness of the hydride K_{IC}^h, and $K = K_{IH,}$ leading to

$$K_{tip} = K - K_S = K_{IC}^h \tag{6}$$

and

$$K_{IH} = K_{IC}^h + \frac{0.22}{(1-\nu)} \varepsilon^T E V_f \sqrt{w} \tag{7}$$

after Eq. (5) is substituted into Eq. (6).

Pan, et al. [66] utilized Eqs. (5) and (7) and the pertinent material parameters for fcc zirconium hydrides, which are summarized in Table 1, to predict the K_S and K_{IH} values for Zr-2.5% Nb and Zircaloy-2 as a function of temperature. As shown in Figure 6, the fracture toughness value of zirconium hydrides, taken from Simpson and Cann [64], ranges from 1 to 3 MPa(m)$^{1/2}$ [0.91–2.73 ksi(in)$^{1/2}$] in the temperature range of 300–600K [80.6–620.6 ºF]. In contrast, the computed value of the shielding stress intensity factor, K_S, is –4.34 MPa(m)$^{1/2}$ [–3.95 ksi(in)$^{1/2}$] at 300K [80.6 ºF] and increases linearly

with increasing temperature to −2.84 MPa(m)$^{1/2}$ [−2.58 ksi(in)$^{1/2}$] at 600K [620.6 ºF]. The calculated K_{IH} value, which is the sum of K_S and K_{IC}^{h}, has a value of 5.36 MPa(m)$^{1/2}$ [4.88 ksi(in)$^{1/2}$] at 300K [80.6 ºF] and increases linearly with temperature to 6.04 MPa(m)$^{1/2}$ [5.50 ksi(in)$^{1/2}$] at 600K [620.6 ºF]. The calculated K_{IH} values are in agreement with the lower bounds of the experimental data for Zr-2.5% Nb [13] and Zircaloy-2 [38,44,50]. A substantial number of the experimental K_{IH} measurements, however, exceed the lower bound and the model calculations based on the crack-tip shielding and phase transformation toughening theories. The results indicate that crack-tip shielding by hydride formation at the crack tip is significant and is partly responsible for the experimental observation that the K_{IH} is higher than K_{IC}^{h}.

Table 1. Material Parameters in the K_{IH} Model for Zr-2.5% Nb and Zircaloy-2
[1 MPa = 0.145 ksi; 1 MPa(m)$^{1/2}$ = 0.91 ksi(in)$^{1/2}$]

Parameter	Expression or Value
Young's modulus [67]	E (MPa) = 95900-57.4(T-273), T in K
Poisson's ratio [67]	$\nu = 0.436 - 4.4.8 \times 10^{-4}$(T-300), T in K
Fracture toughness of hydrides [63]	K_{IC} (MPa(m)$^{1/2}$) = −1.167 + 7.2727 x 10^{-3} T, T >300K [80.6 °F]
Transformation strain [4]	$\varepsilon^T = 0.054$
Transformation zone width [13]	w = 5 μm [0.197 mil]

Because the K_{IH} threshold originates from crack-tip shielding, the value of K_{IH} for DHC in zirconium-based alloys is expected to vary with the crack length and exhibits different K_{IH} values for small and large cracks. In general, the K_{IH} for small cracks is expected to have a lower value than that of large cracks because of a longer crack wake with greater crack-tip shielding. The growth threshold for small cracks, K_{IH}^{SC}, and large cracks, K_{IH}^{LC}, are related according to the expression given by [68]

$$K_{IH}^{SC} = K_{IH}^{LC} \sqrt{\frac{a}{a + a_O}} \tag{8}$$

where a_o is the small-crack parameter. The a_o parameter is defined based on the dependence of the hydride fracture stress on crack length. For fracture of hydrides by large cracks, linear-elastic fracture mechanics is applicable, and the fracture stress increases with decreasing crack length according to a $-1/2$ power, as shown by the dashed lines to $K_{IH} = 5.38$ MPa$\sqrt{m}$ [4.89 ksi(in)$^{1/2}$] and 12 MPa$\sqrt{m}$ [10.9 ksi(in)$^{1/2}$] in Figure 7. This range of K_{IH} values encompasses the lower and upper bound of the growth thresholds observed in Zr-2.5% Nb. For hydrides with small or no cracks, fracture occurs at a constant stress value σ_f^h {≈ 648 MPa [91.0 ksi]} that is relatively independent of the crack length. The transition from a stress-controlled process to a K-controlled process can be considered to occur at $a = a_o$, as shown in Figure 7. The value of a can be computed on the basis that the fracture stress corresponds to the hydride fracture strength at $a = a_o$, leading to

$$a_o = \frac{1}{\pi}\left[\frac{K_{IH}^{LC}}{F\sigma_f^h}\right]^2 \tag{9}$$

where F is the crack geometry correction factor with $F = 1.12$ for an edge crack with a shallow crack depth (e.g., a/W < 0.05). For fcc hydrides, a_o has a value of about 17 μm and 85 μm [0.67 mil and 3.35 mil] for K_{IH} = 5.28 and 12 MPa$\sqrt{m}$ [4.8 and 10.9 ksi(in)$^{1/2}$], respectively, when the pertinent fracture toughness and fracture strength values are substituted into Eq. (9). Figure 7 shows the corresponding threshold stresses as a function of crack length (denoted as solid lines), so for a given crack length, small cracks can propagate at a stress lower than those of large cracks.

Using the appropriate a_o for various K_{IH} values at 300 and 600K [80.6 and 620.6 ºF], Eq. (8) was used to calculate the K_{IH} values for small cracks as a function of crack length, and the results are presented in Figure 8. The results show that the K_{IH} value for small cracks in zirconium alloys approaches a very small value at diminishing crack size. On the other hand, hydride fracture occurs only when the hydride length exceeds a critical length. Experimental data indicated that for Zr-2.5% Nb, the critical hydride length is on the order of 10–20 μm [0.394–0.787 mil], and the hydride width is about 2 μm [7.87×10^{-2} mil] thick [69,70]. These hydrides are formed ahead of a crack tip loaded at a stress intensity factor just below the K_{IH} threshold [70]. The crack front is not uniformly hydrided but occurs in a discontinuous, intermittent process or a narrow band of planes parallel to the crack growth plane [69]. The smallest crack length for a in Eq. (8) is therefore about 10–20 μm [0.39–0.79 mil], leading to a lower bound K_{IH} value of 3.26 and 4 MPa(m)$^{1/2}$ [2.97 and 3.64 ksi(in)$^{1/2}$] for critical crack lengths of 10 and

20 μm [0.39–0.79 mil], respectively. The K_{IH} value increases with increasing crack length and asymptotically approaches the large crack K_{IH} value, which is 5.36 MPa$(m)^{1/2}$ [4.88 ksi$(in)^{1/2}$] at 300K [80.6 ºF], but is 6.03 MPa$(m)^{1/2}$ [5.48 ksi$(in)^{1/2}$] at 600K [620.6 ºF].

It appears that the critical hydride length significantly affects the DHC threshold for small cracks. The existence of a critical hydride length, which was assessed by Shi and Puls [41], has been attributed to a transition of the local stress in the hydride from compressive to tensile as the hydride lengthens. This relationship is illustrated in Figure 9, which shows the local stress at the tip of a crack with a hydride of length L subjected to a stress intensity factor of 10 MPa$(m)^{1/2}$ [9.1 ksi$(in)^{1/2}$]. The local stress is compressive when the hydride length is 2 μm [7.87×10^{-2} mil]. The local stress becomes slightly tensile when the hydride lengthens to 3.3 μm [0.13 mil], and the local stress increases to above 1,000 MPa [145 ksi] and exceeds the fracture strength {648 MPa [94 ksi]} of the hydride when L increases to 10 μm [0.394 mil]. Furthermore, the local stress increases with increasing K values for a given hydride length. The results from Shi and Puls [41] in Figure 3(b) show that at L = 10 μm [0.394 mil], the local stress is compressive for K = 2 MPa$(m)^{1/2}$ [1.82 ksi$(in)^{1/2}$], and a local tensile stress occurs at the crack tip only when K > 4 MPa$(m)^{1/2}$ [3.64 ksi$(in)^{1/2}$]. Experimental evidence on Zr-2.5% Nb [69–71] and Zircaloy-2 [37,38,44,45] supporting the concept of a critical hydride length includes (i) direct observations of the presence of intact hydrides at the crack-tip stress intensity factor at or just below K_{IH} in Zr-2.5% Nb and (ii) the observations of discrete striation spacings and hydride spacings associated with DHC in zirconium alloys [46,47]. For Zr-2.5% Nb, the critical hydride length is about 10–20 μm

[0.394–0.787 mil] [70], which was measured directly ahead of a crack tip loaded just below K_{IH}. In many instances, a series of hydride platelets with a length on the order of 60–100 μm [2.36–3.94 mil] precipitated ahead of the crack tip during DHC in Zr-2.5%Nb [69] and Zircaloy-2 [22,37,38,44,45]. In both cases, the length of individual hydrides was about 10–15 μm [0.394–0.59 mil] [22,38]. These experimental observations suggested that a critical hydride length of 10–20 μm [0.394–0.79 mil] may apply to both Zr-2.5% Nb and Zircaloy-2. In addition, the critical hydride length (10–20 μm [0.394–0.787 mil]) is essentially identical to the a_o value. This implies that once a hydride crack forms, its crack length is almost within the continuum crack growth regime ($a > a_o$); consequently, the small crack regime is fairly limited for DHC in zirconium alloys. Thus, the large crack threshold K_{IH} values should be adequate for DHC in Zr-2.5% Nb and Zircaloy-2. Figure 8 shows the minimum K_{IH} value for small cracks in Zr-2.5% is calculated to be about 3.26–4 MPa$(m)^{1/2}$ [2.97–3.64 ksi$(in)^{1/2}$] at ≈ 10–20 μm [0.394–0.787 mil]. The K_{IH} increases rapidly with crack extension and approaches that of the large crack K_{IH} threshold after about 100–200 μm [3.94–7.87 mil] crack growth for the lower bound values of $K_{IH} = 5.36$ MPa$\sqrt{m}$ [4.88 ksi$(in)^{1/2}$] at 300K [80.6 ºF] and $K_{IH} = 6$ MPa$\sqrt{m}$ [5.46 ksi$(in)^{1/2}$] at 625K [665.6 ºF]. For the upper bound K_{IH} {= 12 MPa$\sqrt{m}$ [10.9 ksi$(in)^{1/2}$]}, the large crack threshold is not reached until after 1,000-μm [39.4-mil] crack extension. The difference in the K_{IH} values for small crack and large cracks gives rise to the resistance-curve (R-curve) behavior that has been reported by Yan and Eadie [70] and modeled by Jernkvist [72].

The difference between the experimentally measured large crack K_{IH} threshold and the estimations of the K_{IH} model shown in Figure 6 is largely caused by the presence

of additional toughening mechanisms that shield the crack-tip stresses from the fracturing of the near-tip hydrides. The toughening mechanisms responsible for increasing the K_{IH} threshold in Zr-based cladding are summarized in the following subsections.

2.1.1. Texture toughening

Zirconium hydrides are favored to form on the {1017} crystalline planes, often referred to as hydride habit planes, which are orientated about 15° from the (0001) planes [40]. This tendency results in a dependence of the K_{IH} threshold value on the crystallographic texture in the zirconium alloy cladding in general and on the basal pole component in particular. Figure 10 shows the K_{IH} threshold data [38–40, 73–75] compiled by Kim, et al. [40] as a function of volume fraction of the basal pole components. The lowest K_{IH} threshold occurs in specimens with a strong basal texture and the maximum applied stress normal to the basal plane. Under these circumstances, many grains in the near-tip regions are oriented for the formation of fcc zirconium hydrides on the {1017} planes that are aligned normal to the maximum principal stress and can be fractured easily, thereby leading to a low K_{IH} threshold. In contrast, nonbasal grains in the near-tip region form hydrides that are not oriented to the maximum principal stress and require a higher applied stress or stress intensity factor to cause hydride fracture at the crack tip, thereby enhancing the K_{IH} value. Thus, crystallographic orientation or texture of zirconium grains significantly influences the K_{IH} value for the onset of DHC.

2.1.2. Ligament toughening by zirconium grains

Because not all grains ahead of the crack tip are optimally oriented for hydride formation and fracture on the {1017} planes, some grains in the near-tip process zone might not form hydrides or may form hydrides on poorly oriented {1017} planes that result in a tortuous crack path. In both instances, the crack path can be bridged by zirconium grain ligaments that are more ductile and tougher than the fcc hydrides. This is a very powerful toughening mechanism, because the fracture toughness of the zirconium matrix can be as high as 58–70 MPa(m)$^{1/2}$ [52.8–63.7 ksi(in)$^{1/2}$] [76–80], compared to a K_{IC} close to 1 MPa(m)$^{1/2}$ [0.91 ksi(in)$^{1/2}$] for the hydrides [63]. The amount of toughening also increases with the bridging length [81–83]. Furthermore, the toughening mechanism is operative in conjunction with transformation toughening. The increase in the K_{IH} threshold due to crack bridging by zirconium-matrix ligaments can be estimated on the basis of the micromechanical model developed for treating ductile-phase toughened materials, which is given by Chan and Davidson [84]

$$K_{IH}^{br} = K_{IH}\left[1+\sqrt{1-V_f}\left(\left(\frac{K_{IC}^{Zr}}{K_{IH}}\right)^2 \exp\left(\frac{-8q}{3}\left[\frac{V_{crit}}{1-V_{Crit}}\right]\right)-1\right)\right]^{1/2} \qquad (10)$$

where V_f is the volume fraction of hydrides and V_{crit} is the critical volume fraction of hydrides for the formation of a continuous hydride network. The $1\text{-}V_f$ term represents the volume fraction of bridging zirconium-grain ligaments in the crack wake, and K_{IC}^{Zr} is the fracture toughness of the zirconium-matrix ligaments. The parameter q has a value that

ranges from 1 to 4 depending on the plastic constraint developed in the crack-tip zone [84]. Because K_{IC}^{Zr} is considerably larger than K_{IH}, the large crack K_{IH} threshold can be increased by a small number of bridging zirconium grain ligaments in the crack wake. Mills and Huang [37] have reported the direct evidence of zirconium-grain ligaments in the crack path during DHC in Zircaloy-2. Yuan and Tangri [69] showed evidence of discontinuous hydrides separated by zirconium grains ahead of a crack in Zr-2.5% Nb during DHC. Similar observations were reported by Lysell and Grigoriev [22] for axial cracks in Zircaloy-2 cladding tubes with or without an internal sponge zirconium liner. Furthermore, Huang and Huang [85] reported discontinuous hydride cracks separated by a Zr grain ligament during DHC in Zircaloy-4. Indirect experimental evidence of the zirconium-grain ligament toughening process is the observation of a fracture surface morphology consisting of facets separated by small ductile tears. Two types of facets have been identified in Zircaloy-2 [37]: (i) well-defined crystallographic facets created by the cleavage of reoriented hydrides and (ii) nondescriptive facets that result from decohesion of the hydride-zirconium matrix interface. These facets were separated by small regions of ductile tearing involving a combination of microvoid coalescence and a sliding-off mechanism. The presence of ductile tearing and shear ridges on the fracture surfaces of zirconium alloys failed by DHC is a good indication of the presence of ligament toughening by zirconium grains. Because of ligament toughening, the K_{IH} threshold observed in Zircaloy-2 can range from 12 to 18 $MPa(m)^{1/2}$ [10.9 to 16.4 $ksi(in)^{1/2}$] [37].

2.1.3. Hydrogen content

The value of K_{IH} for DHC at a given temperature is dependent on the hydrogen content. Figure 11 shows that the K_{IH} value decreases with increasing hydrogen contents for Zr-2.5% Nb at 250 °C [482 °F] [41], and the theoretical curves indicate that in Shi and Puls' analysis [41], crack-tip hydride length must exceed a critical length for hydride cracking to occur, and the maximum length a hydride can attain depends on the hydrogen content in solution. As a result, the K_{IH} increases with decreasing hydrogen content in solution.

The dependence of the critical hydrogen content for the onset of hydride cracking in Zr-2.5% Nb is shown as a function of temperature in Figure 12 [7]. The critical hydrogen content for crack initiation is larger than the hydrogen solubility limit for hydride dissolution (TSSD), but is less that that for hydride precipitation (TSSP) at a given temperature. For a given hydrogen content, DHC cannot occur at a temperature higher than TSSD because no hydrides can form, even at the crack tip. DHC occurs at a small undercooling below the TSSD, and there is a large hysteresis between the TSSP and TSSD for hydrogen in zirconium. The hysteresis, which is caused by the volume expansion during TSSP, results in different DHC behaviors during heating and cooling of zirconium alloys, as well as variations with hydrogen contents [7]. The terminal solid solubility of hydrogen in Zircaloy-2 was measured by McMinn, et al. [86]. Schofield, et al. [87] recently showed that the critical temperatures for the onset and the arrest of DHC

in Zircaloy-2 fall below the dissolution solvus temperature and above the precipitation solvus temperature, in accordance with experimental findings for Zr-2.5%Nb [7].

2.1.4. Irradiation effects

Irradiation appears to exert only a small effect on the K_{IH} value of Zr-2.5%Nb tested at 130–350 °C [266–662 °F]. Sagat, et al. [43] reported a small decrease in K_{IH} as the fluence increased to about 1×10^{25} n/m^2 [1.08×10^{26} n/ft^2] for fast neutrons with energy above 1 MeV at an irradiation temperature in the range of 250–290 °C [482–554 °F], but no increase upon further increase in fluence up to 8×10^{25} n/m^2 [8.61×10^{26} n/ft^2], as shown in Figure 13. The temperature corresponding to the data shown in Figure 13 was not reported by Sagat, et al. [43], but K_{IH} testing was conducted at 130–350 °C [266–662 °F]. The average K_{IH} was 7.5 ± 1.3 MPa(m)$^{1/2}$ [6.82 ± 1.18 ksi(in)$^{1/2}$] for the unirradiated materials compared to 6.2 ± 0.9 MPa(m)$^{1/2}$ [5.64 ± 0.82 ksi(in)$^{1/2}$] for the irradiated materials at the 95% confidence level. Similarly, the K_{IH} value for unirradiated Zircaloy-2 ranges from 7.5 to 13.8 MPa(m)$^{1/2}$ [6.87 ± 1.18 ksi(in)$^{1/2}$] for 200–300 °C [392–572 °F], while it ranges from 9.9 to 12.7 MPa(m)$^{1/2}$ [9 to 11.6 ksi(in)$^{1/2}$] in the irradiated materials at 200–300 °C [392–572 °F] [37,44]. These results suggest that the K_{IH} value at high fluence (8×10^{25} n/m^2) [8.61×10^{26} n/ft^2] might be used as a lower bound K_{IH} for irradiated Zircaloy-2 or Zircaloy-4.

2.2. Temperature dependence of DHC

Although it has a minimal effect of a factor of two on the K_{IH} threshold, temperature exerts significant influence on the growth kinetics of DHC in zirconium-based alloys. Figure 14 summarizes the complex relationships between crack velocity and reciprocal temperature observed in Zr-2.5% Nb [7] for Zircaloy-2 cladding tubes [38, 46]. At temperatures below 318 °C [604 °F] or the TSSP, DHC velocity, V, is dictated by the diffusion of hydrogen to the crack tip to form hydrides and is related to the absolute temperature according to the Arrhenius relation given by [12,38]

$$V = V_0 \exp\left(\frac{-Q_{DHC}}{RT}\right) \tag{11}$$

where Q_{DHC} is the activation energy for DHC, V_o is an empirical constant, T is absolute temperature, and R is the universal gas constant. In general, DHC velocity decreases rapidly with decreasing temperatures because the diffusion of hydrogen to the crack tip is slow at low temperatures. At temperatures above 318 °C [604 °F], the DHC velocity decreases abruptly with increasing temperature for both irradiated and unirradiated materials because of increasing hydrogen solubility that leads to more hydrogen in solid solution and less hydride being formed at the crack tip. Because there is a critical hydride length for DHC to occur, DHC velocity eventually goes to zero when the crack tip hydrides are below the critical length or the temperature exceeds the TSSD, so that no hydrides can form at the crack tip. For hydride formation-limited growth, the DHC velocity is given by

$$V = V_o^h \exp\left(\frac{Q_h}{RT}\right) \quad (12)$$

where Q_h is the activation energy for TSSP, and V_o^h is a preexponent coefficient. As shown in Figure 14, the temperature range and the experimental database over which DHC velocity decreases with increasing temperature are fairly small for irradiated materials to allow an accurate determination of Q_h. On the other hand, the experimental velocity data span a sufficiently large temperature range to determine Q_h and V_o^h based on the irradiated materials, which are then utilized for both irradiated and unirradiated materials. The value of Q_h was determined from the slope in a plot of ln V versus reciprocal temperature. Values of V_o, V_o^h, Q_{DHC}, and Q_h for Zr-2.5% Nb are presented in Table 2.

Table 2. Material Parameters Used in the DHC Computation of Time to Failure as a Function of Temperature

Parameter	Value
V_o	0.14 m/s [0.459 ft/s]
Q_{DHC}	65.5 kJ/mol [15.65 kcal/mol]
V_o^h	8.83×10^{-42} m/s [2.897×10^{-41} ft/s]
Q_h	389 kJ/mol [92.93 kcal/mol]
K_{IH}	5 MPa$(m)^{1/2}$ [4.55 ksi$(in)^{1/2}$]
K	5.25 MPa$(m)^{1/2}$ [4.78 ksi$(in)^{1/2}$]

It is evident that there are two competing mechanisms that control the dependence of DHC velocity on temperature: TSSD and TSSP [7]. Figure 12 shows the TSSD and the TSSP for Zr-2.5% Nb. The increase in DHC velocity with decreasing temperature below TSSD is controlled by hydrogen solubility limit and hydride formation beyond the critical size. In this regime, the temperature is sufficiently high, and hydrogen diffusion to the crack tip occurs quickly; a lower temperature provides a higher driving force for TSSP where fracture at the crack tip results in a higher DHC velocity. At temperatures below about 318 °C [604 °F], the DHC velocity decreases with decreasing temperature because of a lower hydrogen diffusivity and a longer time for hydrogen to move from the bulk to the crack tip. The DHC velocity exhibits a maximum value at about a critical temperature T_C, which is 318 °C [604 °F] for Zr-2.5% Nb, where the precipitation and diffusion kinetics are optimum. The critical temperature at which the maximum DHC velocity occurs is about 30–40 °C [54–72 °F] below the TSSD [7]. Limited experimental data indicated that the critical temperature, T_C, ranges from 310 to 320 ºC [590 to 608 °F] and is not sensitive to hydrogen content in the range of 60–170 wt. ppm [7].

For DHC at a constant temperature, the time to failure, t_f, can be obtained as

$$t_f = \sum \frac{da}{V} \tag{13}$$

where *da* is the crack increment. The crack velocity *V* is given by Eq. (11) for $T < T_C$, but is given by Eq. (12) for $T_C < T <$TSSD and V = 0 for T > TSSD. The time to leakage, t_l, has been computed on the basis of the crack depth reaching the cladding wall thickness, while the time to fracture, t_f, has been computed based on the stress intensity

factor exceeding a critical stress intensity factor of 70 MPa(m)$^{1/2}$ [63.7 ksi(in)$^{1/2}$]. At leakage, a crack penetrates the entire cladding thickness and internal gases inside the cladding tube can escape outward through the crack surfaces. The corresponding stress intensity factor, however, is less than the fracture toughness ($K < K_{IC}$) of the cladding so that cladding fracture does not occur at leakage. After leakage has occurred, subsequent crack growth proceeds axially and causes the stress intensity factor to increase. When $K > K_{IC}$, cladding fracture occurs by splitting the cladding tube along the axial direction. A comparison of the computed time to leakage and time to fracture for cladding tubes at 25 °C [77 °F] is presented in Figure 15. These calculations have been performed for Zircaloy-2 and Zircaloy-4, assuming the material constants for Zr-2.5% are applicable to the Zircaloy-2 and Zircaloy-4. In these calculations, the stress due to a cladding pressure of 5 MPa [0.73 ksi] was superimposed with a hoop stress of 275 MPa [39.9 ksi] assumed to result from reactor transient loading. The initial crack depth resulting from oxide and hydride blister cracking on the outer surface of a cladding tube was 0.253 mm [9.96 mil], leading to an initial stress intensity factor of 6.5 MPa(m)$^{1/2}$ [5.92 ksi(in)$^{1/2}$] at the initial stage of DHC. Eqs. (11–13) indicate that temperature is the most significant parameter affecting the time to failure for DHC in zirconium-based alloys. The time to leakage and the time to fracture by DHC after the assumed DHC initiation were computed using Eqs. (11–13), and the results are presented in Figure 16. The computed times to leakage and fracture are significantly reduced when the cladding temperature is increased from ambient temperature. The shortest times to leakage and failure are 0.4 and 3.3 hours, respectively; they both occur at a critical temperature, T_c, of 318.5 °C [605.3 °F], where the TSSP and hydrogen diffusion kinetics are high. The leakage time is about one-eighth

of the time to fracture. Both the leakage and fracture time increase at temperatures below T_c because the transport of hydrogen to the crack tip is reduced by a slower rate of hydrogen diffusion. At temperatures above T_c, the times to leakage and fracture increase because hydrogen solubility is increased and hydride formation at the crack tip is reduced. The results in Figure 16 indicate that the optimum temperature for the occurrence of DHC in zirconium alloys is in the temperature range of 280–320 °C [536–608 °F], near the tip of the nose of the T-t_f curve. The nose of the T-t_f curve is expected to vary with hydrogen content because both the TSSD and TSSP are functions of hydrogen content.

2.2.1. Texture effects

The DHC velocity at a given stress intensity factor, K, exhibits an orientation dependence. Results on Zr-2.5% Nb showed that the DHC velocity in the longitudinal or axial direction of the cladding is higher than that in the radial direction, as shown in Figure 17 for various temperatures [40,43]. There is, however, a discrepancy in the reported activation energies for the longitudinal and radial directions. Sagat, et al. [43] reported that the temperature dependency of DHC velocity and the activation energy in the longitudinal (axial) direction are smaller than those in the radial direction. On the other hand, the results by Kim, et al. [40] indicated similar activation energy values but lower DHC velocity values in both the longitudinal and radial directions than those reported by Sagat, et al. [43].

2.2.2. Effects of irradiation on DHC

The effects of irradiation on the DHC velocity in Zr-2.5% Nb have been investigated by Sagat and Puls [7]. An exservice pressure tube that had been irradiated at about 295 °C [563 °F] to a neutron fluence of approximately 7×10^{25} n/m^2 [7.54×10^{26} n/ft^2] (E > 1 MeV) was used for the study by hydrogen charging to 60 and 105 wt. ppm. For comparison, an as-manufactured pressure tube was hydrogen charged and homogenized at 400 °C [752 °F] to obtain 170 wt. ppm hydrogen. The DHC velocity measurements were performed at 295–345 °C [563–651 °F] under an initial K_I of 15–17 MPa(m)$^{1/2}$ [13.65–15.47 ksi(in)$^{1/2}$], which increased to about 23 MPa(m)$^{1/2}$ [20.93 ksi(in)$^{1/2}$] during subsequent crack growth. Figure 14 shows the DHC velocity for irradiated material compared against a database of axial crack velocity obtained using CANDU exservice irradiated pressure tubes [7]. The two sets of the DHC data, as shown in Figure 14, show slightly different slopes and activation energy values. Figure 14 also shows that the DHC data for the unirradiated materials are slightly lower than those of the irradiated material at a given temperature. For both materials, the maximum DHC velocity occurs at about 310–320 °C [<590–608 °F], and DHC ceases to occur at temperatures above 350 °C [662 °F]. Sagat, el al. [43] also measured the DHC velocity and K_{IH} in Zr-2.5% Nb that were irradiated at temperatures in the range of 250–290 °C [482–554 °F] in fast neutrons with a high energy (E > 1 MeV) and fluxes between 1.6×10^{17} and 1.8×10^{18} n/m^2·s [1.72×10^{18} and 1.94×10^{19} n/ft^2/s] to fluences between 0.01×10^{25} and 9.8×10^{25} n/m^2 [1.08×10^{24} and 1.06×10^{27} n/ft^2]. Their results indicated that

these levels of neutron irradiation reduced K_{IH} by about 20% [43] and increased the DHC velocity by a factor of five [7,43].

3. Crack-size distributions in zirconium cladding

Cracks in zirconium alloy cladding can originate from several possible sources, including (i) initial manufacturing defects, (ii) the oxide layer on the outer wall, (iii) the hydride layer or rim on the outer wall surface, and (iv) corrosion-induced cracks on the inner wall surfaces [16,19–21,26–36].

DOE estimates of the manufacturing defect size distribution in Zr cladding indicated that the crack depth may be described using an exponential distribution with a median (50%) crack depth of about 12 μm [0.47 mil] [48]. The exponential shape distribution was justified based on manufacturing defect surveys made by Sanders, et al. [88], while the median crack depth and the constants in the exponential shape function were deduced based on a review of PWR fuel performance that indicated there were 485 fuel assembly failures in 16,153 assemblies over a 5-year period for which data were available. Of the 485 fuel assemblies, 240 failures were caused by external events such as handling, debris, and grid fretting. The remaining 245 failures, which were assumed to be caused by initial cladding cracks that were at least 28% through wall or 160 μm [6.3 mil] deep, were used to estimate the possibility of pin failure, the initial defect size distribution, and a median (50%) initial defect size of 12 μm [0.47 mil].

The outer surfaces of the fuel rods are oxidized to form zirconium oxide and produce hydrogen as the fuel is irradiated in the reactor. As a result, the oxide thickness

on the Zircaloy-4 PWR cladding tubes increases with increasing burnup [89]. In particular, the maximum oxide thickness can be described in terms of a quadratic equation of burnup, reaching about 80–100 μm [3.15–3.94 mil] in Zircaloy-4 cladding tubes for a burnup of 60 GWd/MTU [89]. Analysis of the oxide thickness at a given level of burnup indicates that the oxide thickness in Zircaloy-4 cladding tubes follows a normal or lognormal distribution [66]. For ZrO_2, the fracture toughness is about 2.6 MPa$(m)^{1/2}$ [2.37 ksi$(in)^{1/2}$] [90]. Fracture of the ZrO_2 layer can produce a maximum crack depth of about 120 μm [4.73 mil] in high burnup fuel rod Zircaloy-4 cladding, and the corresponding crack size distribution would likely be normal or lognormal.

Hydrogen is produced and absorbed into the cladding as the outer cladding surface is oxidized [27,47,48]. The location of maximum hydrogen content corresponds to the location where the peak oxide layer occurs [48]. The hydrogen content is highest at the outer surface and decreases toward the center. At the peak oxide location, the region of enriched hydrogen content can extend more than 100 μm [3.94 mil] from the outer surface [25, Table 1]. For fuel rods discharged with burnup of 45–50 GWd/MTU, the amount of hydrogen collected at the outer surface exceeds the saturation limit, and as much as 120 ppm hydrogen is available for hydride formation in the form of radial hydrides or hydride blisters [23] when the cladding tubes are cooled from 350 °C to 45 °C [662 °F to 113 °F]. Because the fracture toughness of zirconium hydride {1–3 MPa $\sqrt{m}$ [0.91–2.73 ksi$(in)^{1/2}$]} is slightly less than that of zirconium oxide {≥ 2.6 MPa $\sqrt{m}$ [2.37 ksi$(in)^{1/2}$]}, cracking of the oxide layer at the maximum thickness location is likely to be followed by fracture of the hydride layer or hydride blister below the oxide layer [23]. Under this circumstance, the maximum crack length in the fuel rod cladding

would be on the order of 200 μm [7.87 mil]. Its subsequent growth by DHC if it occurs could lead to rod failure [23]. Detailed descriptions of cladding failure resulting from crack initiation at the outside wall are available in the literature [21,25,27,36]. Because of reduced corrosion and hydrogen pickup, a recent zirconium alloy (M5) is expected to exhibit smaller crack sizes resulting from oxide cracking or hydride blister fracture, compared to Zircaloy-2 and Zircaloy-4.

A structural integrity assessment of pressure tubes in CANDU reactors operating in South Korea was made by Park, et al. [11], who inspected 44 pressure tubes after 19 years of operation. For all the surveyed Zr-2.5% Nb cladding tubes, 8% were affected by flaws greater than those allowable by code {>150 μm [5.91 mil] depth} and about 60% were damaged by debris [11]. In addition, 30% of the inspected pressure tubes contacted the calandria tubes, even though no hydride blister was found in any of the tubes. The major cause of flaws was notchlike-shaped debris defects that intensified stresses at the notch root and showed propensity to hydride formation and DHC [11].

High burnup fuel cladding under power ramping conditions is exposed to locally enhanced residual and PCMI stresses not only at high temperatures, but also during subsequent slow cooling in the reactor. Under certain power ramp conditions, PCI can lead to high local cladding stresses and iodine-induced SCC [91], which has led to the use of a sponge zirconium liner or low friction coating in the inner wall of the fuel cladding for BWR as a remedial measure to prevent PCI failure [17]. The presence of these high local stresses can cause significant amounts of radial hydrides to form in local regions, sometimes leading to a pseudocleavage fracture known as RHA-DHC [25,36]. This type of DHC has been reported to initiate from the outside walls of Zircaloy-2 BWR fuel

cladding tested under power ramp and hold conditions with and without a primary defect [21,25,27,36]. According to Chung [25], inner wall cracks consistent with RHA-DHC are suspected to have occurred in a high burnup Zircaloy-4 PWR fuel during simulated RIA-like testing in a CABRI reactor (REP-Na1). Numerous cracks initiated from the inner diameter and propagated toward the outer diameter at significant depth. Figure 18 shows the axial distribution and depth of the inner wall cracks in the failed fuel cladding of REP-Na1. The crack depth ranged from 10 to 480 μm [0.39 to 18.9 mil] [25], and its distribution can be described in terms of a normal or lognormal distribution [66]. Many of the crack surfaces exhibited a brittle pseudocleavage appearance and sometimes were decorated with hydride debris, suggesting the DHC might have been the crack growth mechanism that caused cladding failure. Ramp testing of segmented fuel rods by Hayashi, et al. [36] clearly showed that the failure mechanism in higher burnup (56–61 GWd/MTU) segment rods is no longer one of pinhole perforation as observed in low burnup (<43 GWd/MTU), but a RHA-DHC process resulting from a combination of high PCMI stresses and radially oriented hydrides precipitated at the outer rim during ramp testing. The high PCMI stresses produce a variety of hydride microstructures in high burnup fuel rods that are susceptible to RHA-DHC under in-reactor and ex-reactor conditions, because the hydrided microstructure is retained in the cladding. Hayashi, et al. reported interface bonding between pellets and cladding tubes [36], which may retain parts of the PCMI stresses after cooling. In many cases, the PCMI stresses are sufficiently high to initiate RHA-DHC and propagate the crack to cause axial fracture in single-step ramp tests, as reported by Hayashi, et al. [36]. It was also considered that stress could be relieved by circumferential cracks at the cladding and the fuels. These

potential in-reactor failure mechanisms in high burnup cladding tubes are schematically illustrated in Figure 19, which includes (i) oxidation of the outer wall surface and oxide cracking, (ii) formation of a hydride blister beneath the zirconium oxide layer and blister cracking, (iii) radial hydride formation ahead of the hydride blister due to hydride growth or hydride reorientation, (iv) uniform corrosion of the inner wall surface and cracking of the corrosion products (predominantly oxides), and (v) DHC. The first four fracture mechanisms serve as the crack initiation processes at the outer and inner walls of the cladding. Once initiated, the outer wall and inner wall cracks can grow by DHC if the stress intensity factor exceeds the K_{IH} growth threshold.

DHC has been a concern for CANDU reactors. Operators of CANDU reactors in Canada [10] and South Korea [2] have implemented (i) inspection and survey procedures for detecting defects and hydride-initiated cracks in pressure tubes and (ii) a fracture mechanics methodology and a leak-before-break requirement for predicting the pressure tube failure resulting from DHC. A multinational program for characterizing DHC growth to kinetics of Zr-2.5% Nb in nuclear reactors of pressure tubes was conducted under the auspices of the IAEA [15].

The causes and mitigation methods for fuel failure in BWRs were reviewed in an IAEA Technical Meeting [18]. Kim [23] reported that primary and secondary hydriding in Zircaloy-2 cladding played critical roles in recent failures of nuclear fuel rods in Korean BWR power plants. The roles of hydrides in these rod failures are similar to those reported by several investigators [16, 19–22], as summarized earlier in Section 1.0. The multitude of field evidence indicates that DHC has occurred in pressure and cladding tubes during power operations, even though its occurrence might not always lead to rod

fracture, because (i) a low-friction coating or a sponge-zirconium liner is used between pellets and cladding [15], (ii) an early detection and intervention program has succeeded [2], and (iii) the transient stresses that drive DHC in cladding tubes occur only during off-normal conditions. However, Hayashi, et al. [36] recently observed hydrided-induced failure in Zircaloy-2 cladding during ramp tests of high burnup BWR segment rods ranging from 43 to 61 GWd/MTU. At high burnups (56 and 61 GWd/MTU), the segmented rods failed by a RHA-DHC process in Zircaloy-2 cladding tubes during single-step ramp tests. This failure mechanism, which was attributed to high PCMI stresses and hydrogen contents at high burnup, may potentially limit high burnup operation in BWRs [18] because the high PCMI stresses can produce a variety of hydrided microstructures that are susceptible to hydride fracture and DHC under subsequent tensile loading during service. The cladding stress responsible for DHC during service in the reactor or at a waste repository is explored in detail in the next section.

4. Cladding stresses

The cladding stress under normal in-reactor conditions arises mainly from the internal gas pressure inside the cladding tubes. While the gas pressure increases with burnup and fission gas release fraction, there is a general consensus that the cladding stress due to internal gas pressure is sufficiently low that the growth threshold for DHC, K_{IH}, would not be exceeded unless the cladding tube contained a deep crack [27,47,49,50]. On the other hand, the transient stresses encountered in the cladding

resulting from interaction with the fuel during in-reactor power ramps can be sufficiently high that they are likely to instigate DHC and could well lead to cladding failure under certain circumstances. The next section summarizes the current status of cladding stresses computation arising from gas pressure and PCMI.

4.1. Gas pressure

The cladding stress depends on the temperature and quantity of fission gases in the plenum, which in turn depends on the burnup and fission gas release fraction. The hoop stress in cladding was computed on the basis of the thin-wall approximation for a burnup ranging from 25–60 GWd/MTU and plenum pressure ranging from 3.41 MPa to 5.51 MPa [0.5 to 0.8 ksi]. The gas pressure (P) of fission gas and helium is given by [48]

(14)

$$P = 3.1br \times Mkg \times T \times FGR \ / (273 \cdot Fvol)$$

where P is fission gas pressure in MPa, Mkg is the mass of uranium in one fuel rod in Kg, T is absolute temperature in K, FGR is fission gas release, br is burnup in GWd/MTU, and Fvol is the rod file volume in cm^3. The stress (σ_p) due to the fission gas pressure was computed according to the expression given by [48]

$$\sigma_h = \frac{PD_I}{2[t - t_{ox} - a]} \tag{15}$$

where D_I is the cladding inside diameter, a is crack depth, t is cladding wall thickness, and t_{ox} is the oxide thickness. The cladding stresses are in the range of 26–48 MPa [3.77–6.96 ksi] and 36–66 MPa [5.22–9.57 ksi] at room temperature, respectively, for cladding wall thickness {5.6–49 mm [0.22–1.93 in]} and corresponding plenum pressures of 3.41–5.5 MPa [0.5–0.8 ksi] with a median crack size {a = 12 μm [0.47 mil]} and the maximum {a = 160 μm [6.3 mil]} and excluding oxide thickness ($t_{ox} = 0$), according to [48]. Pescatore, et al. [92] gave both the average and maximum hoop stresses for PWR fuels from several sources. At 320 °C [608 ºF], the average hoop stress value ranged from 24 to 62 MPa [3.5 to 0 ksi], and the maximum value was up to 134 MPa [19.4 ksi] for less than 1% of the total rods.

4.2. Pellet-cladding mechanical interaction

The cladding stresses due to fission gas release are relatively low under normal conditions. During power ramp, the cladding stress increases because of mechanical interaction between the fuel pellets and the cladding (Figure 20). The mechanism of PCMI, which is well established [91], results from the thermal expansion and crack-induced volumetric increase of the fuel pellets during thermal transients. The thermal stresses lead to fuel fragmentation and increases in the pellet diameter. Creep of the cladding results in local ridges in the cladding tube as the fuel pellets change to an "hourglass" shape [54]. Early analyses of the PCMI stresses were reviewed by Cox [91], who concluded that stresses generated by PCMI during in-reactor power ramp are high, and the corresponding stress intensity factors are comparable to those measured in the

laboratory. The stress concentration factors at cladding tube ridges were computed by Ranjan, et al. [93] using an elastic axisymmetric shell analysis of the cladding by an asymptotic expansion method that yielded closed-form solutions. Elastic concentration factors on the order of 1.1 to 2.8 were obtained for the circumferential stresses at the ridges, depending on the ridge height and the strain state developed at the ridge.

Recent PCMI analyses are elastic–plastic analyses based on FEM with complex constitutive models that include treatment of plasticity, creep, stress relaxation, and irradiation effects [53–61]. These FEM analyses are typically two-dimensional (2D) analyses. More recent 3D FEM analyses provided better descriptions of the time dependent evolution of the local transient stresses at various locations in the cladding tubes during power ramp including various hold times at the ramp terminal level.

Using an elastic–viscoplastic constitutive model that treats plasticity, creep, stress relaxation, anisotropic, and irradiation effects, Schäffler, et al. [57] computed the cladding stresses in a Zircaloy-4 cladding tube during a PWR power ramp transient using simulated loading conditions by imposing a circumferential strain rate of 2×10^{-5} s^{-1} followed by a relaxation period. Figure 21(a) shows the computed hoop stress in the cladding compared to the corresponding biaxial tensile tests at 350 °C [662 °F]. The cladding reaches as high as 600 MPa [87 ksi], but decreases quickly in the first 20 minutes and saturates to about 410–450 MPa [59.5–65.3 ksi] after 100 minutes into the relaxation or strain hold period. This stress transient will be referred to as Type I, which is characterized by a stable, relaxed stress that is higher than that required to meet $K > K_{IH}$ and cause DHC.

Suzuki and Uetsuka [58] developed a fuel performance code, FEMAXI-6, for analyzing light water reactor (LWR) fuel rod behaviors in normal and transient conditions. The FEM-based code, which has incorporated thermal and mechanical models for treating thermal conductivity degradation and pellet-clad bonding in high burnup fuel rods, analyzes the PCMI stresses induced by swelling in high burnup BWR-type fuel rods. Their calculations indicated that the cladding hoop stress transient during a power ramp showed a peak stress of 350 MPa [50.8 ksi], which relaxed quickly and became stable at 260–300 MPa [37.7–43.5 ksi] over a time period of about 120 minutes. The corresponding cladding temperature was 676K [712.4 ºF] at the inner surface and 598K [572 ºF] at the outer surface during the ramp. Bonding between the clad and pellets increased the hoop stress by 17% and also increased the biaxial stress state. Suzuki and Uetsuka [58] also reported that the peak value in the stress transient was sensitive to the creep model chosen for the stress analysis. A hoop stress as high as 600 MPa [87 ksi] had been obtained depending on the creep model. The results of Suzuki and Uetsuka [58] are thus comparable to those reported by Schäffler, et al [57], both in the transient stress levels and the length of the relaxation period.

Using the FEM code TOUTATIS, Brochard, et al. [53] computed and reported the cladding stresses for a rod irradiated for two annual PWR operating cycles and subjected to a power increase from 240 to 450 W/cm [94.1 to 177.2 W/in] in about 20 minutes with a hold time of 100 minutes at the ramp terminal level. The transient inner clad hoop stress during the power ramp is presented in Figure 21(b). The shape of the stress evolution curve is similar to that shown in Figure 21(a), but the stresses are lower. The

time period over which the transient stress persists is shorter and lasts for 100 minutes, which corresponds to the hold time at the ramp terminal level.

More recently, Brochard, et al. [54] computed the cladding stresses for a rod irradiated for two annual PWR operating cycles and subjected to a power increase from 200 to 450 W/cm [78.7 to 177.2 W/in] in 2.5 minutes with an unspecified hold time at the ramp terminal level. Their results for the cladding circumference stress at the interpellet level, which are shown in Figure 21(c), indicate that the cladding stress is fairly low at the initial stage of the power ramp when the gap still exists between the fuel pellets and the cladding tube. The cladding stress builds up quickly once the gap between cladding and pellets closes under the combined effect of cladding creep and pellet swelling [54]. The cladding circumferential stress reaches a maximum value of 350 MPa [50.8 ksi] and then decreases quickly to a lower value of 210 MPa [30.5 ksi] after 7 minutes at the ramp terminal level. For this case, the stress concentration factor at the cladding is about 1.34–1.43 based on experimentally measured values of 0.4–0.6 for the coefficient of friction between pellet and cladding. The stress transients shown in Figures 21(b) and (c) will be referred to as Type II. In contrast to the Type I stress transient, Type II meets the condition of $K > K_{IH}$ for only a short time. Relaxation of the local stress occurs quickly, and the stabilized stress is below that required to exceed K_{IH}; therefore, Type II transients lead to intermittent crack growth and crack arrest.

The magnitude and the duration of the transient PCMI stress are sensitive to a number of factors [53,54,59], including (i) pellet geometry such as pellet shape, the height-to-diameter ratio, fuel swelling, and pellet fragmentation; (ii) thermomechanical loading history during power ramp and the duration of hold time at the ramp terminal

level; (iii) modeling assumptions such as the axial constraint and the constitutive model utilized to treat time- and temperature-dependent inelastic flow resulting from plasticity, creep, stress relaxation, swelling, and irradiation effects; and (iv) cladding characteristics and material parameters such as wall thickness, thermal properties, elastic–viscoplastic properties, pellet–pellet friction, and the coefficient of friction at the fuel cladding interface that are used in the computation.

Systematic studies of the sensitivity of the PCMI stress to structural and material parameters were performed by Brochard, et al. [53,54], who identified the axial constraint, the pellet height, the pellet fragmentation and the hollow pellet as important variables affecting the PCMI stress. Retel, et al. [59] evaluated the separate influences of structural and materials parameter variability on the PCMI in a fuel rod subjected to two PWR cycles with a power equal to about 200 W/cm [78.7 W/in] followed by a power transient with a maximum power equal to 412 W/cm [162.2 W/in]. In the 3D FEM simulations of this set of baseline ramping conditions, the number of axial and radial pellet cracks, pellet fragment size, relative fragment displacement, degrees of symmetry in the fragment configuration, pellet–pellet friction, and pellet–cladding friction were varied systematically. Among these six parameters, Retel, et al. [59] found the pellet-cladding friction coefficient and the number of axial pellet cracks are the most important in increasing the cladding stress. The maximum cladding stress obtained by Retel, et al. [59] was in the range of 300–400 MPa [43.5–58 ksi] for a pellet-cladding friction coefficient of 0–0.2, with cladding temperatures of 440 ºC [824 ºF] and 366 ºC [691 ºF] at inner and outer cladding walls, respectively.

Because of the large number of structural and material variables involved, it is difficult to assess the validity of the computed PCMI transient stress from a particular computation unless the computational results are verified by relevant experimental data. Bourreau, et al. [56] performed power ramp tests on PWR fuel rods with fuel segments extracted from the same fuel rod. Designed by Connectors International, the original segmented fuel rod contained UO_2 pellets that were initially enriched up to 4.5% in ^{235}U and irradiated during two cycles in an 900MW PWR to reach an average burnup of 23.8 GWd/MTU. Three segments of the original fuel rod were extracted, refabricated into subrods, and used in subsequent power ramp tests with four different ramp power histories and hold times at the maximum power or terminal ramp level (TRL). The hold times at the TRL were 0 seconds (no hold time), 16.5 minutes, and 12 hours 19 minutes. Cladding deformations were measured during the power ramping, and the power ramp tests were modeled using 2D and 3D fuel modeling codes. The experimental results of cladding deformation were correlated with power density and compared against FEM computations. The experimental results indicated that the hold time at the TRL exerted a significant effect on the cladding deformation and stresses in the power ramp tests. For all ramp tests, no rod failure occurred during or after the power ramp experiments. A good correlation was observed between the local power during irradiation and the cladding deformation measured after the ramp tests. Comparisons of post-irradiation measurements performed on the three tubes indicated that the cladding deformation increased with the hold time at TRL. The hold time particularly affected the evolution of secondary ridges. Many features of the power ramp tests, such as the axial power profile on cladding diameter variations during the power transients, were simulated by the

provided FEM codes that the analysis used for preexisting oxide fragmentation. In Bourreau, et al. [56], 2D modeling satisfactorily reproduced cladding diameter changes off ridges, while 3D modeling correctly simulated primary ridge changes and allowed secondary ridge buildup.

Direct evidence for the presence of a high PCMI stress was provided by the power ramp testing of BWR segmented rods conducted by Hayashi, et al. [36]. BWR 8 × 8 fuel assemblies with segmented rods of Zircaloy-2 cladding tubes were irradiated up to 5 cycles. Ramp tests of 25 segments with burnup ranging from 43 to 61 GWD/MTU were then conducted in a test reactor. One segment rod irradiated for 3 cycles (43 GWd/MTU) failed by a single-step ramp test after 9 minutes at a terminal ramp power of 614 W/cm with a pinhole caused by PCI and SCC. One segment rod irradiated for 4 cycles (56 GWd/MTU) failed by a single ramp test after 149 minutes at 551W/cm with an outer side axial crack. Nine segment rods were irradiated for 5 cycles (61 GWd/MTU). Two of these rods failed by a single-step ramp test after 68–100 minutes at about 421–428 W/cm, and one failed by a stair ramp test at 446 W/cm, all with outer axial cracks. According to Hayashi, et al. [36], the increase in hydrogen contents and PCMI stresses with increasing burnups led to the formation of radial hydrides at the outer rim and a change in the operative failure mechanisms in the cladding tubes. Specifically, the failure mechanism in the segment rods was PCI/SCC at low burnups (< 43 GWd/MTU). At high burnups (56 and 62 GWD/MTU), rod failure was caused by a combination of high PCMI stresses and radial-hydride-assisted DHC growth during ramp tests. Cladding cracks initiated by fracture of radial hydrides at the outer rim and propagated inward by DHC to the inside wall, followed by DHC in the axial directions and finally ductile

fracture. Posttest examination of the pellet-cladding interface revealed a bonding layer formed between the pellet and the cladding by mutual diffusion of UO_2 and ZrO_2 [36]. The observed times to rod failure in the power ramp tests ranged from 9 to 149 minutes, which are consistent with the durations (7 to 130 minutes) of PCMI transient stresses predicted by Brochard, et al. [53,54].

It is well known that the presence of a large tensile hoop stress during TSSP would align the hydrides along the radial direction of the cladding tube, forming radial hydrides. At certain temperatures, circumferential hydrides in zirconium cladding tubes can reorient under a tensile hoop stress to form radial hydride, providing that the tensile stress exceeds the critical stress for hydride reorientation. Experimental data of the critical stress for hydride reorientation were reviewed by Chung [25], and additional data needs in this area were discussed by Einziger, et al. [94]. Previously, Chung [25] determined empirically that the critical tensile for hydride reorientation is about 100 MPa and its value is relatively insensitive to temperature, as shown in Figure 22. Subsequently, Ferry and Poinssot [95] suggested that the critical stress for hydride reorientation may not be a constant, but its value may increase with decreasing temperature, as shown in Figure 22. More recently, Chu, et al. [96] presented a theoretical analysis that showed the threshold stress for hydride reorientation decreases with increasing temperature and hydrogen content in a complex manner. The results for Zircaloy-4 with 200 wt. ppm H_2 are shown in Figure 22. Daum, et al. [97] recently reported that the critical stresses for hydride reorientation of nonirradiated and high burnup Zircaloy-2 are 80 ± 10 MPa and 75 ± 10 MPa, respectively. A comparison of the threshold stress boundaries against all of the available experimental data in Figure 22

indicates that Chung's empirical threshold stress boundary gives the best agreement, even though a few data points at temperatures of hydride reorientation at temperatures ≥ 400 °C fall below the threshold line. The temperature during in-reactor power ramp is in the range of 300–350 ºC. Figure 22 shows that hydride reorientation would not occur at temperatures less than 400 °C when the cladding stress is below the 90 MPa limit [94]. At temperatures ≥ 400 °C, hydride reorientation may occur at stresses below the 90 MPa stress limit, but more experimental data are needed [94]. On the other hand, the PCMI transient stresses during in-reactor power ramps are in the range of 200–600 MPa. The high PCMI stresses are sufficiently high to cause hydride reorientation in the cladding tubes. A variety of hydride microstructures have been reported, including hydride blisters, hydride rims, sunburst hydrides, and radial hydrides [16,19–21,26–36]. Once formed during power ramps, the hydride microstructures may remain in the cladding tubes and probably persist after the fuel rods are removed from the reactors. Thus, there are considerable uncertainties on the initial cladding conditions (crack distribution, hydride orientation, and morphology) before the fuel rods are emplaced in a repository.

4.3. Potential repository environment

For fuel rods in a potential waste repository environment, the cladding stress was computed to be in the range of 60–100 MPa [8.7–14.5 ksi], based on consideration of the internal rod pressure due to fission gas release and a uniform cladding diameter [48,98]. This estimate of the cladding stress is likely a lower bound because nonuniform cladding diameter changes induced by PCMI and stress concentration at the ridges was not taken into account in the previous stress calculation.

Computing the local hoop stress at the ridges in cladding tubes in a potential repository requires knowledge of (i) the anticipated temperature gradient between the pellet fragments and cladding, (ii) swelling or the presence of voids in the fuels [61], and (iii) bonding or welding between the fuel fragments and cladding wall [36,61]. The latter two phenomena could prevent the fuel pellets from separating from the cladding, thereby allowing a high local stress to be maintained at the ridges after a power ramp [59]. One possible estimate of the upper bound hoop stress in cladding tubes after service may be the relaxed stable hoop stress in the cladding after an in-reactor power ramp, because the temperature gradient, the extent of fuel expansion, and the contact between fuel and cladding are at the maximum levels. The relaxed PCMI stress values range from 200–400 MPa [29–58 ksi] based on the computational results of Brochard, et al. [53,54], Suzuki and Uetsuka [58], and Schäffler, et al. [57]. The actual unrelaxed PCMI stresses may be less than 200–400 MPa [29–58 ksi], depending on the stress relaxation processes and the bonding between pellet and cladding. Over a period of 10^4–10^6 years, cladding tubes in a potential repository might encounter one or more seismic events and impact loading from rockfalls that can cause transient loading on the cladding in successive bursts. The transient cladding stress during a seismic event or a rockfall is expected to lead to a high stress intensity factor at an existing crack in the cladding in a very short time. The general characteristics of the K profiles for these transient stress fields would be similar, but with different amplitudes, durations, and stress relaxation times. For impact loading, subsequent DHC growth may be feasible under the stress transient results in a fracture of the surface oxide layer, hydride blister or rim, or radial hydrides to create or extend a crack so that $K > K_{IH}$. Under this circumstance, DHC may occur after a rock

fall event; the DHC growth kinetics would then be dictated by the duration of the transient stress, the crack lengths, the cladding temperature, the cooling rate, and the properties of the degraded cladding.

5. DHC in fuel rod cladding during in-reactor power ramps

5.1. Internal gas pressure

The propensity to DHC in fuel rod cladding tubes due to internal pressure and local transient stresses induced by PCMI is considered in this section. In particular, the plot of critical stress versus crack length shown in Figure 7 for Zr-2.5% Nb has been extended to zircaloy fuel cladding because comparable experimental data for Zircaloy-2 or Zircaloy-4 are incomplete and are insufficient for statistical analysis. As shown in Figure 6, experimental results on Zircaloy-2 tubing by Huang and Mills [38] indicated that the K_{IH} value for Zircaloy-2 tubing ranged from 5.2 to 8.4 MPa$(m)^{1/2}$ [4.7 to 7.6 ksi$(in)^{1/2}$], compared to 5.5 to 9 MPa$(m)^{1/2}$ [5 to 8.2 ksi$(in)^{1/2}$] for Zr-2.5% Nb materials with closely matched crystallographic textures. The activation energy for DHC in Zircaloy-2 was determined to be 65.3 kJ/mol [15.60 kcal/mol] [38], which is essentially identical to the experimental value of 65.5 kJ/mol [15.65 kcal/mol] for Zr-2.5% Nb [12]. Mills and Huang [38] indicated that the DHC growth rates in Zircaloy-2 tubes were comparable to those observed in Zr-2.5% Nb tubes with similar crystallographic textures. Because the DHC properties are similar, extending Figure 7 for Zr-2.5% Nb to Zircaloy-2, therefore, requires only the assumption that the fracture strengths for hydrides in Zr-

2.5% Nb are comparable to those for fracture of hydrides in Zircaloy-2. On this basis, the calculated curves based on large crack K_{IH} thresholds of 5.36 and 12 MPa(m)$^{1/2}$ [4.9 and 10.9 ksi(in)$^{1/2}$] are applicable to both Zircaloy-2 and Zr-2.5% Nb, because the actual experimental data of these two alloys lie within these two limits. There is a general consensus that the cladding stress level due to internal fission gas pressure {60–100 MPa [8.7–14.5 ksi]} results in a stress intensity level that is on the order of 0.5–2 MPa(m)$^{1/2}$ [0.46–1.82 ksi(in)$^{1/2}$], which is lower than the K_{IH} of 5 MPa(m)$^{1/2}$ [4.6 ksi(in)$^{1/2}$] required for the onset of DHC growth. Hence, DHC by internal gas pressure alone is considered unlikely, as indicated earlier, when the initial crack sizes are estimated on the basis of the size of manufacturing defects in the cladding. Figure 23 compares the cladding stresses against the critical stresses for the onset of DHC for semicircular cracks with large crack thresholds of 5.38 MPa$\sqrt{m}$ [4.9 ksi(in)$^{1/2}$] and 12 MPa$\sqrt{m}$ [10.9 ksi(in)$^{1/2}$] and the corresponding small crack threshold stresses. The nominal stresses in the cladding due to the internal gas pressure are well below the critical threshold stresses required to cause DHC in either Zr-2.5%Nb or Zircaloy-2.

5.2. Transient stress

The transient stress during power ramps can be high and sufficient to cause DHC. The transient PCMI stresses during power ramp are compared with the threshold stress in Figure 23. The comparison indicates that the PCMI transient stress exceeds the threshold stress for DHC for crack depths greater than 80–120 μm [3.2–4.7 mil]. Applying the transient hoop stresses computed by Brochard et al. [53,54], Suzuki and Uetsuka [58],

and Schäffler et al. [57] to DHC indicated that the extent of DHC growth critically depends on the time duration at which the local stress intensity exceeds the K_{IH}. The DHC growth calculations were performed using a semicircular crack assumption. The cladding tube was assumed to contain a 100-μm [3.9-mil]-thick oxide layer with a 150-μm [5.9-mil] hydride blister layer formed beneath the oxide layer. The initial crack depth was taken to half of the oxide thickness. The oxide layer failed when $K > K_{IC}^{oxide}$ and the crack depth was set to the oxide thickness. Similarly, the hydride layer failed when $K > K_{IC}^{hydride}$ and the crack depth was increased by the layer thickness of the hydride blister. DHC growth continued if $K > K_{IH}$ under the stress transient or ceased to occur if $K \leq K_{IH}$. Figure 24 shows the DHC growth results for the three stress transients at 318 ºC [604 ºF]. For DHC growth under a transient stress with a short duration of 7 minutes (dashed line, Figure 24), the amount of DHC growth is ≈ 108 μm [4.3 mil] and crack growth ceases after K drops below K_{IH} (Type II transient) resulting in equal values of crack length (a) and crack depth (b). For a transient stress duration of 130 minutes (solid line, Figure 24), the amount of DHC growth is about 0.1776 mm [6.9 mil] and the crack depth (b) exceeded the wall thickness, leading to leakage but not failure, because the crack length (a) is still below the critical crack length for a K_{IC} of 70 MPa$(m)^{1/2}$ [63.7 ksi$(in)^{1/2}$]. In comparison, DHC growth proceeds throughout the entire wall thickness, and the crack length exceeds the critical crack length for K_{IC} = 70 MPa$(m)^{1/2}$ [63.7 ksi$(in)^{1/2}$] when the transient stress duration is 330 minutes (dot-dashed line). In this case, $K > K_{IH}$ for the entire duration of the stress transient (Type I) and $K \geq K_{IC}$ at time ≥ 200 minutes. It is evident that DHC growth during in-reactor power ramp is an intermittent process that depends on the induced stress or K amplitude, the duration of the transient, the cladding

temperature, and the frequency of ramping. DHC growth occurs as long as the induced K level exceeds K_{IH}. The crack growth rate is fastest at about 318–320 °C [604–608 °F] for Zr-2.5% Nb. Thus the amounts of DHC crack extension are expected to increase with increasing cumulative times of high stress transients or the number of power ramps experienced by the fuel rod.

In an overview paper, Chung [25] summarized several instances involving failure of high burnup cladding. Under various usage conditions, high burnup cladding is subjected to PCMI stresses not only at high temperatures {380–420 °C [716–788 °F]}, but also during subsequent slow cooling to a lower temperature {e.g., 200 °C [392 °F]}. The transient local stresses can induce the precipitation of radial hydrides in significant amounts in some local regions, sometimes leading to cleavage fracture and RHA-DHC. Inner wall cracks were found in a high burnup Zircaloy-4 PWR fuel during pretest heating of a simulated RIA-like pulse test. The length of the inner wall cracks ranged from 20–480 μm [0.79–18.9 mil], and many were partially covered with hydrides [25]. Based on the metallographic and fractographic characteristics of the inner wall cracks, Chung [25] suspected that these cracks might have been caused by RHA-DHC. This is because numerous local regions were found to contain radial hydrides that were in tight contact with the pellet-cladding bonding layer where high transient tensile stresses could be induced by PCMI. Brittle cracks consistent with RHA-DHC were reported at the outer and inner walls of Zircaloy-2 BWR fuel cladding tested under a power ramp with a hold time for tubes with and without a primary defect [20,22,36]. In nonlined BWR failed rods with Zircaloy-2 cladding, Lin, et al. [20] observed a long {287 μm [11.3 mil]} outside-wall crack with radial hydrides at the crack tip. In addition, radial hydrides were

observed to emanate from the outer and the inner cladding walls. The lengths of the radial hydrides that emanated from an outer wall were on the order of 300–390 μm [11.8–15.3 mil], compared to 90–240 μm [3.5–9.4 mil] from an inner wall. Cheng, et al. [21] reported hydride cracks of various lengths {50–200 μm [2–7.9 mil]} initiated from the outer and inner walls in both Zr-lined and nonlined Zircaloy-2 cladding tubes. Localized oxide layer on the order of 70–150 μm [2.8–5.9 mil] in thickness was observed [22]. A hydride rim over 80 μm [3.1 mil] thick was observed on the outer surface. Radial hydrides that emanated from the hydride rim ranged from 160 to 340 μm [6.3–13.4 mil] in length. Nonlined Zircaloy-2 was also prone to the formation sunburst hydrides below the hydride rim. Hayashi, et al. [36] also reported that brittle cracks initiated from radial hydrides formed at the outer walls of Zircaloy-2 cladding tubes of high burnup fuel rods. The crack size ranged from 40 to 330 μm [1.6–13 mil] in the through-thickness direction. Some of the observed cracks propagated entirely through the wall thickness and became axial cracks. The length of the axial cracks was 700 μm and higher. Hayashi, et al. [36] identified RHA-DHC as the cladding failure mechanism by showing the presence of radial hydrides at the crack tip. They also reported that the oxide thickness ranged from 30 to 100 μm [1.2–3.9 mil] and the length of the radial hydrides was about 70 μm [2.8 mil] [36].

The transient nature of the PCMI stresses dictates that DHC growth during power ramp does not lead to immediate cladding failure or the development of a leak in the cladding. Instead, the damage process appears to involve the accumulation of small increments of DHC growth over a long time or after numerous power-ramping events. The power ramp transient stresses produce two effects that can affect the integrity of

cladding tubes under subsequent repository conditions: (i) the generation of local residual stresses at ridges in cladding under normal operating conditions in reactors and repositories and (ii) a distribution of defect or crack sizes that evolve with time and are considerably larger than the initial manufacturing defect sizes. Both the local stress and the crack size distribution can significantly affect the propensity to DHC growth in cladding tubes in a repository environment, illustrated by the box in Figure 23. The relaxed PCMI stresses computed by Brochard, et al. [53,54] and Suzuki and Uetsuka [58] are about 100–300 MPa [14.5–43.5 ksi], and the corresponding crack depths are 50–250 μm [1.97–9.84 mil]. The larger crack depth is based on a 120-μm [4.72-mil] oxide crack and a 130-μm [5.12-mil] hydride crack formed beneath the oxide layer by DHC or fracture of a hydride blister during power ramps. These oxide thicknesses and hydride blister sizes have been estimated on the basis of the experimental observations by Cheng, et al. [21] on Zircaloy-2 that showed the localized oxide layer thickness was about 70–150 μm [2.8–5.9 mil]. A hydride rim over 80 μm [3.1 mil] thick formed on the outside surface with radial hydrides 160–340 μm [6.3–13.4 mil] in length that emanated from the hydride rim [22]. For a crack depth of 250 μm [9.8 mil], the relaxed PCMI stresses are comparable to those required to start DHC. In contrast, DHC does not occur at stresses below 200 MPa for K_{IH} = 5.36 MPa$(m)^{1/2}$ [4.88 ksi$(in)^{1/2}$]. For zirconium alloys with low oxide thickness and hydrogen pickup (e.g., M5), the initial crack depth may be substantially less than 250 μm [9.8 mil]; DHC would not be feasible at a cladding stress of 200 MPa [29 ksi].

5.2.1. Type I transient stress during a cooldown

Without the local stresses at the ridges, the cladding hoop stresses from the internal gas pressure alone may not be sufficiently high to cause DHC in cladding tubes under repository conditions. To produce substantial DHC, the local stress intensity factor at cladding must exceed K_{IH} for a sufficient time period without being relaxed below this critical value. Of the two transient stress types, the one modeled by Schäffler, et al. [57] and another described for reactor ramp-up by Suzuki and Uetsuka [58] is capable of producing substantial DHC growth because of an extended duration where $K > K_{IH.}$ For cladding tubes under potential repository conditions, the amount of crack extension generated by this type of local stress distribution also depends on the cladding temperature and cooling rate. For DHC under a cooldown from a given temperature {e.g., 320 °C [608 °F]}, the crack extension per unit temperature change, dT, can be derived from Eq. (11) and is given by

$$\frac{da}{dT} = \frac{V_o}{\dot{T}} exp\left[\frac{-Q_{DHC}}{RT}\right] \tag{16}$$

for T <590K and

$$\frac{da}{dT} = \frac{V_o^{\,h}}{\dot{T}} \exp\left[\frac{Q_h}{RT}\right] \quad \text{for T > 590K} \tag{17}$$

where $\dot{T}$ is the cooling rate. The importance of the cooling rate on the DHC growth response is illustrated in Figure 25, which plots *da/dT* as a function of temperature for three different cooling rates for Zr-2.5% Nb with V_o = 0.14 m/s [0.459 ft/s], R = 8.31 J/mol/K [1.98 cal/mol/K], and Q_{DHC} = 65.5 kJ/mol [15.65 kcal/mol] for T <318 °C [604 °F] where TSSP is controlled by diffusion kinetics. For T >318 °C [604 °F] where hydrogen solubility controls TSSP, V_o^h = 8.83E–42 m/s [2.897×10^{-41} ft/s] and Q_h = 389 kJ/mol [92.93 kcal/mol]. Figure 25 shows that the amount of DHC growth per temperature change is the highest at about 318 °C [604 °F] and decreases with both increasing and decreasing temperatures for all three cooling rates. DHC growth is essentially nonexistent when the temperature is above 360 °C [680 °F] because hydrogen is in solid solution and hydrides cannot be formed at the crack tip. DHC growth is very limited when the temperature drops below 150 °C [302 °F] because of slow diffusion kinetics. A high cooling rate reduces the DHC growth because there is less time for the crack to propagate during the prescribed cooling rate. Conversely, a slow cooling rate allows more time for DHC to occur. The cumulative crack extension by DHC during the cooldown is given by the area under the curves shown in Figure 25 and is obtained by integrating or summing Eqs. (16 and 17) over the temperature range from T_1 to T_3. T_1 and T_3 are the initial, intermediate, and final temperatures in the cooldown cycle leading to

$$\Delta a = \int_{T_1}^{T_2} \frac{V_o}{\dot{T}} \exp\left(\frac{-Q_{DHC}}{RT}\right) dT + \int_{T_2}^{T_3} \frac{V_o^h}{\dot{T}} \exp\left(\frac{Q_h}{RT}\right) dT \qquad (18)$$

The results for cooling from T_3 = 400 °C [752 °F] to T_1 = 0 °C [32 °F] with T_2 = 318 °C [604 °F] are summarized in Table 3.

Table 3. DHC Crack Extensions and Time of Growth as a Function of Cooling Rates

Cooling Rate, °C/s [°F/s]	Δa, mm [mil] ($T_3 \rightarrow T_2$)	Δa, mm [mil] ($T_2 \rightarrow T_1$)	Δa, mm [mil] ($T_3 \rightarrow T_1$)	Time (hrs)
0.1 [0.18]	0.0109 [0.43]	0.0889 [13.5]	0.0998 [3.93]	1.11
0.01 [0.018]	0.1807 [7.11]	0.8888 [35.0]	1.0695 [42.1]	11.11
0.001 [0.0018]	1.8075 [71.2]	8.8876 [350.0]	10.695 [421]	111.11

Table 3 shows that the amount of DHC extension is about 0.1 mm [3.94 mil] for a cooling rate of 0.1 ºC/s [0.18 ºF/s], and the time spent in DHC growth is 1.1 hours. When the cooling rate is reduced to 0.01 ºC/s [0.018 ºF/s], the time for DHC growth increases to 11.11 hours, and the amount of DHC extension increases to 1.07 mm [42.1 mil]. Further decrease in the cooling rate to 0.001 ºC/s [0.0018 ºF/s] increases the DHC time to 111 hours and the amount of DHC extension to 10.7 mm [0.42 in].

5.2.2. Type II transient stress

For Type II transient stress, the peak stress intensity factor exceeds the K_{IH} value and results in DHC growth for a short time period during a power ramp. After the power ramp is completed, the equilibrium stress is stabilized at a stress intensity factor, K, that drops below the K_{IH} and terminates DHC growth. Under this circumstance, DHC remains dormant until either the local stress is increased or the K_{IH} value is equivalently reduced so that $K > K_{IH.}$ When $K > K_{IH}$, DHC resumes and the crack growth process can be analyzed using the procedure described for treating Type I transient stress. When $K < K_{IH}$, DHC ceases and the crack length remains constant until another transient stress cycle causes the K value to exceed K_{IH} again. This is shown in Figure 24, which presents the results of computations based on the Type I PCMI stress transients reported by Brochard, et al. [53]. Consequently, the cumulative DHC extension depends on the number of transient stress cycles, the time period within which $K > K_{IH}$, the cladding temperature, and the cooling rate. The time, t_h, required for the diffusion of hydrogen to form hydrides at a crack tip can be estimated from the expression

$$t_h = \frac{l_h^2}{4D_h} \tag{19}$$

with

$$D_h(m^2/s) = 2.17x10^{-1} \exp\left(-\frac{8380}{RT}\right) \tag{20}$$

where l_h is the distance that hydrogen must diffuse to reach the crack tip to form hydrides, R is the universal gas constant (R = 8.31 J/mol/K), T is absolute temperature (K), and D_h is the diffusion coefficient of hydrogen in zirconium [4, 98]. Using Eqs. (19) and (20), the times required for diffusion distances of 20, 100, and 1,000 μm [0.79, 3.94, and 39.37 mil] are computed, and the results are shown as a function of temperature in Figure 26. For all three diffusion distances, the times for diffusion of hydrogen to the crack tip are small compared to the stress transient in power ramp, which is on the order of 10 minutes or higher. Thus, there are sufficient times for the diffusion of hydrogen to the crack tip to form hydrides.

The high transient stresses associated with power ramps can potentially cause hydride reorientation (see Figure 22), and leading to crack initiation in cladding by fracturing a hydride blister and a number of radial hydrides. Once a crack of sufficient depth is formed, the stress due to the internal gas pressure might then be large enough to cause subsequent DHC growth. If not, DHC growth would cease and remain dormant until the crack is reactivated by a subsequent transient stress cycle. At 318.5 ºC [605.3 ºF], the time to leakage, and future DHC are 24 and 198 minutes, respectively.

They are in accordance with the experimental observation (9–149 minutes) reported as power ramp test of segmental rods [36].

6. Discussion

6.1 DHC in zirconium alloy cladding tubes

Extensive review of literature data [2,10,11] and FEM computations [53–59] indicate that DHC in zirconium alloy cladding requires local transient stresses induced by PCMI during power ramping. Without these transient PCMI stresses, the cladding stresses due to internal gas pressure alone are not sufficiently high to produce a stress intensity factor at a manufacturing defect or crack to exceed the growth threshold, K_{IH}, for DHC. The relatively large PCMI stresses can cause hydride reorientation, leading to a variety of hydrid microstructures that are prone to brittle crack formation, followed by DHC. The frequency of PCMI occurrence during power ramps is not known, and the corresponding hydride microstructures have not been fully characterized. Thus, characterization of hydride morphology in the cladding tubes of high burnup fuel rods would indicate the frequency of the PCMI occurrence.

At least two types of transient stress profiles have been identified. Type I transient leads to continuous DHC growth until cladding failure, while Type II transient results in intermittent DHC growth and arrest. High burnup fuel rods, which may experience numerous power ramps, are likely to contain cracks that have been initiated by oxide cracking, blister fracture or corrosion, and subsequently extended by DHC.

A range of crack depths generated by DHC may be expected because the driving stresses are transient and vary with thermal and mechanical loading histories, hold times, and the number of power ramps. Currently, very little information is available about the hydride size distribution and the crack depth distribution in cladding tubes after they are removed from service. Without an accurate assessment of crack depth and hydride blister size, there are uncertainties on the cladding stress required to cause $K > K_{IH}$, the cladding resistance against DHC growth during the operation period before disposal.

The peak cladding temperature history for the center rod in the waste package during the operation period before disposal is about 325 °C [617 °F] [49]. Because of the high DHC propagation rate near 318 °C [604 °F], the time to leakage is on the order of a few hours if $K > K_{IH}$ in any cladding tubes. DHC may occur based on internal gas pressure alone if large hydride blisters or radial hydrides are present in the microstructure, the fracturing of which leads to $K > K_{IH}$. There is also a concern that slow cooling rates (10^{-6} to 10^{-7} °C/s) may reduce the K_{IH} value by forming a long continuous hydride at the crack tip. Experimental K_{IH} data needed to address this issue currently do not exist.

6.2 Effects of temperature on DHC

The cladding temperature has a significant effect on DHC growth in zirconium cladding tubes. The worst DHC growth resistance in Zr-2.5% occurs at around 310–320 °C [590–608 °F], with an estimated time to leakage of 24 minutes and an estimated time to failure of about 3.3 hours. For both cladding leakage or fracture, the

time to failure increases with increasing temperature above 310–320 °C [590–608 °F] because of slower hydride formation kinetics, while the time to failure increases with decreasing temperatures below 310–320 °C [590–608 °F] because of slower hydrogen diffusion. As a result, power ramping at around 310–320 °C [590–608 °F] can cause cladding failure by DHC in as little as 24 minutes for leakage or 3.3 hours for cladding fracture. Power ramping above 350 °C [662 °F] would prevent DHC initially, but results in DHC when the cladding temperature cools slowly from 350 °C [662 °F] to lower temperatures while the transient stresses are still high. The time to leakage is about one-eighth of the time to fracture at a given temperature. The lower DHC growth resistance at 310–320 °C [590–608 °F] occurs as a result of a high crack growth rate, despite a higher fracture toughness compared to that at lower temperatures. At ambient temperature, the DHC growth is exceedingly slow, making the time to propagate a DHC through a cladding wall thickness of 0.56 mm [22.1 mil] about 10 years. Thus, a low cladding temperature can effectively suppress DHC in cladding tubes, regardless of the local stresses at the ridges.

6.3 Effect of burnup

The burnup level of fuel rods is one of the most important factors affecting the cladding performance and integrity. A high burnup can be detrimental to cladding integrity because the number of power ramps increases with increasing burnup, while the gap between pellet and cladding decreases. In high burnup fuel, the cladding tubes are likely to have experienced a greater number of transient stress cycles where high PCMI

stresses can cause hydride reorientation, producing a variety of hydride microstructure and DHC growth compared to low burnup fuels. High burnup cladding tubes are also likely to contain thicker oxide or corrosion layers that can fracture during power ramping and serve as stress risers to initiate DHC at multiple sites. Power ramp tests conducted on segmented fuel rods [36] revealed a change of cladding failure from one of pinhole perforation at low burnup (<45 GWd/MTU) to one of RHA-DHC at high burnup levels (53 and 63 GWd/MTU).

6.4 Effect of cooling rate

The propensity of DHC decreases with increasing cooling rates. Because DHC growth rates are higher at temperatures between 200–350 °C [392–662 °F], a high cooling rate means less time is spent in this temperature range where the DHC propagates at high rates and consequently forms smaller crack extensions. A cooling rate exceeding 0.1 ºC/s [0.18 ºF/s] gives a crack extension of <0.01 mm [0.39 mil], because the time spent in the high DHC growth regime is only about 1 hour. The amount of DHC growth and time spent in the high DHC growth regime increase proportionately with decreasing cooling rates, as shown in Table 3. The slow cooling rates likely in a potential repository environment make the zirconium alloy cladding tubes susceptible to DHC growth, because there could be a significant amount of time spent at an elevated temperature where DHC growth kinetics are high.

7. Conclusions

1. PCMI (Section 4.2) during in-reactor power ramping can cause stress transients at local ridges in cladding. The magnitude and duration of stress transients that can cause hydride reorientation and DHC growth in cladding tubes can be classified into two types: Type I stress transients that result in $K > K_{IH}$ over a long time duration and cause DHC failure and Type II stress transients that result in $K > K_{IH}$ and DHC growth for only a short time duration and arrest DHC growth when K drops below K_{IH}.
2. High burnup cladding tubes are likely to contain crack sizes that are larger than those caused by manufacturing defects because of issues such as failure processes and the possibility of DHC during power ramps (Section 5). The crack sizes in cladding tubes are uncertain because the PCMI transient stresses during in-reactor power ramps and the corresponding DHC extensions are generally not well defined.
3. The growth threshold, K_{IH}, for DHC in zirconium alloys (Zr-2.5% Nb and Zircaloy-2) has a value of about 5 $MPa(m)^{1/2}$ [4.55 $ksi(in)^{1/2}$] or higher at ambient temperature (Section 2.1). A higher K_{IH} value can result from toughening due to the compressive stresses accompanied by hydride formation at the crack tip and crack bridging by intact ductile zirconium grains in the crack wake (Section 2.1). A K_{IH} lower than 5 $MPa(m)^{1/2}$ [4.55 $ksi(in)^{1/2}$] is also theoretically feasible when long hydrides form at the crack tip under very slow cooling rates, but this theoretical prediction has not been verified by experimental data. Although K_{IH} is

better described in terms of a probability distribution whose parameters vary with cooling rate, texture, temperature, and neutron fluence, a constant value of $K_{IH} = 5$ MPa$(m)^{1/2}$ [4.55 ksi$(in)^{1/2}$] can be used as a conservative criterion for the onset of DHC with a 95% confidence limit (Section 5.2).

4. The amount of DHC growth in zirconium alloy cladding tubes depends on the thermal mechanical history experienced (Section 5.2). Theoretical analysis indicates that cooling rate significantly affects DHC growth because it determines the times that hydride cracks spend at elevated temperatures where the growth rates are high. With decreasing cooling rates, the time to failure decreases, but the amount of DHC growth increases. The very slow cooling rates anticipated in a potential repository make cladding tubes susceptible to DHC unless the cladding temperature and the stress are kept low.

5. The growth threshold, K_{IH}, for DHC may be insensitive to the crack length because of a small crack limit that is about 20 μm [0.79 mil] or less (Section 2.1). Because the critical length for hydride fracture could be on the order of 10 μm [0.39 mil], a hydride crack behaves as a long crack almost as soon as it is initiated. Thus, it is not necessary to consider the effects of crack size on the K_{IH} value beyond that of a large crack in zirconium alloys when the applied stresses are less than 300 MPa [43.5 ksi] (Section 2.2).

6. Theoretically, DHC growth kinetics of zirconium alloys are the highest at the 300–320 °C [572–608 °F] temperature range. A theoretical analysis indicates that the DHC growth rate decreases with increasing temperatures above 320 °C [608 °F] and is suppressed at temperatures above 350 °C [662 °F] due to high

hydrogen solubilities (i.e., the possible absence of hydride formation at the crack tip). Furthermore, the crack growth rate decreases with decreasing temperatures below 300 °C [572 °F] because of slower hydrogen diffusion kinetics to the crack tip. Thus, according to the theoretical analysis, zirconium alloy cladding is most susceptible to DHC at temperatures ranging from 300 to 320 °C [572–608 °F]. Sustained loads at these temperatures should be avoided to minimize DHC.

7. The time to leakage is about one-eighth of the time to fracture for zircaloy alloy tubes (Zr-2.5% Nb and Zircaloy-2) at a given temperature between 0–350 °C [32–662 °F] (Section 2.2). The time to leakage is computed based on a crack depth reaching the cladding-computed wall thickness of 0.57 mm [22.4 mil], and the time to fracture is computed based on a critical stress intensity factor of 70 $MPa(m)^{1/2}$ [63.7 $ksi(in)^{1/2}$].

Recommendations

1. For in-reactor conditions, recommended tests and assessments are as follows:
    - Perform power ramp tests of segmented rods irradiated to different levels to confirm cladding failure by RHA-DHC at high burnup levels.
    - Evaluate the concept of a critical burnup level for cladding failure.
    - Assess the validity of the high PCMI stresses reported in the literature through numerical modeling or critical experimentation.
    - Characterize the hydride morphology to confirm the presence of high PCMI stresses that cause hydride reorientations and possible bonding between pellet and cladding on high burnup fuel rods.
2. Generate K_{IH} data for Zircaloy-4, ZIRLO, and M5 possibly for irradiated and hydrated samples, because there are few or no K_{IH} data for these alloys.
3. Investigate the dependence of K_{IH} on the hydride length. Formation of a long hydride at the crack tip may lower the K_{IH} value and lead to DHC at unexpectedly low stress levels by promoting the transition of time-dependent subcritical crack growth (DHC) to unstable fast fracture.

Acknowledgments—The author acknowledges G. Cragnolino for his technical review and B. Sagar for his programmatic review. Thanks are also expressed to L. Mulverhill for her editorial review and L. Naukam in preparing the document.

This paper was prepared to describe work performed by the Center for Nuclear Waste Regulatory Analyses (CNWRA) for the U.S. Nuclear Regulatory Commission (NRC) under Contract No. NRC–02–07–006. The activities reported here were performed on behalf of the NRC Office of Nuclear Material Safety and Safeguards, Division of High-Level Waste Repository Safety. This paper is an independent product of CNWRA and does not necessarily reflect the view or regulatory position of NRC.

References

[1] J.T.A. Roberts, Structural Materials in Nuclear Power Systems, Plenum Press, New York (1981) 60-61.

[2] S.L. Kwak, J.S. Lee, Y.J. Kim, Y.W. Park, A probabilistic integrity assessment of flaw in zirconium alloy pressure tube considering delayed hydride cracking, International Journal of Modern Physics B 17, Nos. 8 and 9 (2003) 1,587-1,593.

[3] R.P. Marshall, M.R. Louthan, Tensile properties of zircaloy with oriented hydrides, Transactions of ASM. 63 (1963) 693-700.

[4] D.O. Northwood, U. Kosasih, Hydrides and delayed hydrogen cracking in zirconium and its alloys, International Metals Reviews 28, No. 2. (1983) 92-121.

[5] R. Dutton, K. Nuttall, M.P. Puls, L.A. Simpson, Mechanisms of hydrogen induced delayed cracking in hydride forming materials, Metallurgical Transactions A 8A (1977) 1,553-1,562.

[6] B. Cox, Environmentally-induced cracking of zirconium alloys—a review, J. Nucl. Mater. 170 (1990) 1-23.

[7] S. Sagat, M.P. Puls, Temperature limit for delayed hydride cracking in Zr-2.5% alloys, transactions of the seventeenth international conference on structural mechanics in reactor technology (SMiRT 17), Prague, Czech Republic, August 17-22, 2003, Paper No. G06-4 (2003) 1-8.

[8] C.J. Simpson, C.E. Ellis, Delayed hydrogen embrittlement in Zr-2.5 wt% Nb alloys, J. Nucl. Mater. 52 (1974) 289-295.

[9] C.E. Coleman, J.F.R. Ambler, Susceptibility of zirconium alloys to delayed hydrogen cracking, zicronium in the nuclear industry: Third Conference, Quebec City, Canada, August 10-12, 1976, ASTM STP 633, A.L. Lowe and G.W. Parry (Eds.), ASTM International, Philadelphia, Pennsylvania (1977) 589-607.

[10] G.D. Moan, C.E. Coleman, E.G. Price, D.K. Rodgers, S. Sagat, Leak-before-break in the pressure tubes of CANDU reactors, International Journal of Pressure Vessels and Piping 43 (1990) 1-21.

[11] Y.W. Park, S.S. Kang, B.S. Han, Structural integrity assessment of pressure tubes for Wolsong Unit 1 based on operational experiences, Nuclear Engineering and Design. 212 (2002) 41-48.

[12] L.A. Simpson, M.P. Puls, The effects of stress temperatures and hydrogen content on hydride-induced crack growth in Zr-2.5 Pct Nb, Metallurgical Transactions A 10A (1979) 1,093-1,105.

[13] S.Q. Shi, M.P. Puls, Criteria for fracture initiation at hydrides in zirconium alloys-I. sharp crack tip, J. Nucl. Mater. 208 (1994) 232-242.

[14] S.Q. Shi, M.P. Puls, S. Sagat, Criteria for fracture initiation at hydrides in zirconium alloys-II. shallow notch, J. Nucl. Mater. 208 (1994) 243-250.

[15] International Atomic Energy Agency, Delayed Hydride Cracking in Zirconium Alloys in Pressure Tube Nuclear Reactors, Final Report of a Coordinated Research Project, 1998–2000. IAEA-TECDOC-1410 (2004).

[16] K. Edsinger, J.H. Davies, R.B. Adamson, Degraded fuel cladding fractography and fracture behavior, Zirconium in the Nuclear Industry: Twelfth International Symposium, ASTM STP 1354, G.P.Sabol and G.D. Moan (Eds.), ASTM International, West Conshohocken, Pennsylvania (2000) 316-339.

[17] K. Edsinger, K. Linga Murty, LWR pellet-cladding interactions: materials solutions to SCC, JOM. 53, No. 7 (2001) 9-13.

[18] International Atomic Energy Agency, Fuel failure in water reactors: causes and mitigation, Proceedings of a Technical Meeting held in Bratislava, Slovakia, June 17-21, 2002, IAEA-TECDOC-1345 (2003).

[19] J.S. Armijo, Performance of failed fuel, Proceedings of 1994 International Topical Meeting on LWR Fuel Performace, April 1994, American Nuclear Society, West Palm Beach, Florida (1994) 410-422.

[20] K-F Lin, C-S Chubg, J-J Yeh, J-H Chen, S-S Chu, L-F Lin, Investigation on the Post-defect deterioration of nonbarrier BWR failed rods, Proceedings of 1994 International Topical Meeting on LWR Fuel Performance, April 1994, American Nuclear Society, West Palm Beach, Florida (1994) 377-390.

[21] B. Cheng, B.C. Oberlander, W. Wiesenack, S. Yagnik, J. Turnbull, An in-reactor simulation test to evaluate root cause of secondary degradation of defective BWR fuel rod, Zirconium in the Nuclear Industry: Thirteenth International Symposium, ASTM STP 1423, G.D. Moan and P. Rudling (Eds.), ASTM International, West Conshohocken, Pennsylvania (2002) 616-633.

[22] G. Lysell, V. Grigoriev, Characteristics of axial splits in failed BWR fuel rods, Ninth International Symposium on Environmental Degradation of Materials in Nuclear Power Systems–Water Reactors, Newport Beach, California, August 1-9, 1999. F.P. Ford, S.M. Bruemmer, and G.S. Was (Eds.) The Minerals, Metals & Materials Society, Warrendale, Pennsylvania, (1999) 1,169.

[23] Y.S. Kim, PWR fuel failure analysis due to hydriding based on pie data. Fuel Failure in Water Reactors: Causes and Mitigation, Proceedings of a Technical Meeting held in Bratislava, Slovakia, June 17-21, 2002, IAEA-TECDOC-1345 (2003) 137-147.

[24] P. Rudling, T. Ingemansson, G. Wikmark, Operation and fuel design strategies to minimize degradation of failed BWR fuel, fuel failure in water reactors: causes and mitigation, Proceedings of a Technical Meeting held in Bratislava, Slovakia, June 17-21, 2002, IAEA-TECDOC-1345 (2003) 239-254.

[25] H.M. Chung, Understanding hydride- and hydrogen-related processes in high-burnup cladding in spent-fuel-storage and accident situations. International Meeting on LWR Fuel Performance, Orlando, Florida, September 19-22, 2004, Paper No. 1064 (2004).

[26] R.L. Yang, Resolving our understanding of REP-Na1 Microstructural Analysis, Proceedings of the 2004 International Meeting on LWR Fuel Performance, Orlando, Florida, September 19-22, 2004, Paper No. 1094 (2004) 565-575.

[27] CRWMS M&O, Hydride-related degradation of SNF cladding under repository conditions, ANL–EBS–MD–000011. Rev. 00 ICN 01. CRWMS M&O, Las Vegas, Nevada (2000).

[28] P. Guedeney, M. Trotabas, M. Boschiero, C. Forat, P. Blanpain, FRAGEMA fuel rod behaviour characterization at high burnup, Proceedings of the International Topical Meeting on LWR Fuel Performance, Fuel for the 90's, April 21-24, 1991, TIC: 243519, Avignon-France, La Grange Park, Illinois (1991) 627-638.

[29] A.M. Garde, G.P. Smith, R.C. Pirek, Effects of hydride precipitate localization and neutron fluence on the ductility of irradiated Zircaloy-4, Zirconium in the Nuclear Industry: Eleventh International Symposium, TIC: 244499, E.R. Bradley and G.P. Sabol (Eds.), ASTM International, Philadelphia, Pennsylvania (1996) 407-430.

[30] F. Lemoine, C.E. Cadarache, M. Balourdet, RIA related analytical studies and separate effect tests, Proceedings of the 1997 International Topical Meeting on Light Water Reactor Fuel Performance, Portland, Oregon, March 2-6, 1997, TIC 232556, American Nuclear Society, La Grange Park, Illinois (1997) 693-703.

[31] J. Papin, M. Balourdet, F. Lemoine, F. Lamare, J.M. Frizonnet, F. Schmitz, French studies on high burnup fuel transient behavior under RAI conditions, J. Nuclear Safety, 37(4) (1996) 289-327.

[32] R.O. Meyer, R.K. McCardell, H.M. Chung, D.J. Diamond, H.H. Scott, A regulatory assessment of test data for reactivity-initiated accidents, J. Nuclear Safety, 37(4) (1996) 271-288.

[33] G.P. Smith, Jr., R.C. Pirek, H.R. Freeburn, D. Schrire, The evaluation and demonstration of methods for improved nuclear fuel utilization, DOE/ET/34013-15, Washington, D.C. (1994).

[34] R.L. Yang, O. Ozer, H.H. Klepfer, Fuel performance evaluation for EPRI program planning, International Topical Meeting on LWR Fuel Performance, Avignon (France), April 21-24, 1991, Vol. 1, American Nuclear Society, La Grange Park, Illinois (1991) 258-271.

[35] O.N. Pierron, D.A. Koss, A.T. Motta, K.S. Chan, The influence of hydride blisters on the fracture of Zircaloy-4, J. Nuclear Materials. 322 (2003) 21-35.

[36] H. Hayashi, Y. Etoh, Y. Tsukuda, Outside-in failure of BWR segment rods during power ramp tests, Fuel Failure in Water Reactors: Causes and mitigation, Proceedings of a Technical Meeting held in Bratislava, Slovakia, June 17-21, 2002, IAEA-TECDOC-1345 (2003) 148-163.

[37] J.S. Mills, F.H. Huang, Delayed hydride cracking behavior for zircaloy-2 plate, Engineering Fracture Mechanics 39, No. 2 (1991) 241-257.

[38] F.H. Huang, W.J. Mills, Delayed hydride cracking behavior for ZIRCALOY-2 tubing, Metallurgical Transactions A 22A (1991) 2,049-2,060.

[39] C.E. Coleman, Effect of texture on hydride reorientation and delayed hydrogen cracking in cold-worked Zr-2.5Nb, Zicronium in the Nuclear Industry: Fifth Conference, Boston, Massachusetts, 1982, ASTM STP 754, D.G. Franklin (Ed.) ASTM International, Philadelphia, Pennsylvania (1982) 393-411.

[40] Y.S. Kim, S.S. Kim, S.C. Kwon, K.S. Im, Y.M. Cheong, Anisotropic threshold stress intensity factor, K_{IH} and crack growth rate in delayed hydride cracking of Zr-2.5Nb pressure tubes, Metallurgical and Materials Transactions A 33A (2002) 919-925.

[41] S.Q. Shi, M.P. Puls, Dependence of the threshold stress intensity factor on hydrogen concentration during delayed hydride cracking in zirconium alloys, J. Nucl. Mater. 218 (1994) 30-36.

[42] J.-H. Huang, C-S. Ho, Subcritical crack growth behavior for hydrided Zircaloy-4 plate, Materials Chemistry and Physics, 47 (1997) 184-192.

[43] S. Sagat, C.E. Coleman, M. Griffiths, B.J.S. Wilkins, The effect of fluence and irradiation temperature on delayed hydride cracking in Zr-2.5Nb, Zicronium in the Nuclear Industry: Tenth International Symposium, Baltimore, Maryland, June 21-24, 1993, ASTM STP 1245, A.M Garde and E.R. Bradley (Eds.), ASTM International, Philadelphia, Pennsylvania (1994) 35-61.

[44] K. Petterson, K. Kese, P. Efsing, Studies on delayed hydride cracking of zircaloy cladding, Ninth International Symposium on Environmental Degradation of Materials in Nuclear Power Systems-Water Reactors, Newport Beach, California, August 1-9, 1999, F.P. Ford, S.M. Bruemmer, and G.S. Was (Eds.) The Minerals, Metals & Materials Society, Warrendale, Pennsylvania (1999).

[45] P. Efsing, K Pettersson, Delayed hydride cracking in irradiated Zircaloy cladding, Zirconium in the Nuclear Industry: Twelfth International Symposium, ASTM STP 1354, G.P.Sabol and G.D. Moan (Eds.), ASTM, International, West Conshohocken, Pennsylvania (2000) 340-355.

[46] V. Grigoriev, R. Jakobsson, Delayed hydrogen cracking velocity and J-integral measurement on irradiated BWR cladding, Journal of ASTM International, Vol. 2, No. 8, Paper ID JAI12434, (September 2005).

[47] V. Jain, G. Cragnolino, L. Howard, A review report on high burnup spent nuclear fuel–disposal issues, CNWRA 2004-08, U.S. Nuclear Regulatory Commission Contract NRC-02-02-012, San Antonio, Texas, Center for Nuclear Waste Regulatory Analyses (2004).

[48] CRWMS M&O, Initial cladding condition, ANL–EBS–MD–000048. Rev. 00 ICN 01. CRWMS M&O, Las Vegas, Nevada (2000).

[49] E. Siegmann, J.K. McCoy, R. Howard, Cladding evaluation in the Yucca Mountain repository performance assessment, R.W. Smith and D.W. Shoesmith, (Eds.), Sci. Basis Nucl. Waste Man. XXIII Symp. Proc. 608, Matls. Res. Soc. (2000) 3-9.

[50] CRWMS M&O, Clad degradation – summary and abstraction, ANL–WIS–MD–000007, Rev. 00 ICN 01, CRWMS M&O, Las Vegas, Nevada (2000).

[51] M.E. Cunningham, E.P. Simonen, R.T. Allemann, I.S. Levy, R.F. Hazelton, E.R. Gilbert, Control of degradation of spent LWR fuel during dry storage in an inert atmosphere, PNL–6364, Pacific Northwest Laboratory, Richland, Washington (1987).

[52] Y.S. Kim, Hydride reorientation and delayed hydride cracking of spent fuel rods in dry storage, Metallurgical and Materials Transactions A, 40A (2009) 2867-2875.

[53] J. Brochard, F. Bentejac, N. Hourdequin, Nonlinear Finite Element Studies of the Pellet-Cladding Mechanical Interaction in a PWR Fuel, Transactions of the Fourteenth International Conference on Structural Mechanics in Reactor Technology (SMiRT 14), Lyon, France, August 17-22, 1997, Paper CW/4 (1997) 271-278.

[54] J. Brochard, F. Bentejac, N. Hourdequin, S. Seror, C. Verdeau, O. Fandeur, S. Lansiart, P. Verpeaux, Modelling of pellet cladding interaction in PWR fuel, Transactions of the Sixteenth International Conference on Structural Mechanics in Reactor Technology (SMiRT 16), Washington, DC, August 2001, Paper No. 1,314 (2001), 1-8.

[55] S. Bourreau, S. Lansiart, P. Couffin, C. Verdeau, G.M. Decroix, Influence of the hold period on the fuel rod behaviour during a power ramp, IAEA-TECDOC-1179, Fuel Chemistry and Pellet-Clad Interaction Related to High Burnup Fuel, Miköping, Sweden (1998) 63-73.

[56] S. Bourreau, J. Brochard, F. Bentejac, P. Couffin, C. Verdeau, S. Lansiart, N. Cayet, M.C. Grandjean, F. Mermaz, P. Blanpain, Ramp testing of PWR fuel and multi-dimensional finite element modeling of PCMI, Proceedings of the 2000 International Topical Meeting on Light Water Reactor Fuel Performance, Park City, Utah, April 10-13, 2000, Published on CD-ROM, La Grange Park, Illinois, American Nuclear Society (2000).

[57] I. Schäffler, P. Geyer, P. Bouffioux, P. Delobello, Thermomechancial behavior and modeling between 350 °C and 400 °C of zircaloy-4 cladding tubes from an unirradiated state to high fluence (0 to 85×10^{24} nm^{-2}, E > 1MeV), J. of Engineering Materials and Technology 122 (2000) 169-176.

[58] M. Suzuki, H. Uetsuka, Development of fuel performance code FEMAXI-6 and analysis of mechanical loading on cladding during power ramp for high burnup fuel rod, Fuel Failure in Water Reactors: Causes and Mitigation, Proceedings of a Technical Meeting held in Bratislava, Slovakia, June 17-21, 2002. IAEA-TECDOC-1345 (2003) 217-238.

[59] V. Retel, F. Trivaudey, M.L. Boubakar, D. Perreux, P. Thevenin, Comparative effects of structural and material parameters variability on pellet-cladding interaction in a PWR fuel rod, Nuclear Engineering and Design 228 (2004) 35-46.

[60] M. Billaux, Modeling pellet-cladding mechanical interaction and application to BWR maneuvering, Proceedings of the 2004 International Meeting on LWR Fuel Performance, Orlando, Florida, September 19-22, 2004, Paper No. 1047 (2004) 576-584.

[61] T. Ahn, F. Gaskins, D. Pomerening, M. Bailey, Hydride effects in the cladding performance for the safe geological disposal of high-level waste, ASTM workshop on hydride Reorientation in Zircaloy Alloys, Costa Mesa, California, January 31–Feburary 1, 2007. ML063540231. NRC (2007).

[62] D. Broek, Elementary Engineering Fracture Mechanics, Sijthoff & Noordhoff, Alphen aan den Rijn, Netherlands (1978) 73-77.

[63] L.A. Simpson, C.D. Cann, Fracture toughness of zirconium hydride and its influence on the crack resistance of zirconium alloys, J. Nucl. Mater. 87 (1979) 303-316.

[64] S.Q. Shi, M.P. Puls, Fracture strength of hydride precipitates in Zr-2.5Nb alloys, J. Nucl. Mater. 275 (1999) 312-317.

[65] R.M. McMeeking, A.G. Evans, Mechanics of transformation-toughening in brittle materials, J. Am. Ceram. Soc. 65, No. 5 (1982) 242-246.

[66] Y.-M. Pan, K.S. Chan, D. Rhia, Development of performance criteria for high burnup cladding materials, SwRI IR&D Project 20-R9565, Southwest Research Institute, San Antonio, Texas (2006). Synopsis available at http:/www.swri.org/3pubs/IRD2007/synopses/209565.htm (accessed September 21, 2011).

[67] M.P. Puls, Effects of crack tip stress states and hydride-matrix interaction stresses on delayed hydride cracking, Metallurgical Transactions A 21A (1990) 2,905-2,917.

[68] K.S. Chan, Y.-D. Lee, D.L. Davidson, S.J. Hudak, Jr., A fracture mechanics approach to high cycle fretting fatigue based on the worst case fret concept part I-model development, International Journal of Fracture 112 (2001) 299-330.

[69] X.Q. Yuan, K. Tangri, Metallographic observations on the developing hydride morphology at the crack tip during hydrogen induced delayed cracking in a Zr-2.5 Nb alloy, J. Nucl. Mater. 105 (1982) 310-317.

[70] D. Yan, R.L. Eadie, The near threshold behaviour of delayed hydride cracking in Zr-2.5 wt% Nb, International Journal of Pressure Vessels and Piping 77 (2000) 167-177.

[71] G.K. Shek, M.T. Jovanovic, H. Seahra, Y. Ma, D. Li, R.L. Eadie, Hydride morphology and abriation formation during delayed hydride cracking in Zr-2.5% Nb, J. Nucl. Mater. 231 (1996) 221-230.

[72] L.O. Jernkvist, A model for predicting pellet-cladding interaction-induced fuel rod failure, Nuclear Engineering and Design 156 (1995) 393-399.

[73] C.E. Coleman, S. Sagat, K.F. Amouzouvi, Control of Microstructure to Increase the Tolerance of Zirconium Alloys to Hydride Cracking, AECL-9524, Atomic Energy of Canada Ltd, Chalk River, Ontario, Canada (1987).

[74] S.S. Kim, Y.S. Kim, I.-H. Kuk, The effect of texture variation on delayed hydride cracking behavior of Zr-2.5% Nb plate, J. Nucl. Mater. 273, No. 1 (1999) 52-59.

[75] S.S. Kim, S.C. Kwon, K.N. Choo, Y.M. Cheong, Y.S. Kim, Effects of texture on K_{IH} in the radial direction in Zr-2.5% Nb pressure tube materials, Key Engineering Materials 183-187 (2000) 845-850.

[76] P.H. Kreyns, W.F. Bourgeois, C.J. White, P.L. Charpentier, B.F. Kammenzind, D.G. Franklin, Embrittlement of Reactor Core Materials, Zirconium in the Nuclear Industry: Eleventh International Symposium, Garmisch-Partenkirchen, Germany, September 11-14, 1995, ASTM STP 1295, E.R. Bradley and G.P. Sabol (Eds.) ASTM, West Conshohocken, Pennsylvania (1996) 758-782.

[77] K.S. Chan, Y.-D. Lee, A fracture mechanics-based model for assessing the mechanical failure of nuclear fuel rods due to rock fall, Nuclear Engineering and Design 201 (2000) 209-226.

[78] G. Bertolino, G. Meyer, J.P. Ipiña, Mechanical properties degradation at room temperature in Zircaloy-4 by hydrogen brittleness, Mater Res. 5 (2002) 1-13.

[79] J. Bertsch and W. Hoffelner, Crack resistance curves determination of tube cladding material, J. Nucl. Mate. 352 (2006) 116-125.

[80] P.A. Raynaud, D.A. Koss, A.T. Motta, K.S. Chan, Fracture toughness of hydrided zircaloy-4 sheet under through-thickness crack growth conditions, Zirconium in the Nuclear Industry: Fifteenth International Symposium, June 24-28, 2007, Sunriver, Oregon, ASTM STP 1505, M. Limack and B. Kammenzind (Eds.), ASTM International, West Conshohocken, Pennsylvania (2007), J. of ASTM International, 5 (2008)1, paper ID #JAI101183.

[81] M. Bannister, H. Shercliff, G. Bao, F. Zok, M.F. Ashby, Toughening in brittle systems by ductile bridging ligaments, Acta Metallurgica et Materialia 40 (2002) 1,531-1,537.

[82] A.F. Bower, M. Ortiz, A three-dimensional analysis of crack trapping and bridging by tough particles, J. Mech. Phys. Solids. 39 (1991) 815-858.

[83] K.S. Chan, Fracture toughness of multiphase intermetallics, high-temperature ordered intermetallic alloys VI, Mater. Res. Soc. Symp. 364 (1994) 469-480.

[84] K.S. Chan, D.L. Davidson, Delineating ductile-phase toughening and brittle-phase embrittlement in Nb-based in-situ composites, J. Metallurgical and Materials Transactions A. 32A (2001) 2,717-2,727.

[85] J.-H. Huang, S.-P. Huang, Evidence of discontinuous crack growth in delayed hydride cracking of a zirconium alloy, J. Scripta Metall. 27 (1992) 1,247-1,251.

[86] A. McMinn, E. Darby, J.S.Schofield, The terminal solid solubility of hydrogen in zirconium alloys, Zirconium in the Nuclear Industry: Twelfth International Symposium, ASTM STP 1354, G.P.Sabol and G.D. Moan (Eds.), ASTM, International, West Conshohocken, Pennsylvania (2000) 173-195.

[87] J.S. Schofield, E.C. Darby, C.F. Gee, Temperature and hydrogen concentration limits for delayed hydride cracking in irradiated Zircaloy, Zirconium in the Nuclear Industry: Thirteenth International Symposium, ASTM STP 1423, G.D. Moan and P. Rudling (Eds.), ASTM, International, West Conshohocken, Pennsylvania (2002) 339-357.

[88] T.L. Sanders, K.D. Seager, Y.R. Rashid, P.R. Barrett, A.P. Malinauskas, R.E. Einziger, H. Jordan, T.A. Duffey, S.H. Sutherland, P.C. Reardon, A Method for Determining the Spent-Fuel Contribution to Transport Cask Containment Requirements, SAND90-2406. Sandia National Laboratories, Albuquerque, New Mexico (1992) TIC: 232162.

[89] A.M. Garde, Enhancement of aqueous corrosion of Zircaloy-4 due to hydride precipitation at the metal-oxide interface, C.M. Eucken and A.M. Garde (Eds.), Kobe, Japan (1991) 566-594.

[90] B.A. Cottom, M.J. Mayo, Fracture toughness of nanocrystalline ZrO_2 – 3mol% Y_2O_3 determined by vickers indentation, Scripta Materialia 34 No. 5 (1996) 809-814.

[91] B. Cox, Pellet-clad interaction (PCI) failures of zirconium alloys fuel cladding-a review, J. Nucl. Mater. 172 (1990) 249-292.

[92] C. Pescatore, M.G. Cowgill, T.M. Sullivan, Zircaloy cladding performance under spent fuel disposal conditions, BNL52235, Brookhaven National Laboratory, Upton, New York (1989).

[93] G.V. Ranjan, G.N. Brooks, A.K. Miller, Stresses and strains at zircaloy cladding ridges, Transactions of the Fifth International Conference on Structural Mechanics in Reactor Technology, Vol. D, Paper D3/3, T. Jaeger and B.A. Boley, (Eds.), International Congress Center, Berlin (1979).

[94] R.E. Einziger, C.L. Brown, G.P. Hornseth, C.G. Interrante, Data needs for storage and transportation of high burnup fuel, Radwaste Solutions, March/April (2005) 44-56.

[95] C. Ferry, C. Poinssot, Expected evolution of spent nuclear fuel in long term dry storage: consequences on the RN source-term models, Presentation at the CEA-NRC Meeting, February 7, 2005, Washington, DC , NRC ADAMS Accession Number ML112640422 (2005).

[96] H.C. Chu, S.K. Wu, and R.C. Kuo, Hydride reorientation in Zircaloy-4 cladding, Journal of Nuclear Materials, 373 (2008) 319-327.

[97] R.S. Daum, S. Majumdar, Y. Liu, M.C. Bilone, Radial-hydride embrittlement of high-burnup Zircaloy-4 fuel cladding, J. Nuclear Science and Technology, 43 (2006) 1,054-1,067.

[98] Kearns, J.J., Dissolution kinetics of hydride platelets in zircaloy-4, J. Nuclear Materials 27 (1968) 64-72.

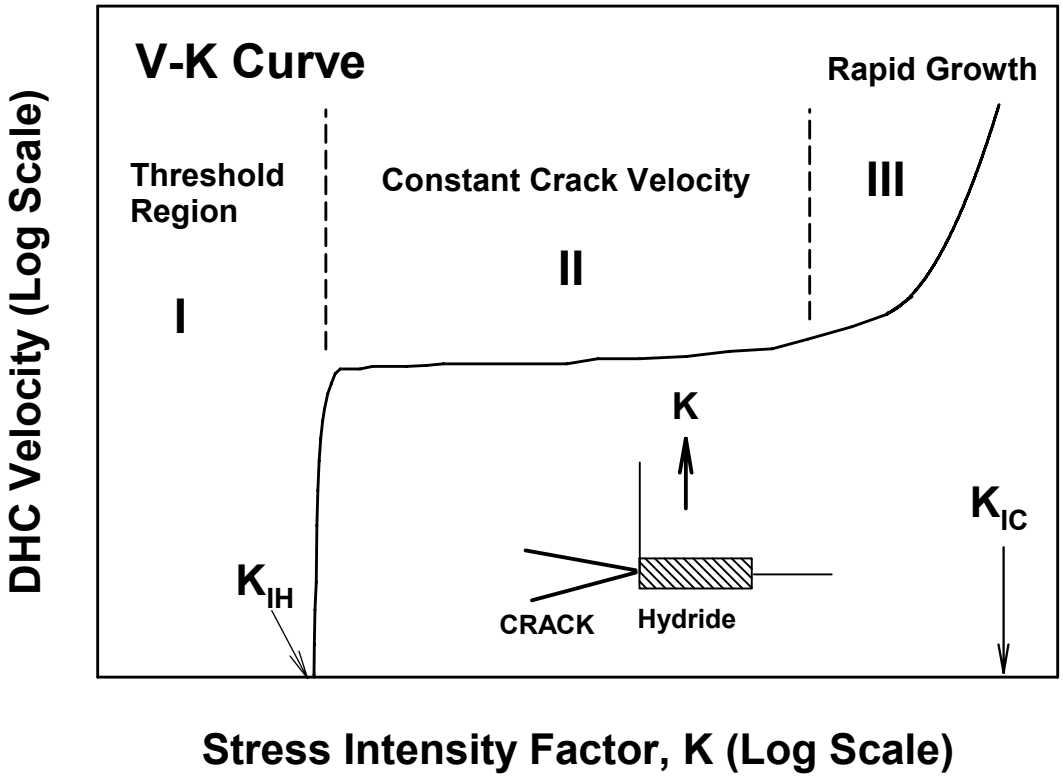

Figure 1. **DHC velocity as a function of the Mode I stress intensity factor, K, showing a growth threshold, K_{IH}, for the onset of DHC, a constant velocity region, and a fast fracture region.**

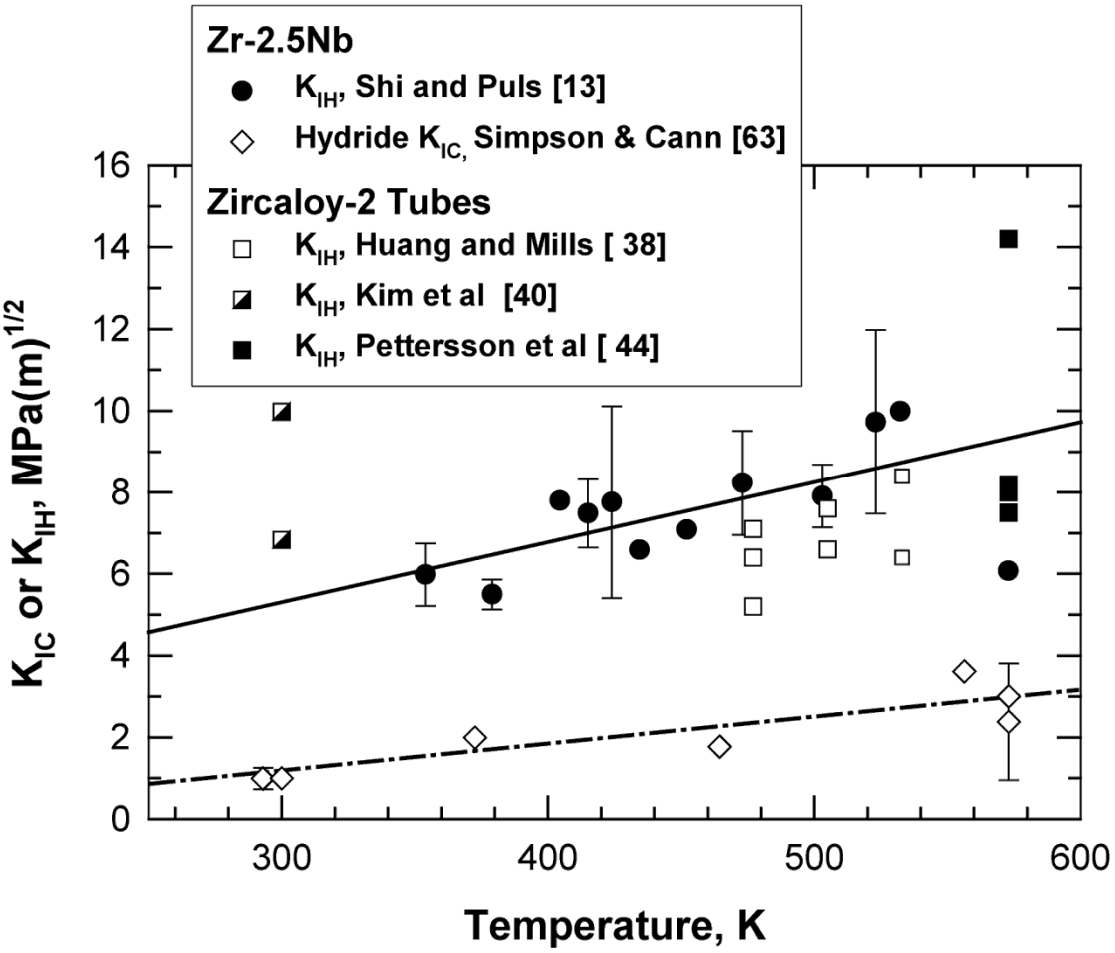

Figure 2. **The DHC growth threshold K_{IH} of Zr-2.5 Nb compared to the critical stress intensity factor, K_{IC}, for fracture of bulk hydrides. Experimental data are from Shi and Puls [13] and Simpson and Cann [63]. {1 MPa(m)$^{1/2}$ = 0.91 ksi(in)$^{1/2}$; T(°F) = 1.8[T(K) – 273] + 32}**

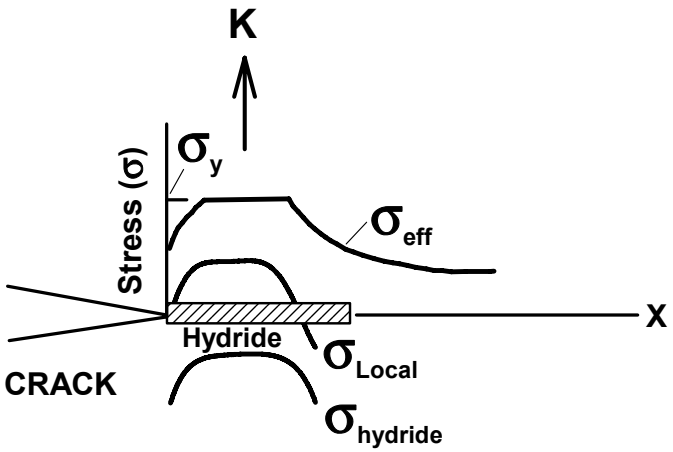

Figure 3(a). Schematic showing crack-tip hydride and stresses.

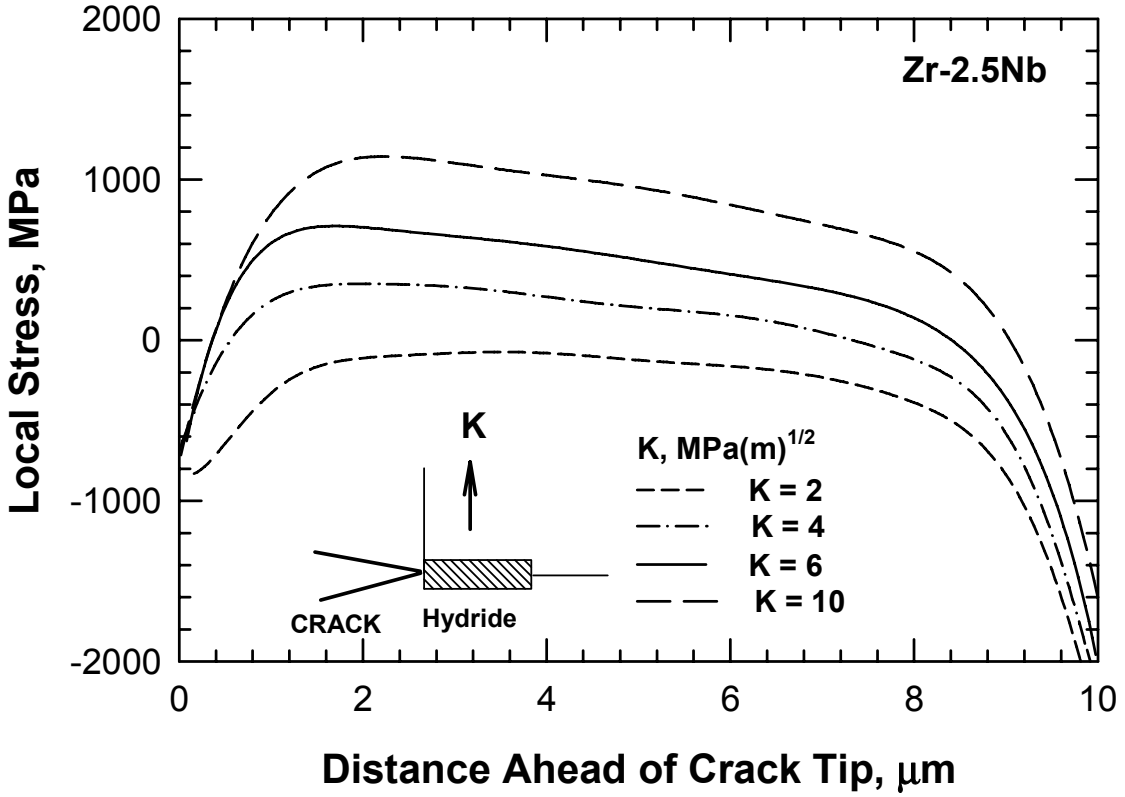

Figure 3(b). **Profiles of $\sigma_{local} = \sigma_{eff} + \sigma_{hydride}$ at crack tip for a hydride 2μm [7.87×10^{-2} mil] thick, 10μm [0.39 mil] long, and 10 μm [0.39 mil] wide under different K values. Results are from Shi and Puls [13]. [1 MPa = 0.145 ksi]**

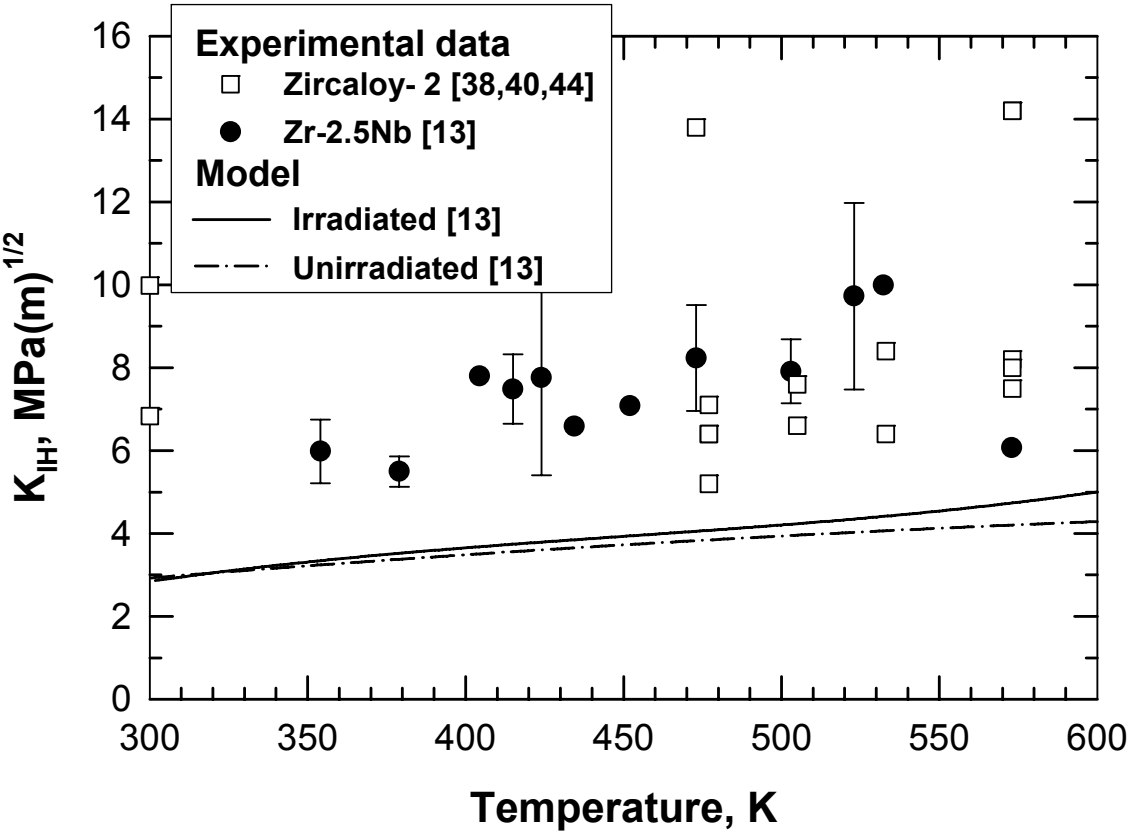

Figure 4. **Comparison of theoretical K_{IH} with experimental data. Data are from Shi and Puls [13]. [1 MPa(m)$^{1/2}$ = 0.91 ksi(in)$^{1/2}$]**

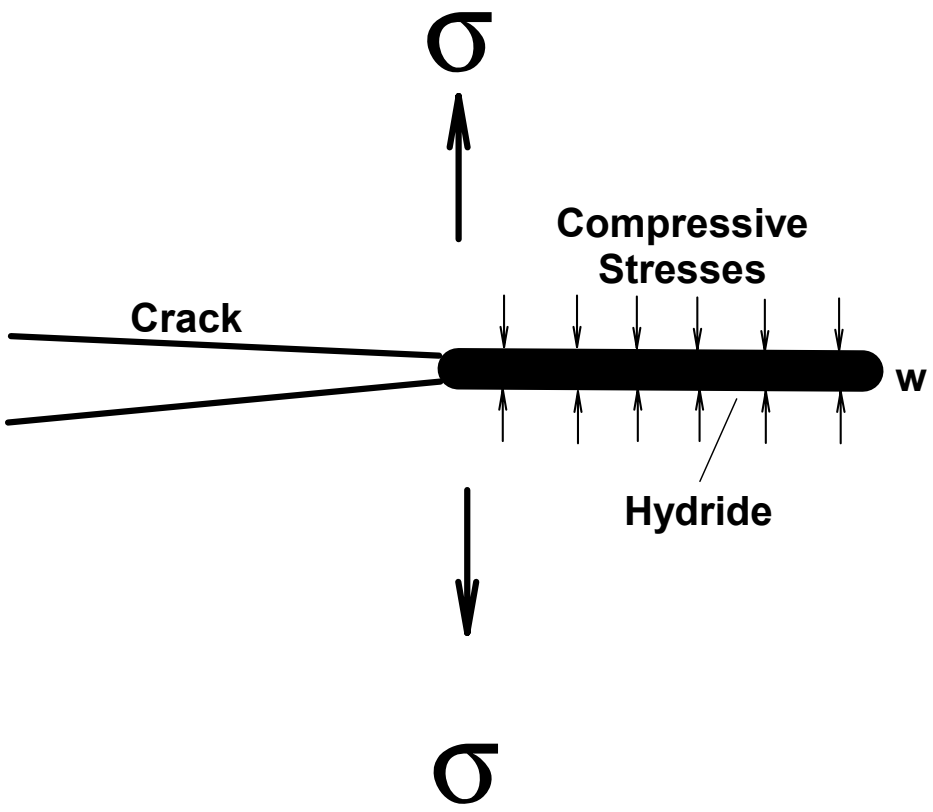

Figure 5. **Crack-tip shielding of a crack in an elastic field by the compressive transformation stresses accompanied by hydride formation at a crack tip.**

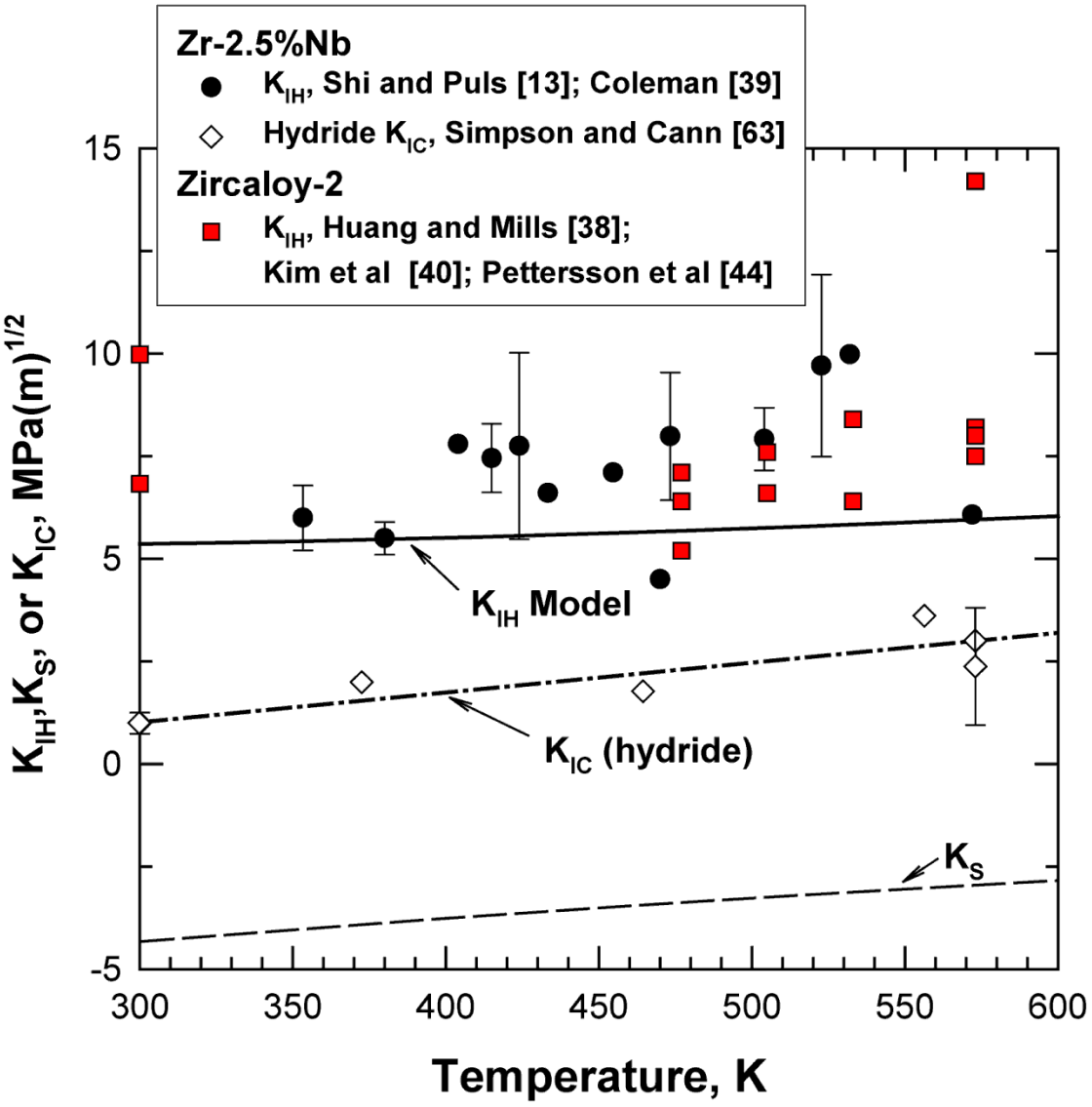

Figure 6. **Theoretical values of K_{IH} based on the fracture toughness (K_{IC}) of hydrides {data are from Simpson and Cann [63]} and crack-tip shielding of near-tip stress intensity factor (K_S) compared against experimental data of K_{IH} from the literature {data are from Coleman [39]; Shi and Puls [13]; Huang and Mills [38]; Pettersson, et al. [44]; Kim, et al. [40]}. {1 MPa(m)$^{1/2}$ = 0.91 ksi(in)$^{1/2}$; T(°F) = 1.8[T(K) – 273] + 32}**

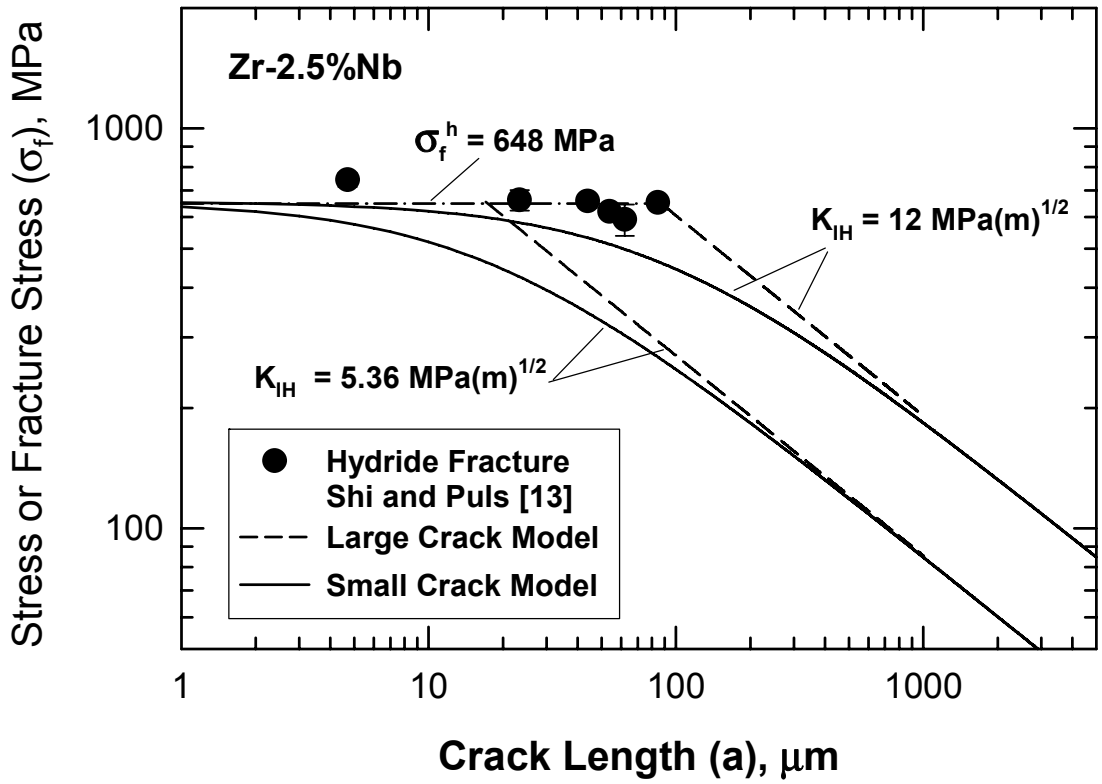

Figure 7. **Comparisons of large crack and small crack threshold stresses for delayed hydride cracking in Zr-2.5% Nb for K_{IH} values of 5.38 MPa $\sqrt{m}$ [4.9 ksi(in)$^{1/2}$] and 12 MPa $\sqrt{m}$ [10.9 ksi(in)$^{1/2}$]. The threshold stresses for DHC approach the hydride fracture stress, which is 648 MPa [94 ksi] {data are from Shi and Puls [17]}, at various crack lengths, depending on the K_{IH} value. DHC growth occurs when the cladding stress exceeds the threshold stress at a given crack length. [1 MPa = 0.145 ksi; 1 MPa(m)$^{1/2}$ = 0.91 ksi(in)$^{1/2}$; 1 μm = 0.0394 mil]**

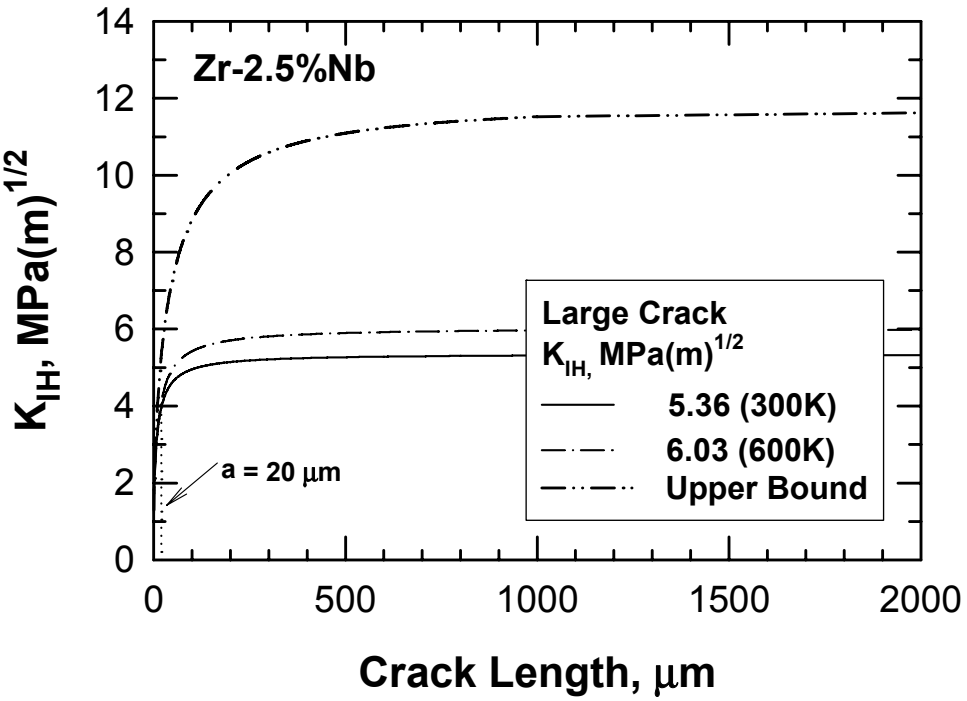

Figure 8. **Dependence of K_{IH} on crack length for small cracks. For a crack depth of 10–20 μm [0.39–0.99 mil], $K_{IH} \approx 3.3–4$ MPa(m)$^{1/2}$ [3–3.64 ksi(in)$^{1/2}$], but its value increases rapidly with the crack length to saturate at the large crack threshold. [1 MPa(m)$^{1/2}$ = 0.92 ksi(in)$^{1/2}$; 1 μm = 0.0394 mil; 300K = 80.6 ºF; 600K = 620.6 ºF]**

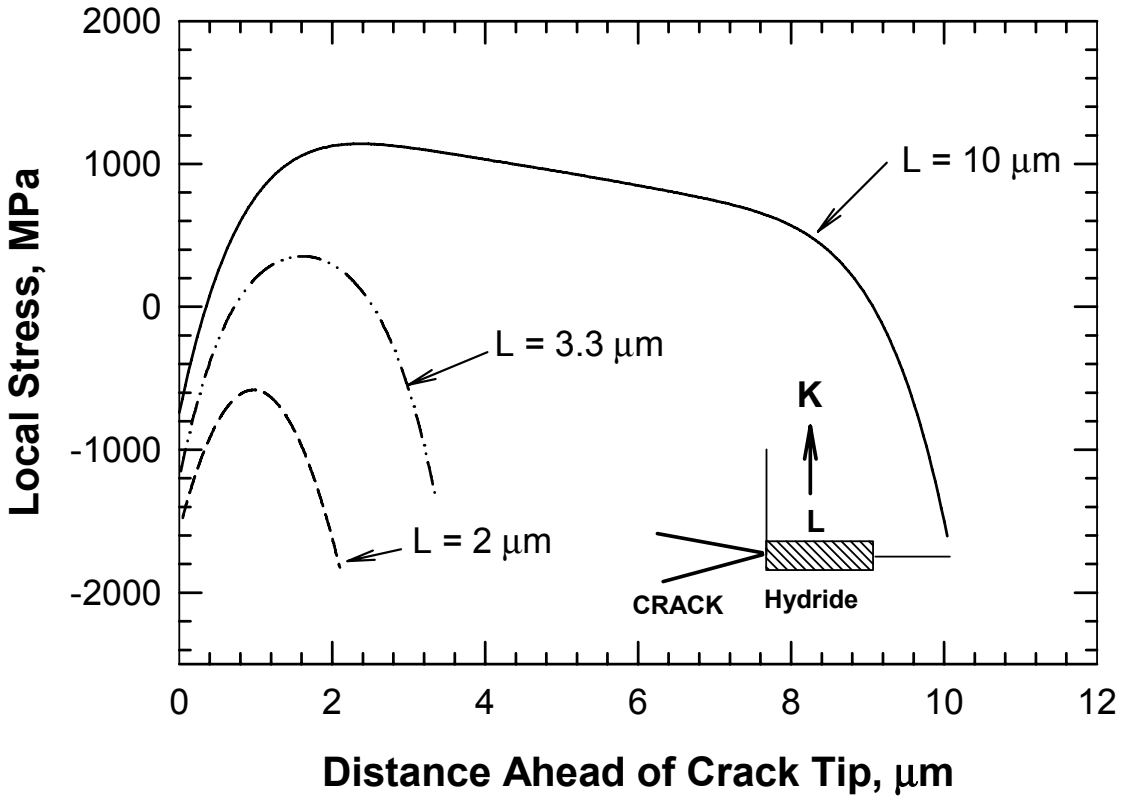

Figure 9. **Profiles of $\sigma_{local} = \sigma_{eff} + \sigma_{hydride}$ at crack tip for hydrides having different lengths under K = 10 MPa(m)$^{1/2}$ [9.1 ksi(in)$^{1/2}$]. Results are from Shi and Puls [13]. [1 MPa = 0.145 ksi; 1 μm = 0.0394 mil]**

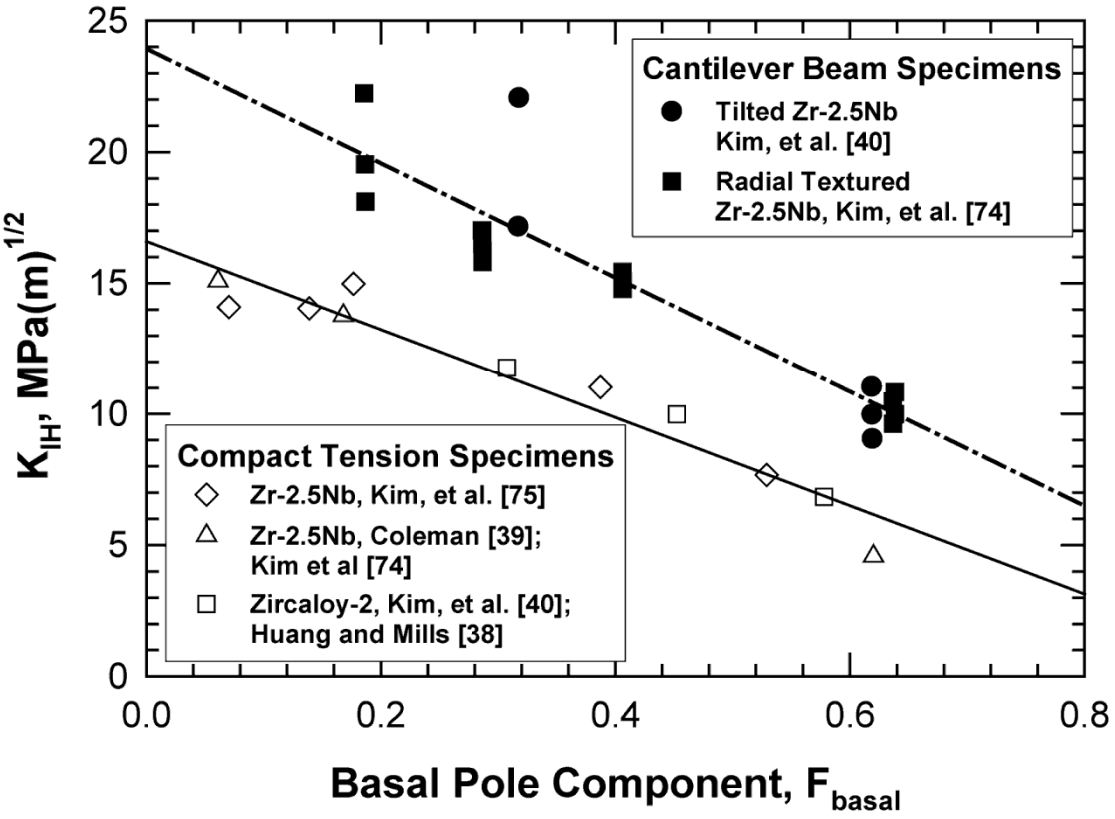

Figure 10. **Threshold stress intensity factor, K_{IH}, of Zr-2.5 Nb tube with crack growth direction as a function of the basal pole components. Data are compiled by Kim, et al. [40]. [1 MPa(m)$^{1/2}$ = 0.91 ksi(in)$^{1/2}$]**

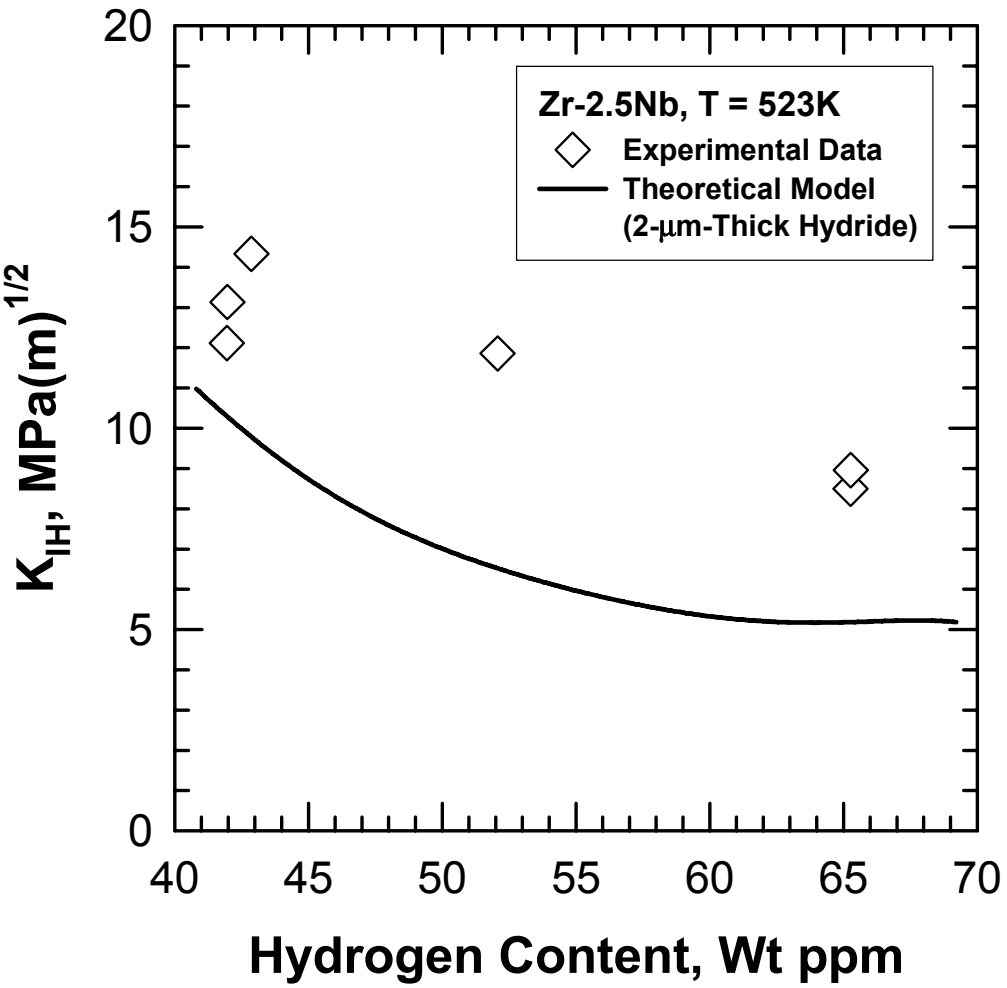

Figure 11. **The threshold stress intensity factor, K_{IH}, as a function of hydrogen concentration in solid solution. Experimental data and theoretical model are from Shi and Puls [41]. [1 MPa(m)$^{1/2}$ = 0.91 ksi(in)$^{1/2}$; 523 K = 482 ºF; 2 μm = 0.0787 mil]**

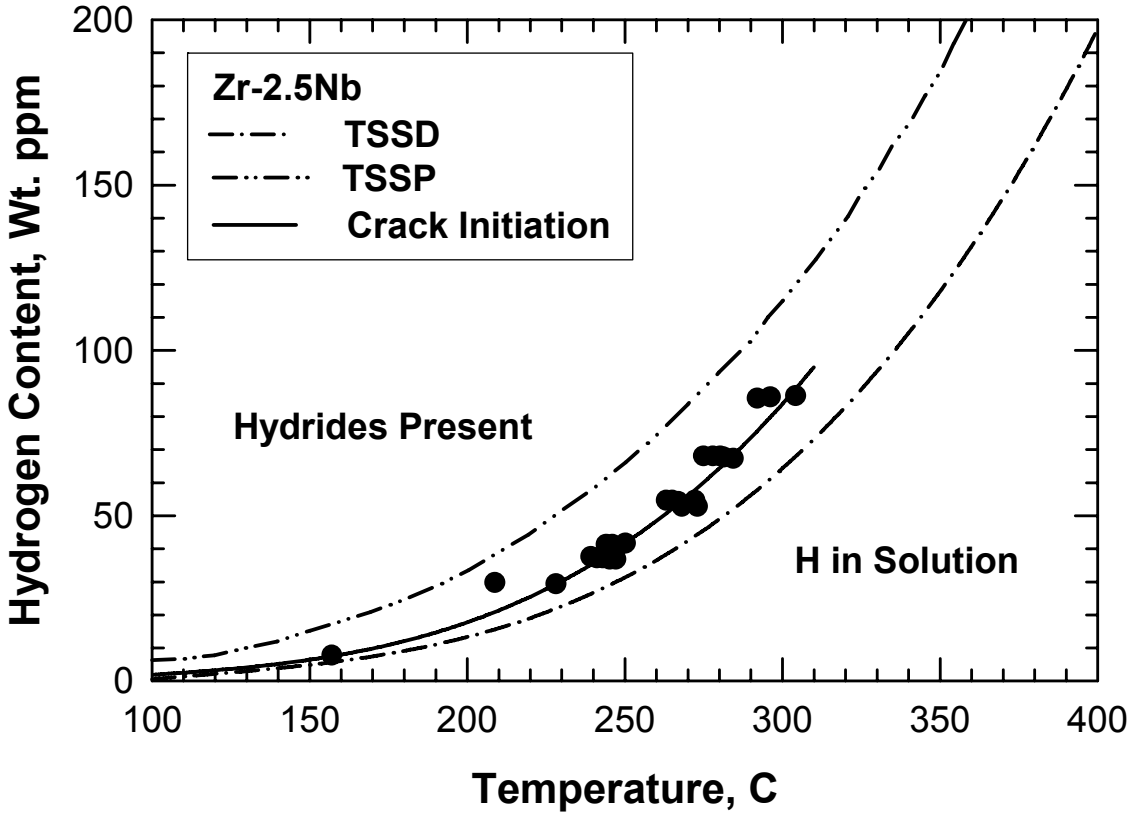

Figure 12. **Terminal solubility limits for zirconium: TSSD-hydride dissolution limit, TSSP-hydride precipitation limit, and crack initiation temperature. Results are from Sagat and Puls [7]. {T(°F) = 1.8[T(K) – 273] + 32}**

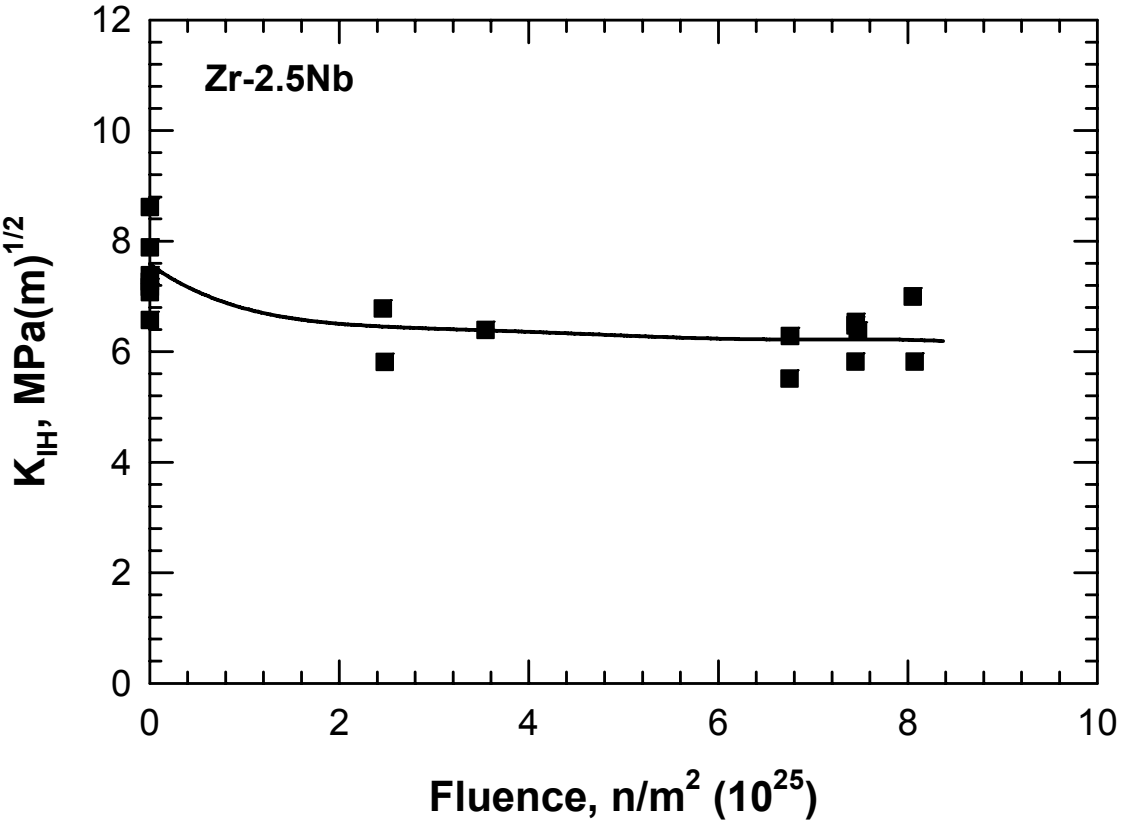

Figure 13. Dependence of K_{IH} on irradiation fluence. Data are from Sagat, et al. [43]. [1 MPa(m)$^{1/2}$ = 0.91 ksi(in)$^{1/2}$; 1 n/m^2 = 10.8 n/ft^2]

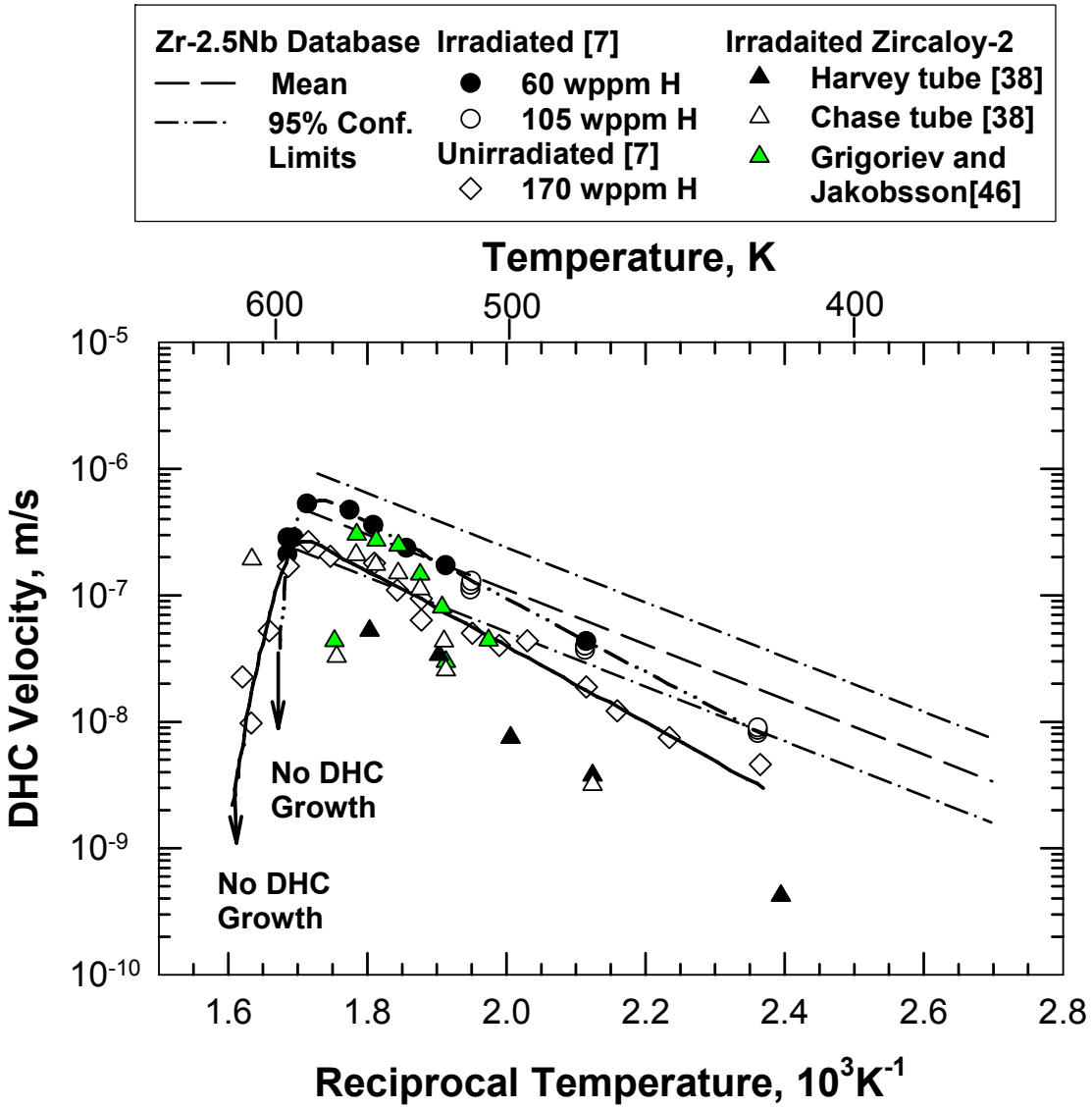

Figure 14. **High temperature crack velocity data for DHC in irradiated and unirradiated Zr-2.5% Nb material. Data are from Sagat and Puls [7]; Huang and Mills [38]; Grigoriev and Jakobsson [46]. {T(°F) = 1.8[T(K) – 273] + 32; 1 m/s = 3.28 ft/s}**

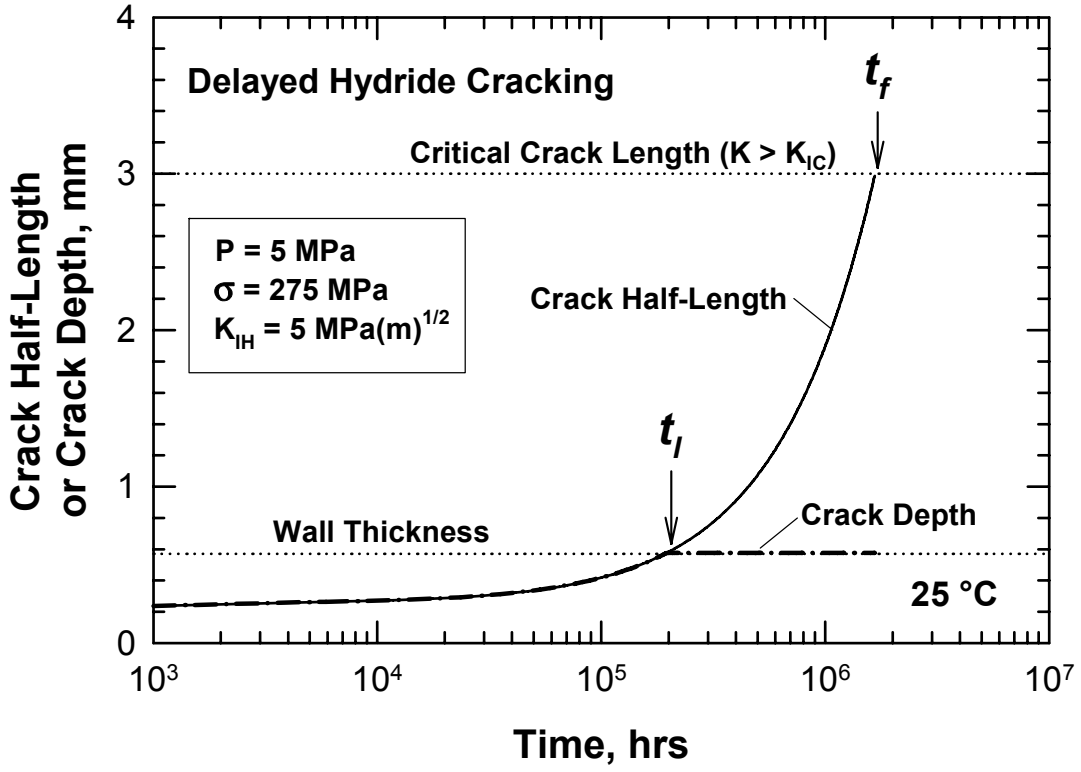

Figure 15. **Computed time to leakage based on crack depth equal cladding wall thickness compared against computed time to fracture based on the stress intensity factor exceeding a critical stress intensity factor of 70 MPa(m)$^{1/2}$ [63.7 ksi(in)$^{1/2}$]. [1 mm = 39.4 mil]**

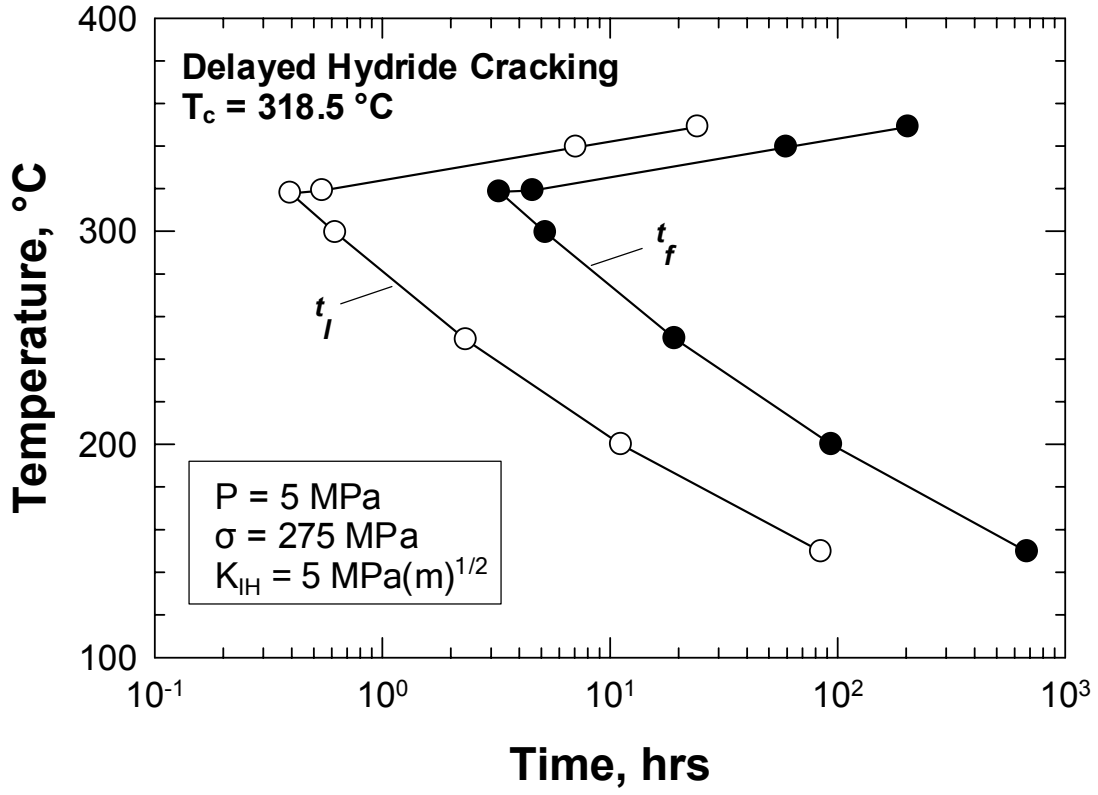

Figure 16. **Computed time to leakage (crack depth = wall thickness) and time to fracture K >K_{IC}) by DHC in Zr-2.5% Nb as a function of temperature. The results show the time to failure (leakage or fracture) decreases with increasing temperature from 0 to 320 °C [32 to 608 ºF] and increases from 320 to 350 °C [608 to 662 ºF]. No DHC failure occurs at temperatures above 350 °C [662 ºF] because of the absence of hydride formation at the crack tip. {T(ºF) = 1.8T(ºC) + 32; 1 MPa(m)$^{1/2}$ = 0.91 ksi(in)$^{1/2}$}.**

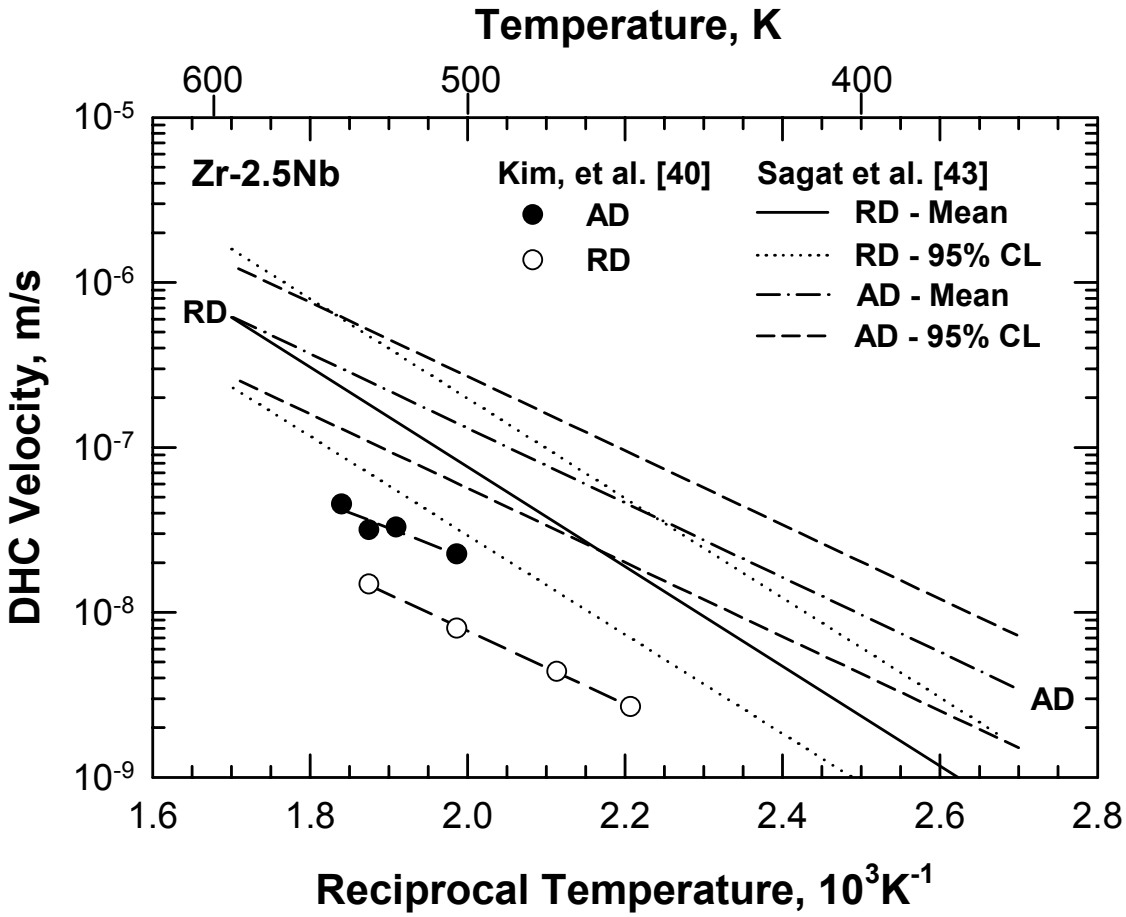

Figure 17. Comparison between radial and axial DHC velocity for Zr-2.5% Nb pressure tubes. Data are from Sagat, et al. [43] and Kim, et al. [40]. RD: radial direction; AD: axial direction; CL: confidence limits. 1 m/s = 3.28 ft/s; T(°F) = 1.8[T(K) – 273] + 32}

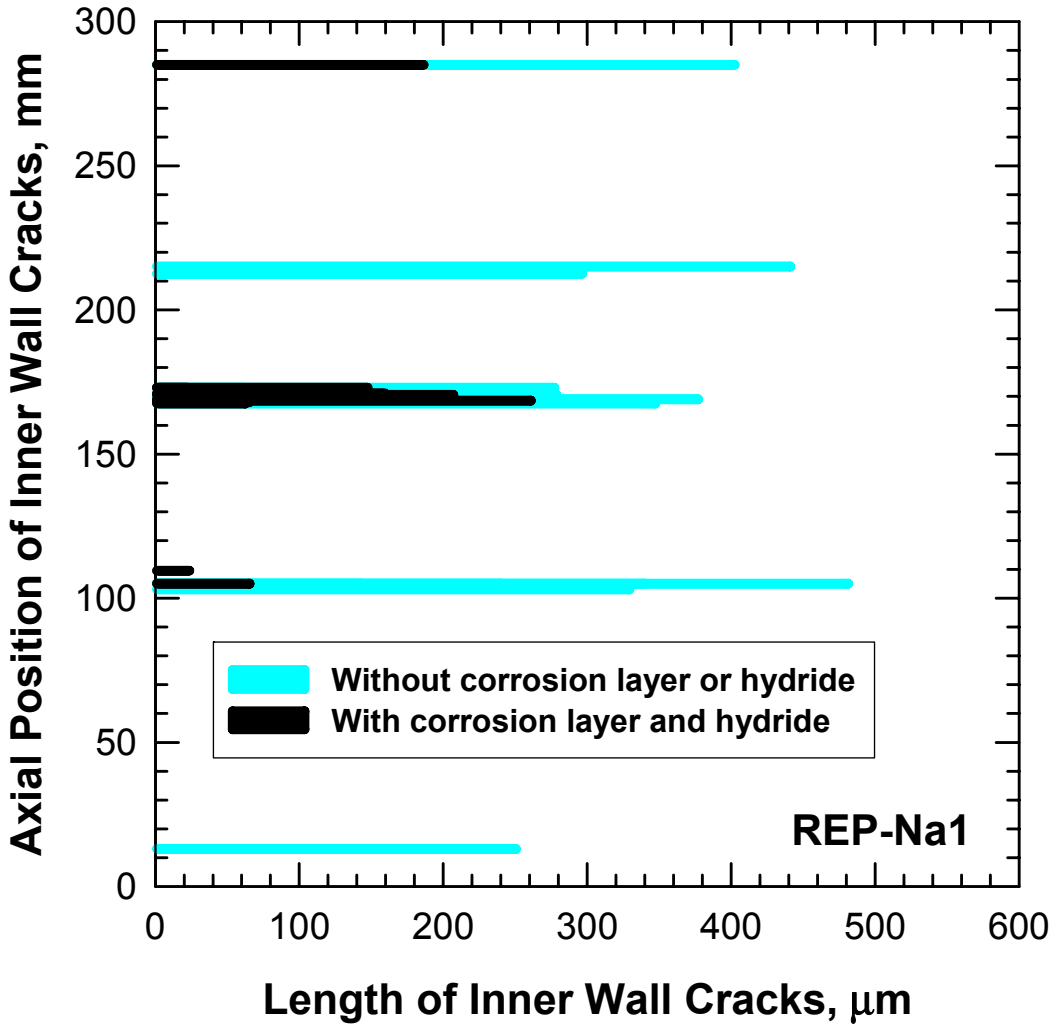

Figure 18. **Axial position versus length of inner wall cracks observed in REP-Nal. Data are from Chung [25]. [1 mm = 39.4 mil; 1 μm = 0.0394 mil]**

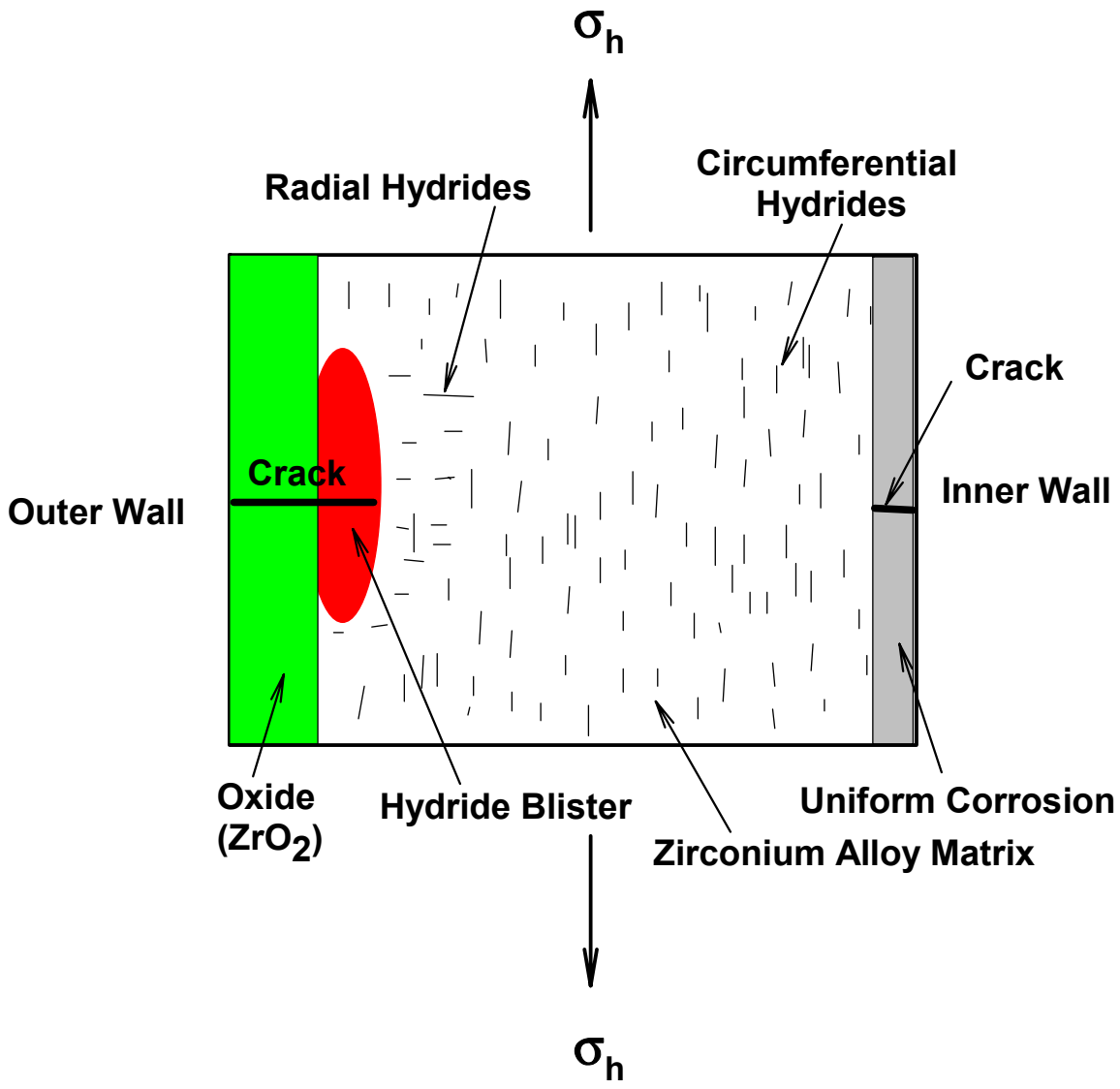

Figure 19. **Summary of possible failure mechanisms in high burnup Zr-based fuel cladding tubes showing (i) oxide formation and cracking on outer wall, (ii) hydride blister formation and cracking, (iii) hydride reorientation, and (iv) uniform corrosion on the inner wall. Once initiated, the outer wall and inner wall cracks can propagate by DHC if $K > K_{IH}$. Schematic corresponds to a cross section of the cladding perpendicular to the axial direction where σ_h denotes hoop stress.**

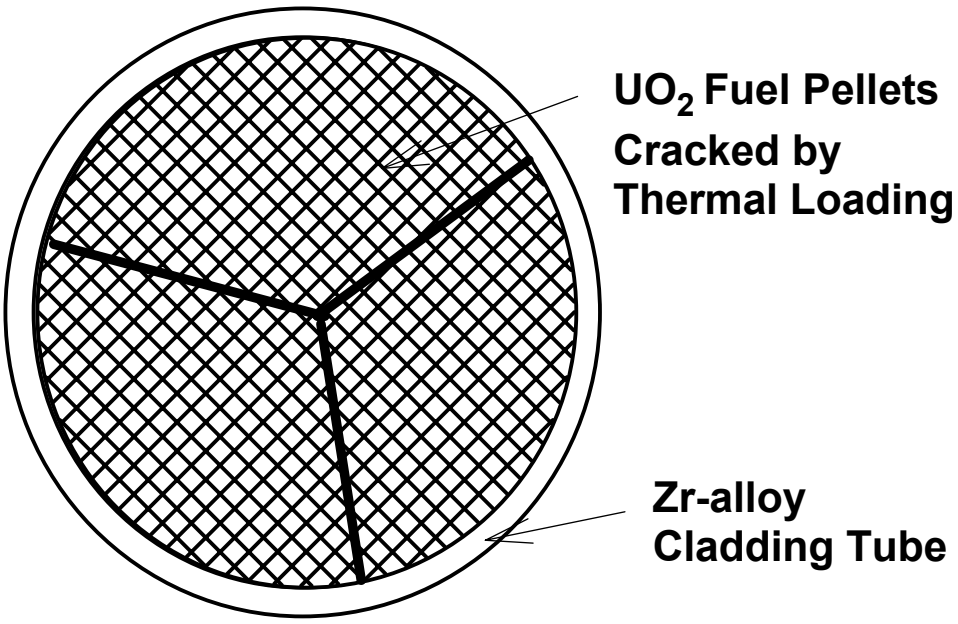

Figure 20. **Pellet-cladding mechanical interaction results from the thermal expansion and cracking of the UO_2 fuel pellets during power ramp and induces local tensile hoop stresses in the cladding that can potentially propagate an existing crack or defect by DHC.**

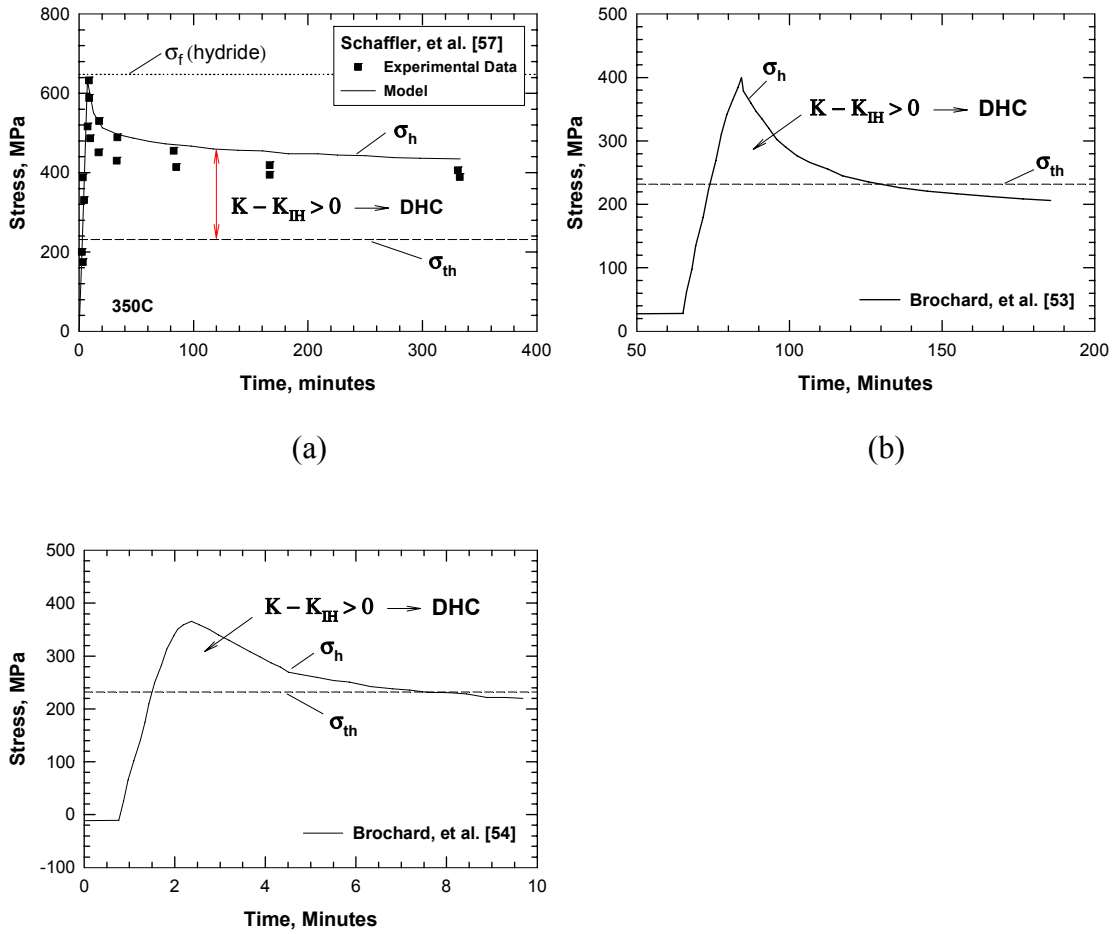

Figure 21. **Stress transients associated with pellet-cladding mechanical interactions: (a) Type I stress transient with a stabilized stress that leads to $K > K_{IH}$ and DHC, (b) Type II stress transient with a peak stress that leads to $K > K_{IH}$ and DHC over a short duration (130 minutes) and stabilized stress that results in $K < K_{IH}$ and crack arrest, and (c) Type II stress transient with a 7-minute duration where $K > K_{IH}$ and DHC growth can occur. [1 MPa = 0.145 ksi]**

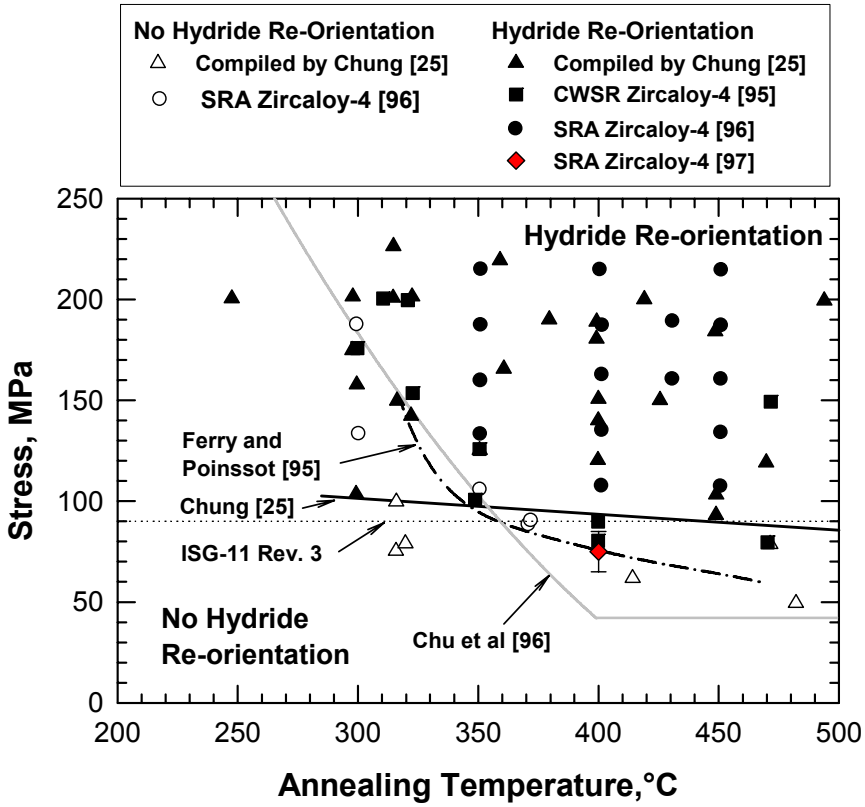

Figure 22: **Critical tensile stresses for hydride reorientation as a function of temperature compared against experimental data compiled by Chung [25], cold-worked and stress-relieved (CWSR) Zircaloy-4 data compiled by Ferry and Poinssot [95], and stress-relief annealed (SRA) Zircaloy-4 by Chu, et al. [96] and Daum, et al. [97]. The stress limit defined in the NRC Interim Staff Guidance-II Revision 3 (ISG-II Rev. 3) [94] is shown as the dotted line.**

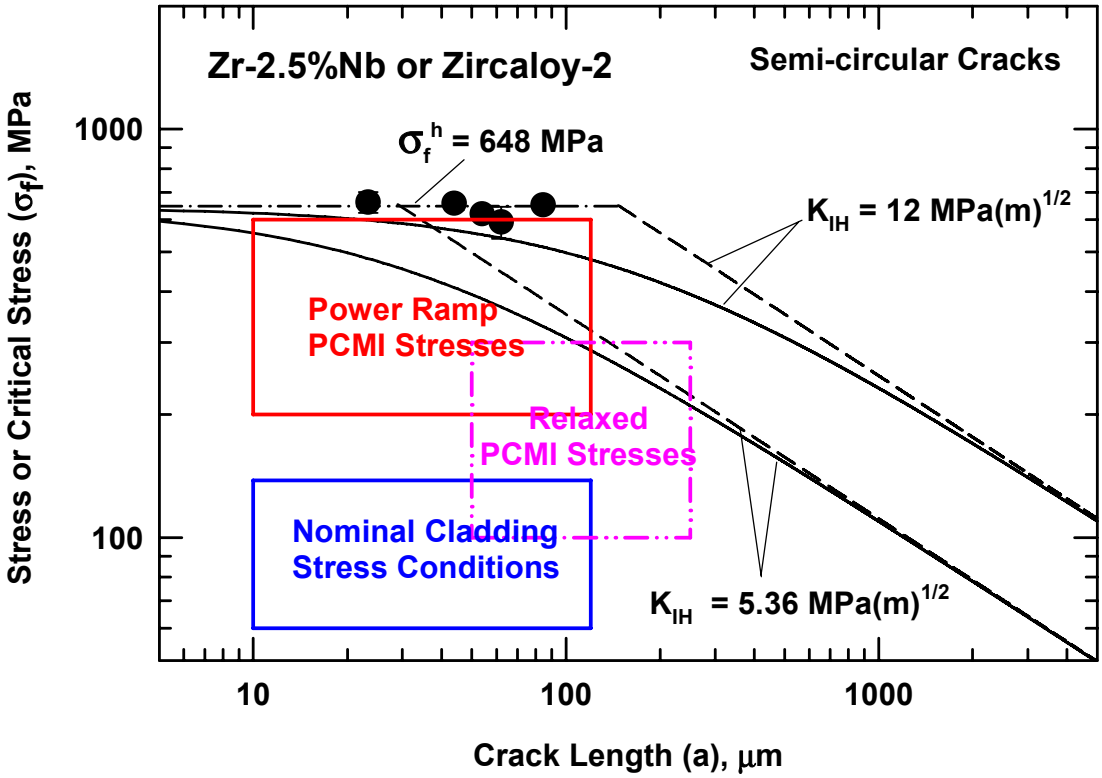

Figure 23. **A comparison of cladding stresses under various loading conditions and crack lengths against the large crack and small crack threshold stresses for the onset of DHC in Zr-alloy cladding tubes made of Zircaloy-2 or pressure tubes made of Zr-2.5% Nb.**
[1 MPa = 0.145 ksi; 1 MPa(m)$^{1/2}$ = 0.91 ksi(in)$^{1/2}$; 1 μm = 0.0394 mil]

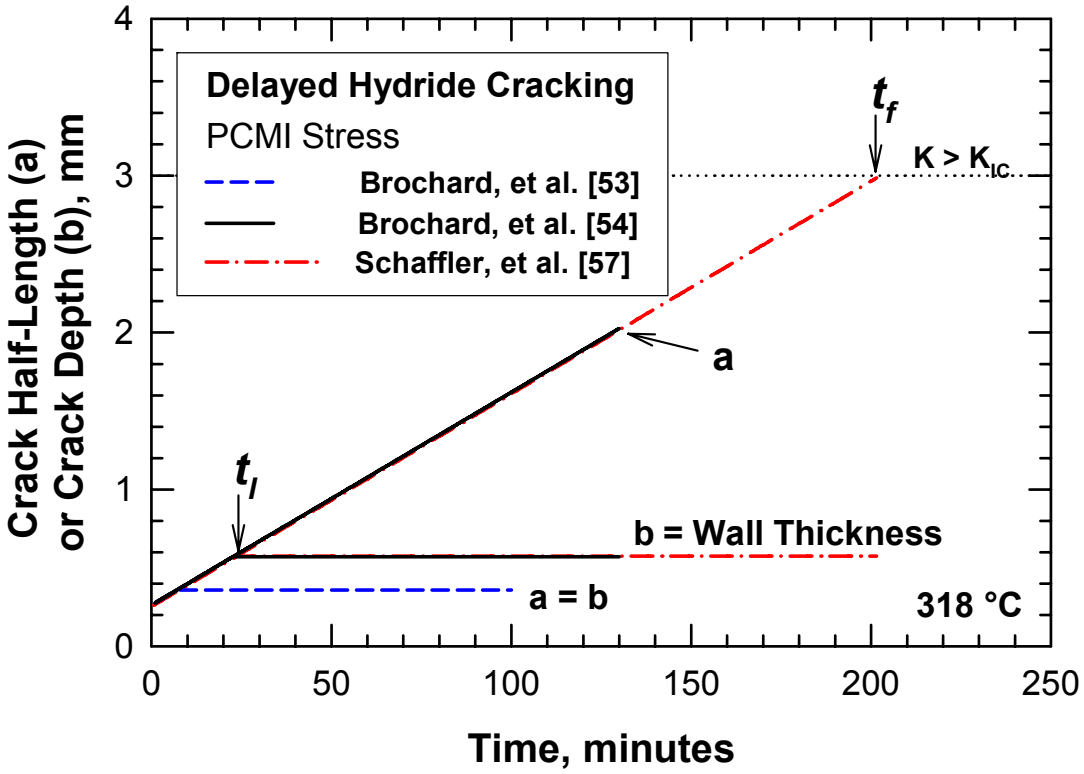

Figure 24. **DHC growth resulting from PCMI stress transients during power ramps. Crack extension was computed for Zr-2.5% Nb cladding on the basis of PCMI stress transients reported by Schäffler, et al. [7] and Brochard, et al. [53,54]. [1 mm = 39.4 mil; 318 ºC = 604.4 ºF]. Leakage occurs at t_I where the crack depth (b) ≥ cladding wall thickness. Cladding fracture occurs at t_f where K ≥ K_{IC}.**

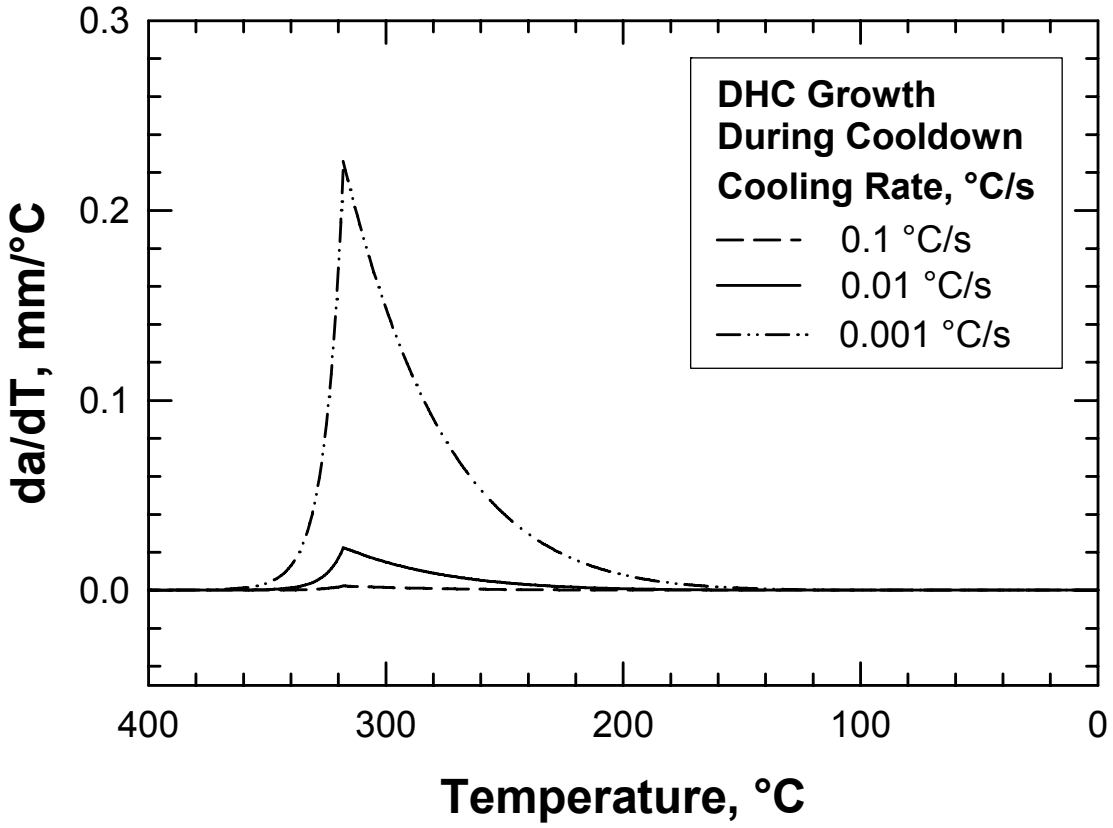

Figure 25. DHC growth rate per unit temperature change as a function of cladding temperature for three cooling rates. [1 mm/ºC = 0.022in/ºF; T(ºF) = 1.8 × T(ºC) + 32; 1 ºC/s = 1.8 ºF/s]

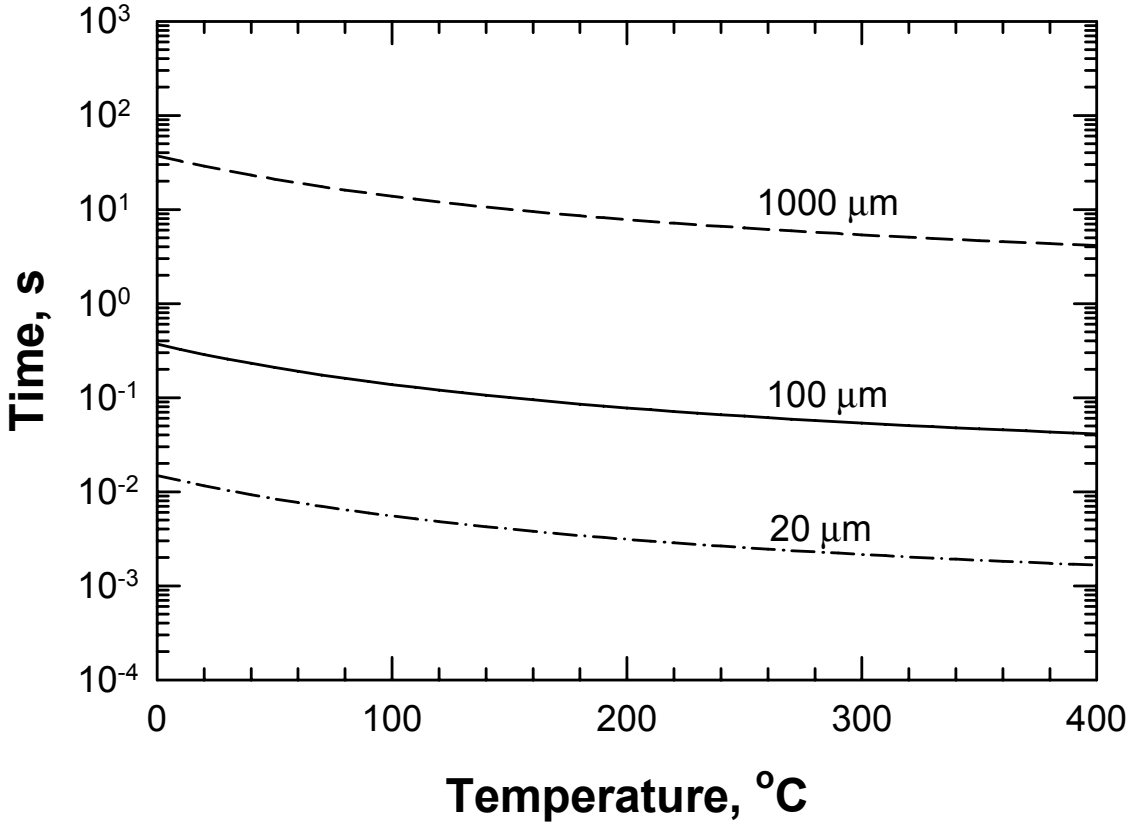

Figure 26. Times required for the diffusion of hydrogen atoms from various distances to form hydrides at the crack tip. [T(°F) = 1.8T(°C) + 32; 1 μm = 0.0394 mil]

Figure 1. DHC velocity as a function of the Mode I stress intensity factor, K, showing a growth threshold, K_{IH}, for the onset of DHC, a constant velocity region, and a fast fracture region.

Figure 2. The DHC growth threshold K_{IH} of Zr-2.5 Nb compared to the critical stress intensity factor, K_{IC}, for fracture of bulk hydrides. Experimental data are from Shi and Puls [13] and Simpson and Cann [63]. {1 MPa$(m)^{1/2}$ = 0.91 ksi$(in)^{1/2}$; T(°F) = 1.8[(K) – 273] + 32}

Figure 3(a). Schematic showing crack-tip hydride and stresses.

Figure 3(b). Profiles of $\sigma_{local} = \sigma_{eff} + \sigma_{hydride}$ at crack tip for a hydride 2μm [7.87×10^{-2} mil] thickness, 10μm [0.39 mil] long, and 10 μm [0.39 mil] wide under different K values. Results are from Shi and Puls [13]. [1 MPa = 0.145 ksi]

Figure 4. Comparison of theoretical K_{IH} with experimental data. Data are from Shi and Puls [13]. [1 MPa$(m)^{1/2}$ = 0.91 ksi$(in)^{1/2}$]

Figure 5. Crack-tip shielding of a crack in an elastic field by the compressive transformation stresses accompanied by hydride formation at a crack tip.

Figure 6. Theoretical values of K_{IH} based on the fracture toughness (K_{IC}) of hydrides {data are from Simpson and Cann [63]} and crack-tip shielding of near-tip stress intensity factor (K_S) compared against experimental data of K_{IH} from the literature {data are from Coleman [39]; Shi and Puls [13]; Huang and Mills [38]; Pettersson, et al. [44]; Kim, et al. [40]}. {1 MPa$(m)^{1/2}$ = 0.91 ksi$(in)^{1/2}$; T(°F) = 1.8[T(K) – 273] + 32}

Figure 7. Comparisons of large crack and small crack threshold stresses for delayed hydride cracking in Zr-2.5% Nb for K_{IH} values of 5.38 MPa $\sqrt{m}$ [4.9 ksi$(in)^{1/2}$] and 12 MPa $\sqrt{m}$ [10.9 ksi$(in)^{1/2}$]. The threshold stresses for DHC approach the hydride fracture stress, which is 648 MPa [94 ksi] {data are from Shi and Puls [17]}, at various crack lengths, depending on the K_{IH} value. DHC growth occurs when the cladding stress exceeds the threshold stress at a given crack length. [1 MPa = 0.145 ksi; 1 MPa$(m)^{1/2}$ = 0.91 ksi$(in)^{1/2}$; 1 μm = 0.0394 mil]

Figure 8. Dependence of K_{IH} on crack length for small cracks. For a crack depth of 10–20 μm [0.39–0.99 mil], $K_{IH} \approx$ 3.3–4 MPa$(m)^{1/2}$ [3–3.64 ksi$(in)^{1/2}$], but its value increases rapidly with the crack length to saturate at the large crack threshold. [1 MPa$(m)^{1/2}$ = 0.92 ksi$(in)^{1/2}$; 1 μm = 0.0394 mil; 300K = 80.6 °F; 600K = 620.6 °F]

Figure 9. Profiles of $\sigma_{local} = \sigma_{eff} + \sigma_{hydride}$ at crack tip for hydrides having different lengths under K = 10 MPa(m)$^{1/2}$ [9.1 ksi(in)$^{1/2}$]. Results are from Shi and Puls [13]. [1 MPa = 0.145 ksi; 1 μm = 0.0394 mil]

Figure 10. Threshold stress intensity factor, K_{IH}, of Zr-2.5 Nb tube with crack growth direction as a function of the basal pole components. Data are compiled by Kim, et al. [40]. [1 MPa(m)$^{1/2}$ = 0.91 ksi(in)$^{1/2}$]

Figure 11. The threshold stress intensity factor, K_{IH}, as a function of hydrogen concentration in solid solution. Experimental data and theoretical model are from Shi and Puls [41]. [1 MPa(m)$^{1/2}$ = 0.91 ksi(in)$^{1/2}$; 523 K = 482 ºF; 2 μm = 0.0787 mil]

Figure 12. Terminal solubility limits for zirconium: TSSD-hydride dissolution limit, TSSP-hydride precipitation limit, and crack initiation temperature. Results are from Sagat and Puls [7]. {T(ºF) = 1.8[T(K) – 273] + 32}

Figure 13. Dependence of K_{IH} on irradiation fluence. Data are from Sagat et al. [43]. [1 MPa(m)$^{1/2}$ = 0.91 ksi(in)$^{1/2}$; 1 n/m^2 = 10.8 n/ft^2]

Figure 14. High temperature crack velocity data for DHC in irradiated and unirradiated Zr-2.5% Nb material. Data are from Sagat and Puls [7] ; Huang and Mills [38]; Grigoriev and Jakobsson [46]. {T(ºF) = 1.8[T(K) – 273] + 32; 1 m/s = 3.28 ft/s}

Figure 15. Computed time to leakage based on crack depth equal cladding wall thickness compared against computed time to fracture based on the stress intensity factor exceeding a critical stress intensity factor of 70 MPa(m)$^{1/2}$ [63.7 ksi(in)$^{1/2}$]. [1 mm = 39.4 mil]

Figure 16. Computed time to leakage (crack depth = wall thickness) and time to fracture K >K_{IC}) by DHC in Zr-2.5% Nb as a function of temperature. The results show the time to failure (leakage or fracture) decreases with increasing temperature from 0 to 320 °C [32 to 608 ºF] and increases from 320 to 350 °C [608 to 662 ºF]. No DHC failure occurs at temperatures above 350 °C [662 ºF] because of the absence of hydride formation at the crack tip. {T(ºF) = 1.8T(ºC) + 32; 1 MPa(m)$^{1/2}$ = 0.91 ksi(in)$^{1/2}$}.

Figure 17. Comparison between radial and axial DHC velocity for Zr-2.5% Nb pressure tubes. Data are from Sagat, et al. [43] and Kim, et al. [40]. RD: radial direction; AD: axial direction; CL: confidence limits. {1 m/s = 3.28 ft/s; T(ºF) = 1.8[T(K) – 273] + 32}

Figure 18. Axial position versus length of inner wall cracks observed in REP-Nal. Data are from Chung [25]. [1 mm = 39.4 mil; 1 μm = 0.0394 mil]

Figure 19. **Summary of possible failure mechanisms in high burnup Zr-based fuel cladding tubes, showing (i) oxide formation and cracking on outer wall, (ii) hydride blister formation and cracking, (iii) hydride reorientation, and (iv) uniform corrosion on the inner wall. Once initiated, the outer wall and inner wall cracks can propagate by DHC if $K > K_{IH}$. Schematic corresponds to a cross section of the cladding perpendicular to the axial direction where σ_h denotes hoop stress.**

Figure 20. **Pellet-cladding mechanical interaction results from the thermal expansion and cracking of the UO_2 fuel pellets during power ramp and induces local tensile hoop stresses in the cladding that can potentially propagate an existing crack or defect by DHC.**

Figure 21. **Stress transients associated with pellet-cladding mechanical interactions: (a) Type I stress transient with a stabilized stress that leads to $K > K_{IH}$ and DHC, (b) Type II stress transient with a peak stress that leads to $K > K_{IH}$ and DHC over a short duration (130 minutes) and stabilized stress that results in $K < K_{IH}$ and crack arrest, and (c) Type II stress transient with a 7-minute duration where $K > K_{IH}$ and DHC growth can occur. [1MPa = 0.145 ksi]**

Figure 22. **Critical tensile stresses for hydride reorientation as a function of temperature compared against experimental data compiled by Chung [25], cold-worked and stress-relieved (CWSR) Zircaloy-4 data compiled by Ferry and Poinssot [95], and stress-relief annealed (SRA) Zircaloy-4 by Chu, et al. [96] and Daum, et al. [97]. The stress limit defined in the NRC Interim Staff Guidance-II Revision 3 (ISG-II Rev. 3) [94] is shown as the dotted line.**

Figure 23. **A comparison of cladding stresses under various loading conditions and crack lengths against the large crack and small crack threshold stresses for the onset of DHC in Zr-alloy cladding tubes made of Zircaloy-2 or pressure tubes made of Zr-2.5% Nb. [1 MPa = 0.145 ksi; 1 $MPa(m)^{1/2}$ = 0.91 $ksi(in)^{1/2}$; 1 µm = 0.0394 mil]**

Figure 24. **DHC growth resulting from PCMI stress transients during power ramps. Crack extension was computed for Zr-2.5% Nb cladding on the basis of PCMI stress transients reported by Schäffler, et al. [7] and Brochard, et al. [53,54]. [1 mm = 39.4 mil; 318 ºC = 604.4 ºF]. Leakage occurs at t_l where the crack depth (b) ≥ cladding wall thickness. Cladding fracture occurs at t_f where $K \geq K_{IC}$.**

Figure 25. **DHC growth rate per unit temperature change as a function of cladding temperature for three cooling rates. [1 mm/ºC = 0.022in/ºF; T(ºF) = 1.8 × T(ºC) + 32; 1 ºC/s = 1.8 ºF/s]**

Figure 26. Times required for the diffusion of hydrogen atoms from various distances to form hydrides at the crack tip. [T(°F) = 1.8T(°C) + 32; 1 μm = 0.0394 mil]